PhD Dissertation

Field Weakening and Sensorless Control Solutions for Synchronous Machines Applied to Electric Vehicles

Author:
Elena Trancho Olabarri

February 26, 2018

eman ta zabal zazu

Universidad del País Vasco
Euskal Herriko Unibertsitatea

Thesis directors:
Edorta Ibarra Basabe
Antoni Arias Pujol

(c)2018 ELENA TRANCHO OLABARRI

tecnalia Inspiring Business

UNIVERSITAT POLITÈCNICA DE CATALUNYA
BARCELONATECH

Agradecimientos

Durante este tiempo sois muchas las personas que habéis participado en este trabajo y os quiero expresar mi gratitud por el apoyo y la confianza que me habéis prestado.

En primer lugar me gustaría dar las gracias a mis directores de tesis Edorta Ibarra Basabe y Antoni Arias Pujol. Edorta, gracias por haberme animado desde el minuto cero a embarcarme en esta aventura. Gracias por enseñarme a investigar de verdad, por protegerme y por dejarme compartir contigo mis altibajos emocionales. Gracias, Toni, por tus consejos, tu disponibilidad, tu paciencia y tus *master classes* virtuales a través de Skype. Pocas veces se crean buenos grupos de trabajo, y el formado por Los Tres Tenores es un buen ejemplo. Me gustaría dar las gracias también a Iñigo Kortabarria, por toda su ayuda desde el comienzo hasta hoy.

Todo esto nunca hubiera sido posible sin el respaldo de mis compañeros de Tecnalia. Gracias a todos, a los que seguís y a los que ya no estáis. Gracias por vuestra disponibilidad, vuestra ayuda incondicional y gracias por todas las horas de más dedicadas a la puesta a punto del banco de pruebas.

Quisiera agradecer la cálida acogida por parte de mis compañeros del grupo de investigación en electrónica aplicada APERT. Muchas gracias por contar conmigo y por hacerme sentir una más.

Finalmente, quiero dar las gracias a mi familia. A Pablo, por sacrificar muchas tardes y sábados de verano acompañándome a Tecnalia para rehacer pruebas, y por aguantar con una sonrisa mis días malos. Y a ama, aita y Eduardo por animarme, entenderme y por hacer más fáciles los días difíciles.

A todos, muchísimas gracias de todo corazón.

En Bilbao, Febrero de 2018.

Contents

List of Figures

List of Tables

Abstract

Nowadays and due to environmental concerns, the automotive industry is greatly involved with the reduction of on road vehicle pollutant emissions. Transport electrification is considered as a key technology to achieve this goal. However, an extensive research and development of high efficient, low cost, optimized and reliable electric propulsion systems is required in order to achieve these objectives.

Electric machines can be considered as the main elements of Electric Vehicle (EV) propulsion systems. These machines must fulfil a number of particular characteristics, such as high power and torque densities, high efficiency and fault tolerance capability. Due to these requirements, Permanent Magnets Synchronous Machines (PMSM) are the most established technologies in current hybrid and electric vehicles. However, their high power density is achieved thanks to rare-earth magnetic materials, whose use involves economic, environmental and politic issues. Therefore, alternative rare-earth free machines are being investigated, such as Permanent Magnet assisted Synchronous Reluctance Machines (PM-assisted SynRMs).

Regarding the aforementioned automotive synchronous machines, the development of efficient and reliable torque control strategies is of great importance. Due to volume optimization requirements, electric machines suffer from high non-linearities as a consequence of magnetic saturation. Therefore, an accurate machine electromagnetic model is required by the controller, where magnetic saturation phenomena cannot be neglected. Besides, mismatches between Finite Element Models (FEM) and real prototypes are usual due to manufacture tolerances, operation temperature and ageing, leading to electric parameter deviations. Conventional control approaches highly depend on machine electrical parameters, and they can eventually loss controllability when the stator voltage limit is reached, i.e., in field weakening or deep field weakening operation. Additionally, fault tolerance is considered as crucial by the EV industry, being limp-home capability a desirable feature for future electrified vehicles. In this sense, a great amount of literature focused on both topics can be found in the scientific literature.

In this thesis, a general overview of an EV powertrain system is provided. The existing electric machine technologies for EV applications and the most common torque control approaches for synchronous machines are then reviewed. Once an accurate electromagnetic model for three-phase synchronous machines including magnetic saturation is provided, Proportional Integral (PI) based Field Oriented Control (FOC) and second order Sliding Mode Control (SMC) approaches are thoroughly detailed.

Once the state of the art has been reviewed, this thesis proposes two novel control solutions which improve the robustness of current automotive synchronous machine torque control strategies in field weakening and deep field weakening operation regions, ensuring a reliable and efficient system performance under parameter uncertainties. These strategies combine a Voltage Constraint Tracking (VCT) feedback algorithm with the well established Look-up Table (LUT) set-point generation approach. The proposed strategies are conceived to drive the system into a pseudo-optimal operation point when the controllability is not guaranteed, ensuring proper field weakening operation and maintaining the optimal current set points when deviations are small and system controllability is ensured by LUT data.

On the other hand and considering the importance of fault tolerance in the automotive industry, this work also proposes a novel sensorless control algorithm to provide limp-home capability under machine encoder or resolver failures. This strategy combines a Phase Locked Loop (PLL) based position estimator for medium to high speed ranges, and a High Frequency Injection (HFI) technique for low speeds and standstill. The work also focuses on the development of a robust strategy to ensure smooth transitions between both PLL and HFI techniques. The proposed sensorless algorithm is successfully combined with the novel VCT/LUT approach, providing the required limp-home operation.

Simulation and experimental results obtained in an automotive grade 51 kW PM-assisted SynRM are provided, demonstrating the validity of the proposed strategies.

Resumen

Hoy en día, la polución es uno de los mayores problemas de los países industrializados. El sector de la automoción es uno de los que más contribuye en la emisión de gases de efecto invernadero (GHG, *Greenhouse Gas*), llegando a ser responsable de hasta el 15 % del total de emisiones de CO_2 de la Unión Europea. Por ello, la industria de la automoción es uno de los sectores más implicados en la reducción de emisiones de CO_2. Por las razones anteriormente expuestas, la electrificación del transporte por carretera está en pleno auge, favoreciendo nuevas oportunidades para la investigación y el desarrollo industrial. Aunque a día de hoy uno de los mayores retos tecnológicos radica en el desarrollo de baterías que incrementen la autonomía de los vehículos eléctricos e híbridos, el desarrollo de sistemas de propulsión eficientes, fiables, compactos y económicos juega también un papel relevante para la introducción del vehículo eléctrico en el mercado.

Para el diseño del sistema de propulsión de un vehículo eléctrico, la elección de la máquina eléctrica es un aspecto importante, ya que deben ser capaces de operar en una serie de condiciones particulares, incluyendo el funcionamiento a altas velocidades, junto con aceleraciones bruscas y temperaturas extremas. Además, dichas máquinas deben ofrecer una serie de características deseables, tales como altas densidades de potencia y par. Por otro lado, deben ser eficientes y, en la medida de lo posible, tolerantes a fallos. Teniendo en cuenta estas características, las Máquinas Síncronas de Imanes Permanentes (PMSMs, *Permanent Magnet Synchronus Machines*) son, a día de hoy, la tecnología más utilizada en vehículos eléctricos e híbridos. Sin embargo, estas máquinas cuentan con una alta densidad de potencia gracias al uso de materiales magnéticos de alta densidad, entre los cuales destacan las aleaciones neodimio-hierro-boro (NdFeB) y, en menor medida, materiales como el disprosio (Dy) y el Terbio (Tb). El uso de estos materiales, también conocidos como tierras raras (REE, *Rare-Earth Elements*), conlleva asociados una serie de problemas económicos,

medioambientales y políticos. Por ello, existe un creciente interés por desarrollar y producir sistemas de propulsión sin tierras raras, donde destacan las máquinas de reluctancia síncrona asistidas por imanes de ferrita (PM-assisted SynRM, *Permanent Magnet Assisted Synchronous Reluctance Machines*).

En lo que a las técnicas de control de este tipo de máquinas síncronas se refiere, es fundamental el desarrollo de estrategias de control eficientes y robustas. En este sentido, las particularidades de las máquinas électricas y los escenarios de operación del vehículo eléctrico hacen que estos requisitos produzcan nuevos retos tecnológicos, tanto para el mundo académico como para la industria. Por un lado, los diseños de las máquinas tienden a ser cada vez más compactos para, de este modo, aprovechar mejor el espacio disponible en el vehículo. Estas optimizaciones dan lugar a máquinas con parámetros eléctricos altamente no lineales, causados por el efecto de la saturación magnética. En este contexto, es muy importante disponer de una caracterización electromagnética fiable de la máquina. Sin embargo, las diferencias existentes entre las predicciones de los parámetros eléctricos obtenidos a partir de simulaciones basadas en elementos finitos (FEM, *Finite Element Model*) y la máquina prototipo real (generalmente debidas a la dependencia de dichos parámetros con la temperatura, el envejecimiento de la máquina y tolerancias de fabricación, entre otros) favorecen la aparición de desviaciones entre los parámetros eléctricos teóricos y reales. Estos factores hacen que el uso de técnicas de control convencionales, altamente dependientes del conocimiento previo de los parámetros eléctricos de la máquina, no sean lo suficientemente robustas y puedan producir problemas de controlabilidad en las zona de debilitamiento de campo (FW, *Field Weakening*) y debilitamiento profundo de campo (*deep Field Weakening*).

Por otro lado, las tendencias futuras en aplicaciones de propulsión eléctrica incluyen el desarrollo de máquinas síncronas de alta velocidad (HSEM, *High Speed Electric Machine*)[1] con el fin de reducir, más aun, el volumen de la máquina eléctrica. En este tipo de máquinas, los niveles de potencia nominal y máxima requeridas para el vehículo se mantienen, ya que se aumenta la velocidad mecánica del motor y se reduce el par requerido. En general, la región de debilitamiento de campo se extiende en este tipo de máquinas. El desarrollo de HSEMs conlleva una serie de nuevos retos tecnológicos necesarios para garantizar un correcto funcionamiento del sistema. En lo que a las estrategias de control se refiere, es necesario desarrollar estrategias de control avanzadas que aseguren un correcto control a altas velocidades, o considerar técnicas que contemplen el

---

[1] Hoy en día se consideran máquinas HSEM aquellas que operan por encima de 10000 rpm. Sin embargo, en un futuro próximo se espera desarrollar gran número de máquinas para vehículo eléctrico e híbrido cuyo rango de operación supere los 15000 rpm.

efecto de los retrasos de las señales en el control. Otra posibilidad radica en el aumento de las frecuencias de muestreo de los algoritmos de control, lo que deriva en un aumento de la frecuencia de conmutación de los convertidores de potencia. Por ello, cabe destacar la nueva generación de dispositivos de potencia basados en semiconductores de banda ancha (WBG, *Wide Band Gap*) como los dispositivos de Carburo de Silicio (SiC) o Nitruro de Galio (GaN).

Ante estos dos escenarios futuros (dependencia de parámetros eléctricos y operación a altas velocidades), resulta de especial interés para la industria del vehículo eléctrico e híbrido el desarrollo de estrategias de debilitamiento de campo robustas.

Otro requisito indispensable para los sistemas de propulsión aplicados a los futuros vehículos eléctricos es la fiabilidad de los mismos. La detección de faltas y la tolerancia a fallos son necesarias no sólo para garantizar la seguridad del vehículo, sino que también lo son para garantizar el funcionamiento ininterrumpido del sistema bajo condiciones de falta. Llevando a cabo un modelo de modos de fallos y análisis de sus efectos (FMEA, *Failure Mode and Effect Analysis*), se deduce que un fallo de resolver (o de encoder), encargado de proporcionar la posición del rotor de la máquina e indispensable para la orientación de campo y para el algoritmo de control, tendría consecuencias catastróficas para el sistema. En este sentido, numerosos estudios se centran en el desarrollo de técnicas para la estimación de la posición y la velocidad del rotor, también llamadas técnicas *sensorless*. El objetivo de estos estudios es, en su mayoría, proporcionar estrategias capaces de garantizar que el vehículo llegue a su destino bajo condiciones de seguridad y en funcionamiento pseudo-óptimo, a pesar de que haya ocurrido un fallo. Este concepto es también conocido como operación *limp-home*.

Considerando todo lo anterior, en esta tesis se presenta, en primer lugar, la arquitectura general del sistema de propulsión de un vehículo eléctrico. En este sentido, se incluye un estado del arte de las tecnologías de máquinas de automoción actuales y sus características principales. A continuación, se muestra un modelo electromagnético detallado de una máquina síncrona trifásica teniendo en cuenta el efecto de la saturación magnética. Finalmente, se explican las técnicas de control de par comúnmente utilizadas para este tipo de aplicaciones, donde cabe destacar el control orientado a campo (FOC, *Field Oriented Control*) basado en PIs y el control por modo deslizante de segundo orden (second order SMC, *Sliding Mode Control*). Aunque la técnica de control FOC basada en PIs es la estrategia más utilizada en la industria, las altas no-linealidades de este tipo de máquinas hacen que sea interesante utilizar estrategias de control no lineales, tales como la técnica SMC de segundo orden.

Una vez presentado el estado del arte relacionado con la temática de la tesis, se proponen dos nuevas soluciones de control para mejorar la robustez de las estrategias de debilitamiento de campo actuales, asegurando un comportamiento fiable del sistema. En primer lugar, se realiza una formulación detallada de las cuatro regiones de operación de las máquinas síncronas de automoción (MTPA, *Maximum Torque per Ampere*, FW y MTPV, *Maximum Torque Per Voltage*), y se presenta el análisis matemático necesario para la obtención de las corrientes óptimas en cada región de operación. En concreto, esta tesis se centra en la técnica de control indirecto FOC, donde las corrientes óptimas de referencia son previamente calculadas analíticamente y almacenadas en tablas interpoladas (LUT, *Look-up table*). Esta estrategia es comúnmente utilizada en la industria en general, y en el sector de la automoción en particular, ya que su coste computacional es bajo comparado con otras alternativas y, además, es relativamente simple de implementar. Sin embargo, esta estrategia en particular ajusta las LUTs para un determinado conjunto de parámetros eléctricos de la máquina, pudiendo llegar a producir inestabilidades cuando existen desviaciones de parámetros, dando como resultado un incorrecto control en debilitamiento de campo. En este sentido, se presentan dos algoritmos de control FW robustos ante variaciones de parámetros: (a) *flowchart based* y (b) *integration based VCT (Voltage Constraint Tracking).*

Las estrategias de debilitamiento de campo propuestas se basan en la regulación de la tensión de estator cuando el sistema entra en las regiones FW y MTPV, asegurando que el sistema permanece siempre por debajo del límite de tensión máximo de estator establecido. De esta manera, garantizan la controlabilidad del sistema en todo su rango de operación. Para ello, dirigen el sistema hacia un punto de operación pseudo-óptimo cuando las desviaciones de parámetros son lo suficientemente grandes como para descontrolar el sistema. Las dos técnicas propuestas son analizadas y comparadas en simulación. La validación experimental se realiza en una PM-assisted SynRM de 51 kW, utilizando la estrategia *integration based VCT*, dado su bajo coste computacional y su ajuste simple. Por otro lado, el control convencional FOC basado en PI es sustituido por el control FOC basado en SMC, dada su idoneidad para sistemas altamente no-lineales. La validación experimental se lleva a cabo empleando los datos del análisis FEM proporcionado por el fabricante para el ajuste de las LUTs, detectándose desviaciones debidas a la temperatura del rotor, la fabricación (tolerancias en el *airgap*) y al modelo FEM utilizado (modelo 2.5D). Se confirma experimentalmente que, sin una estrategia de control robusta como la propuesta, el sistema de propulsión pierde ampliamente su capacidad de operación. En esta aplicación en particular, esto equivaldría a limitar a 40 km/h la velocidad máxima del vehículo. Se demuestra finalmente que el uso de la estrategia propuesta asegura un correcto funcionamiento del sistema en todo el rango de operación. El control FW propuesto ha sido validado en condiciones de condución mediante la aplicación del ciclo de homologación de consumos europeo WLTP (*Worldwide harmonized Light vehicles Test Procedure*).

Finalmente, en esta tesis se propone una estrategia de control de par tolerante a fallos de resolver. Se presenta una técnica *sensorless* híbrida compuesta por un estimador basado en una PLL (*Phase Locked Loop*) y la técnica por injección de componente de alta frecuencia (HFI, *High Frequency Injection*). El estimador basado en PLL se utiliza para estimar la posición del rotor en rangos de velocidad medios/altos, mientras que el uso de la técnica HFI se limita a la determinación de la posición a bajas velocidades y en parado. El trabajo desarrollado en esta tesis se centra en el desarrollo de una estrategia de transición entre ambas técnicas, basada en bandas de histéresis y dependiente de la velocidad. Esta estrategia tiene como objetivo el aportar robustez y seguridad durante el periodo de transición entre PLL y HFI. La contribución desarrollada tiene en cuenta el particular escenario del EV, incluyendo funcionamiento en cuatro cuadrantes (motor y generador) y pasos por cero. Esta estrategia se valida en una PM-assisted SynRM de 51 kW, ejecutándose junto con la estrategia de debilitamiento de campo anteriormente propuesta, de forma que se obtienen resultados satisfactorios, ya que se logra un rango de operación suficiente como para garantizar el funcionamiento *limp-home* del sistema.

Laburpena

Gaur egun, automobilaren industria buru-belarri ari da lanean ibilgailuek sortzen dituzten gas kutxakorren emisioak murrizteko. Testuinguru horretan, ibilgailuen elektrifikazioa aukera egokia da helburu hori lortzeko. Horretarako, beharrezkoa da eraginkorrak, merkeak, optimizatuak eta fidagarriak diren propultsio-sistema elektrikoak garatzea.

Motor elektrikoak dira ibilgailu elektrikoen propultsio-sistemen osagarri nagusiak. Ezaugarri partikular batzuk bete behar izaten dituzte motor horiek, hala nola potentzia-dentsitate eta eraginkortasun altua izatea, eta baita ere hutsegite-tolerantzia gaitasuna izatea, besteak beste. Beharrizan horiek direla eta, iman iranunkorreko makina sinkronoa (PMSM, *Permanent Magnet Synchronous Machine*) da, gaur egun, teknologia erabiliena ibilgailu hibrido eta elektrikoetan. Hala ere, PMSMen potentzia-dentsitate altua lur arraroetan oinarritutako material magnetikoei esker lortzen da. Material horien erabilerak ekonomian, ingurumenean eta geopolitikan izan dezakeen eragina kontua hartuta, lur arraroetan oinarritzen ez diren aukerak ikertzen ari da komunitate zientifikoa; hala nola imanez lagundutako erreluktantzia sinkronoko makinak (*PM-assisted Synchronous Reluctance Machines*, PM-assisted SynRM) kontsideratzen dira ordezko bideragarri bezala.

Automobilerako motor elektriko sinkrono horiei dagokienez, oso garrantzitsua da eraginkorrak eta fidagarriak diren momentu elektromagnetikoaren kontrolerako algoritmoak garatzea. Motor horien bolumena optimizatu behar denez, parametro elektrikoetan ez-linealtasun handiak agertzen dira saturazio magnetikoaren ondorioz. Beraz, makinen modelo elektromagnetiko zehatzak behar dira kontrolagailuak doitzeko. Alde horretatik, elementu finitu (FEM) bidez aurreikusitako parametroen eta prototipo errealen parametroen arteko ezberdintasunak nahikoa ohikoak dira, fabrikazio-tolerantzien, operazio-tenperaturaren eta makinaren zahartzearen eraginez. Kontrol-algoritmo konbentzionalek motorren parametroekiko oso sentikorrak dira, eta kontrolagarritasuna gal daiteke esta-

toreko tentsio maximora iristean, hori da, eremu-murrizketa (*field weakening*) eta eremu-murrizketa sakoneko (*deep field weakening*) operazio-eremuetan. Horrez gain, hutsegite-tolerantzia ere kontsideratzen da ibilgailu elektrikoaren industrian, ibilgailua modu degradatuan tailerrera iritsi ahal izateko matxurak gertatzerakoan. Bi esparru horien inguruko hainbat lan aurki daitezke literatura zientifikoan.

Tesi honetan, ibilgailu elektriko baten propultsio-sistema gainbegiratzen da, eta aplikazio horietan erabiltzen diren motor elektrikoen teknologiak eta momentu elektromagnetikoaren kontrolerako algoritmoak berrikusten dira. Saturazio magnetikoa kontuan hartzen duen hiru fasedun makina sinkronoaren modelo elektromagnetiko zehatza azaldu ondoren, erregulatzaile proportzional integraletan eta bigarren ordenako lerradurazko kontrolean (*Sliding Mode Control*, SMC) oinarritutako FOC (*Field Oriented Control*) kontrol-teknikak azaltzen dira sakon.

Ondoren, ibilgailu elektrikoetako motor sinkronoak eremu-murrizketa eta eremu-murrizketa sakonean kontrolatzeko erabiltzen diren kontrol-algoritmoen mardultasuna hobetzen duten bi algoritmo berri proposatzen ditu tesi honek. Era horretara, sistemaren fidagarritasuna bermatzen da parametro elektrikoen ziurgabetasunen aurrean. Estatoreko erreferentziazko korronteak sortzeko oso ezaguna den tauletan oinarritutako teknika (*Look-up Table*, LUT) eta *Voltage Constraint Tracking (VCT)* motako berrelikadura konbinatzen dute proposatutako teknikek. Horrela, operazio-puntu pseudo-optimo batetara eramaten da sistema, kontrolagarritasuna bermatuta ez dagoenean. Aldiz, erreferentzia optimoak mantentzen ditu algoritmoak, makinaren kontrolagarritasuna bermatuta badago.

Automobilaren industrian hutsegite-tolerantziari ematen zaion garrantzia kontuan hartuta, posizio-sentsoreen hutsegiteen aurrean etxera itzultzeko gaitasuna (*limp-home capability*) eskaintzen duen *sensorless* motako kontrol-algoritmo berri bat proposatzen du ere lan honek. PLL (*Phase Locked Loop*) eta maiztasun altuko injekziozko (*High Frequency Injection*, HFI) teknikak konbinatzen ditu proposatutako algoritmoak. Tesi honetan, teknika horien arteko trantsizio leunak eta mardulak gauzatzen dituen algoritmo berria proposatu da ere. Azkenik, proposatutako *sensorless* eta VCT/LUT estrategiak konbinatuz lortu da makina sinkronoak beharrezkoa duen etxera itzultzeko gaitasuna.

51 kW dituen automobilerako PM-assited SynRM motako motor sinkrono batetarako lortutako simulazio-emaitzek eta emaitza esperimentalek erakusten dute proposatutako kontrol-estrategien baliagarritasuna.

Chapter 1

Introduction

1.1 Context

The research work resulting in this thesis has been carried out in the transport business area of Tecnalia Research & Innovation (Industry and transport Unit), in collaboration with the *Applied Electronics Research Team* (APERT) of the Electronics Technology department, University of the Basque Country (UPV/EHU) and with the *Institut d'Organitzacio i Control de Sistemes Industrials* of the*Universitat Politècnica de Catalunya* (UPC).

Tecnalia's transport area focuses its activity in the research and development of hybrid and electric propulsion systems, including the following topics:

- Research, design and development of advanced control strategies for automotive electric machines applied to electric and hybrid propulsion systems. Current research interests include the study of control strategies for high speed operation, sensorless control, fault tolerant operation and multiphase machine control.

- Research and development of optimal energy management strategies, including energy recovery during regenerative braking, damage reduction on mechanical components and vehicle life-cycle and autonomy range extension.

- Research in automated driving, including Advanced Driver Assistance Systems (ADAS). Research interests in this specific field include decision-making systems, which enable the design of new ADAS for control sharing between the vehicle and the driver.

- Research in new multi-material structures for weight reduction purposes.

On the other hand, the APERT research activities include the following topics:

- Reconfigurable systems and System on Chip (SoC): Development of optimized digital systems for reconfigurable logic including the research, design and development of partial reconfiguration techniques and fault tolerant strategies for safer and more reliable systems.
- Power and control circuitry for energy converters. Research and design of power electronics systems used for electric energy generation, transformation and storage, being of special interest automotive and aerospace applications.

Finally, the Division of Automatic Control at the *Institut d'Organitzacio i Control de Sistemes Industrials*, which belongs to the UPC, focuses its research interests (among others) in:

- Modelling and control of electronic power systems (generation and conversion).
- Sensorless control of Electric Drives.

Regarding public research projects, this thesis has been partially supported by the FP7 framework/European Commission under grant number 605075, "*Synchronous Reluctance Next Generation Efficient Motors for Electric Vehicles*" (SYRNEMO) project (October 2013-November 2016). The purpose of this project was to design and validate, in an automotive test bench, a drive including a high speed synchronous reluctance machine assisted by ferrite magnets, studying its suitability for automotive applications. The consortium involved in the project consisted of eight partners: Austrian Institute of Technology (project coordinator), AVL, Centro Ricerche Fiat SpcA, Leibniz University of Hannover, Tecnalia Research & Innovation, THIEN eDrives, University of Bologna and Vrije Universiteit Brussel. The project delivered a fully electric powertrain technology at TRL 5-6, to be integrated in large-scale production of future electric vehicles. In this project, driving efficiency and environmental compatibility where enhanced, in line with the EU policies in the field of low-carbon transport and Green House Gas (GHG) emissions reduction for road transport[1]. In this context, Tecnalia's activities included the design of a robust torque control strategy ensuring controllability of the drive in the whole vehicle operation range. In order to cope with resolver failures, a sensorless control technique was implemented to guarantee the limp-home operation of the vehicle. Tecnalia was also responsible for the powertrain testing and validation in an automotive grade test bench, available at Tecnalia's premises.

Additionally, this work has been partially supported by the Basque Government within the regional projects KT4eTRANS (KK-2015/00047 and KK-2016/00061) of the ELKARTEK programme, and FPGAmc (EMAITEK programme).

1.2 Introduction to the thesis

Pollution is considered as one of the greatest problems in the industrialized countries. Attending to several studies, transport is one of the major contributors of pollutants in urban areas. Taking into account the increasing ecological awareness and the shortage of fossil-fuel resources, one of the most involved sectors in the reduction of pollution is the automotive industry. The transport electrification is opening new technological challenges and opportunities [2], such as the development of high density batteries to increase the vehicle's autonomy and the design and research on efficient, low cost, optimized and reliable electric propulsion systems [2–4].

The selection of the electric machine is one of the key aspects in the design of an Electric Vehicle (EV) propulsion system. In general, the electric machine must be as efficient as possible at several operation points, allowing energy recovery during braking. Additionally, it must offer high acceleration rates for fast starting, and it must operate at extreme ambient temperatures. Taking into account the automotive industry context, a) high power and torque densities, b) high efficiency, c) fault tolerance capability and d) low cost and simplicity are desirable characteristics for electric machines [5]. In this sense, Permanent Magnets Synchronous Machines (PMSMs) are the most established technologies [6] due to their high power density and reduced weight [4, 7].

The high power density requirements are met thanks to magnetic materials, usually sintered neodymium-iron-boron (NdFeB) alloys, and other Rare-Earth Elements (REE), such as dysprosium (Dy), whose use involve some disadvantages [8, 9] such as the high cost of magnetic materials, risk of depletion and resource monopoly issues. Due to the above economic, environmental

---

[1] http://www.syrnemo.eu/

and politic reasons, there is a growing need to produce efficient rare-earth free propulsion systems, motivating the automotive sector to investigate different alternatives. Rare-Earth free machine technologies such as Induction Machines (IM), Switched Reluctance machines (SRM) or Synchronous Reluctance machines (SynRM) are being considered for EV and HEV applications [9]. However, a comparison of the different machine technologies regarding relevant aspects such as efficiency, robustness, power density, control simplicity and costs, among others, show that the suitability of each technology depends on the specific application, not being straightforward to determine the superiority of one machine over the others. In this context, the contributions of this thesis will focus on both REE based Interior PMSMs and rare-earth free PM-assisted SynRM technologies.

The development of reliable control algorithms that take into account the particular requirements of automotive IPMSMs and PM-assisted SynRMs is of great importance for the automotive industry. Due to machine design and optimization aspects, in automotive applications it is of common practice to reduce the volume of the machine as much as possible. These optimization requirements produce non-linearities in the electric parameters caused by magnetic saturation, which can not be neglected in the machine electromagnetic model, as they influence the control algorithm design. However, conventional control approaches strongly depend on machine electrical parameters. Among the variety of control strategies available in the scientific literature, look-up-table (LUT) based Field Oriented Control (FOC) strategies are one of the most commonly used torque control techniques for automotive synchronous machines with high saliency (IPMSMs and PM-assisted SynRMs) [10,11]. These techniques are relatively simple to implement and require low computational burden. However, deviations of the electric parameters due to machine ageing, manufacture tolerances, temperature dependency and the existing differences between the Finite Element Model (FEM) data and the real machine, together with the high non-linearities caused by the magnetic saturation phenomena can lead to control loss and uncontrollable regeneration in the field weakening region. Thus, the current tendency of extending the constant power region confirms the importance of relying on a robust control strategy to overcome the aforementioned issues and ensure a correct operation of an EV drive during its whole life-cycle.

Additionally, design trends for the next generation of EV and HEV propulsion systems include the increase of the machine operation speed for an even more compact drive. Nowadays, a great amount of medium speed electric drives (5000 rpm to 8000 rpm) can be found in the market. However, drive volume optimization requirements leads to the design of high speed electric drives exceeding 15000 rpm [5]. This trend includes additional technological challenges to be overcome. The required high switching frequencies forces traditional power electronics Silicon (Si) based devices to reach their physical limits [12,13]. New semiconductor materials such as Silicon Carbide (SiC) and Gallium Nitride (GaN) seem to be the most appropriate candidates and are currently being investigated [14, 15]. However, when conventional Si devices must be used, the switching frequency limitation leads to a number of control challenges. Advanced strategies, which cope with these relatively low sampling rates and which take into account the delays introduced by the controller, must be developed. Additionally, an increase of the drive speed range leads to the extension of the constant power region, making field weakening control even more relevant [16].

Taking the latter into account, a novel robust torque control strategy for IPMSMs and PM-assisted SynRMs applied to EVs is presented in this thesis. In order to guarantee the EV drive controllability in the whole speed/torque operation range and during the entire propulsion system lifetime, a combination of a robust second order SMC and a LUT/Voltage Constraint Tracking (VCT) based hybrid field weakening control is proposed. Simulation and experimental evidences demonstrate that the inclusion of this technique improves the overall control algorithm robustness under parameter deviations.

Other crucial requirement for future EV drives is fault tolerance [9,17]. In this context, it is relevant for the automotive industry to develop highly reliable systems that enable to complete vehicle service in derated operation mode (limp-home operation) when significant faults occur. On the one hand, research studies focused on multiphase topologies have been carried out in the last years. Multiphase machine technologies are considered as an interesting alternative for their application in EV propulsion systems due to their intrinsic fault tolerance [18]. The development of Prognostic and Health Management Systems (PHMS) is also an attractive option to increase the safety of EV end-users [19,20]. These techniques aim to predict degradation mechanisms before a fault occurs. Finally, the replacement of sensors by estimation techniques is another relevant research topic regarding fault tolerance [21]. In an EV drive, one of the most critical sensors is the resolver[2], which provides the rotor position for field orientation and control. Although a great amount of research works provide position and speed estimation techniques to eliminate the resolver, the automotive industry suggests to maintain such sensor for normal operation and considers estimation techniques for sensor degradation detection and sensorless

---

[2] Although encoders can also be used for the determination of the angular position and the speed, resolvers are preferred in the automotive industry due to their robustness.

limp-home operation [22, 23]. The particular scenario of an automotive application requires an appropriate sensorless performance for a wide speed range. This thesis proposes a novel hybrid sensorless control strategy based on the combination of two established approaches. A solution to achieve a smooth transition between both control approaches is also proposed. Simulation and experimental results validate the proposed strategy to be further implemented in electric vehicles.

1.3 Objectives

The main objective of this thesis is to improve the robustness of current torque control algorithms for automotive synchronous machines, proposing novel solutions that ensure a reliable and efficient regulation performance. In this context, the following specific objectives have been defined in order to achieve the main goal of this thesis:

(a) To gain an in deep understanding of the most common EV machine technologies and their corresponding torque control techniques, identifying the actual controller limitations and technological challenges.

(b) The proposal, development and validation of a robust torque control algorithm under machine electrical parameter deviations and uncertainties. This strategy will ensure system controllability in the whole operation range, including field weakening and deep field weakening regions.

(c) The proposal, development and validation of a fault tolerant torque control strategy against resolver failures. This contribution will be adapted to the particular electric vehicle scenario. Complex algorithms should be reduced as much as possible and computational burden should be optimized in order to guarantee a proper implementation in an automotive certified microprocessors with limited calculation capabilities.

1.4 Structure of the document

This thesis consists of five chapters and two appendixes. Apart from this introduction to the thesis, the document is organized as follows:

2. **Electric vehicle drive systems: Electric machines and control**. In this chapter, an overview of an electric vehicle powertrain architecture is

provided, including a review of the most common electric machine technologies and their features. After this introduction, the chapter focuses on synchronous machines, providing the required mathematical fundamentals[3], summarizing the torque control strategies available in the scientific literature. A comprehensive explanation of PI and SMC based Field Oriented Control (FOC) is introduced, considering their suitability for automotive synchronous machine control. Finally, this chapter discusses the challenges derived from future trends in the electric automotive sector, such as high speed machine operation and fault tolerance requirements.

3. **Look-up Table based flux weakening strategy including novel Voltage Constraint Tracking feedback**. In this chapter, a reliable field weakening control algorithm is proposed in order to guarantee an electric vehicle drive controllability in the whole torque/speed operation range, during the whole propulsion system lifetime and under parameter uncertainties. First of all, a summary of the field weakening strategies available in the scientific literature is provided, giving special interest to the mathematics involved in the calculations of the optimum current trajectories. After that, the thesis focuses on the LUT based field weakening control approach, providing guidelines for LUT dimension optimization and precalculation procedures. A combination of a robust second-order SMC and a LUT/VCT based hybrid field weakening control is finally proposed. Two VCT strategies are proposed and compared throughout simulation: a flowchart based algorithm and an integration based algorithm. Finally, the integration based strategy is considered due to its lower computational burden and easier adjustment, and is experimentally validated demonstrating the effectiveness of the proposal.

4. **Hybrid sensorless control solution for limp-home operation of automotive synchronous machines**. A novel hybrid sensorless strategy is presented in this chapter. First of all, a summary of the most common sensorless techniques for synchronous machines is provided. Then, the proposed sensorless structure, which combines a High Frequency Injection (HFI) technique (for low to zero speeds) and a Phase-Locked Loop (PLL) algorithm (for medium and high speeds) is presented. A solution to achieve a smooth transition between the PLL and the HFI strategies is also proposed, allowing to correctly determine the rotor position po-

---

[3] A detailed description of the electromagnetic model of a synchronous machine including magnetic saturation effect is also provided.

larity required by the HFI algorithm when PLL-to-HFI transitions are conducted. The developed strategy covers the required speed and torque range that guarantees sufficient limp-home capability to the vehicle, and also has speed reversal capabilities. These features are demonstrated in this chapter providing simulation and experimental evidences.

5. **Conclusions and future work**. This chapter summarizes the conclusions obtained from this work, as well as its main contributions. The publications resulting from this work are included in this chapter, and the future research lines are also addressed.

A. **Appendix: Vector transformations.** This appendix provides the mathematical fundamentals of the Park and Clarke transformations used in this work.

B. **Appendix: Second order SMC parameter tuning.** This appendix presents the mathematical approach needed for the determination of the second order SMC parameters required for the equivalent voltage calculations and the Super-Twisting algorithm (STA).

C. **Appendix: Experimental platform for EV propulsion system testing.** The automotive test bench used for the experimental validation of both contributions is described in this appendix.

Chapter 2

Electric vehicle drive systems: Electric machines and control

2.1 Introduction and overview of an EV powertrain architecture

In recent years, environmental issues such as pollution and global warming have encouraged researches on highly efficient systems. In this context, transport is one of the sectors with the highest contribution on greenhouse gas (GHG) emissions, contributing to the 27 % of the global CO_2 emissions [24]. Particularly, road transport represents 75 % of the total transport emissions [9, 25, 26]. For this reason, the automotive industry is one of the sectors that is actively involved in the reduction of such pollutants. The electrification of road transport is opening new opportunities and challenges to the mechanical, electronics and control engineers in the automotive industry [27–29].

In order to illustrate the promising future of vehicle electrification, figure 2.1(a) summarizes the results of a study carried out by the International Energy Agent (IEA), where the evolution of the Electric Vehicle (EV) stock up to 2030 is forecasted [1]. The Electric Vehicles Initiative (EVI) members forecast in 20 millions the EV stock by 2020, while the Paris Declaration on Electro-Mobility and Climate Change and Call to Action expects to reach 100

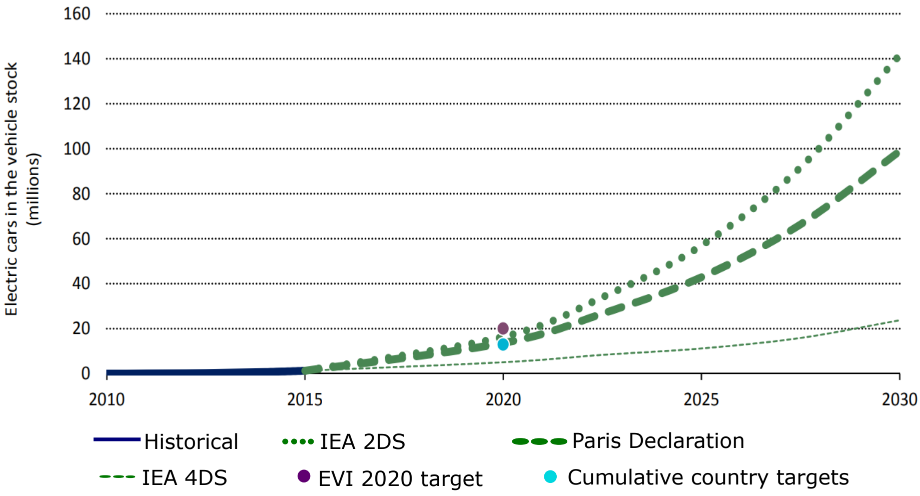

(a) Deployment scenarios for EV stock.

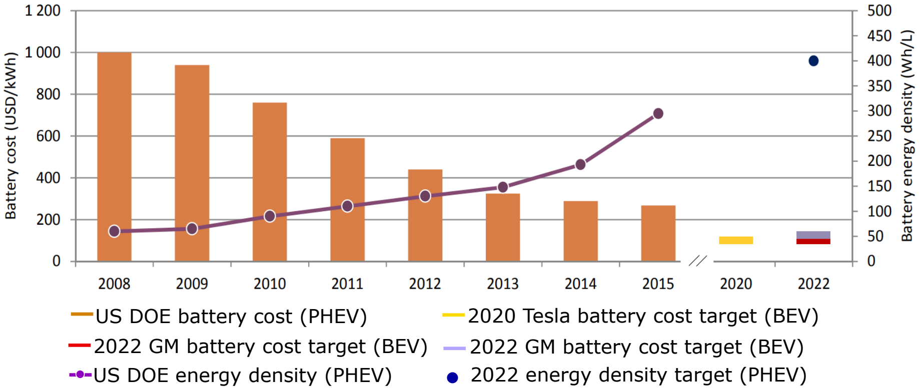

(b) Evolution of battery energy density and cost.

Figure 2.1: EV deployment targets and predictions on the evolution of battery energy densities [1].

million electric cars by 2030. The IEA 2DS foresees an even more ambitious deployment for EVs by 2030 (150 million). One of the most critical challenges to be overcome in order to meet the aforementioned targets is related with battery technologies. Although battery costs have been reduced by four from 2008 to 2015 (figure 2.1(b)), industry and government support is still required for the deployment of these technologies in the EV market. In addition, the need of increasing vehicle autonomies is encouraging researches to develop high density batteries to enable longer ranges at lower prices.

Additionally, the research, design and development of efficient, low cost, low weight, compact and reliable electric and hybrid propulsion systems (or powertrains) is required for the successful introduction of electrified vehicle technologies in the market [2, 3]. A number of vehicle architectures, such as Fuel Cell (FC) vehicles, battery powered EVs and Hybrid EVs (HEVs)[1] are currently being investigated [3, 30–32]. Among them, the most mature technologies with significant market penetration are battery powered EVs and series or parallel HEV configurations [33], whose architectures are represented in figure 2.2. In this context, this work will focus on EV vehicles, and other vehicular topologies such as hybrid and FC configurations will not be considered[2].

A general architecture of an EV powertrain configuration is shown in figure 2.3, where the hierarchy of the powertrain subsystems (responsible for the motion of the vehicle), the power connections (in green) and the communication lines between the vehicle Electronic Control Units (ECUs) based on CAN (Controller Area Network) protocol (in red) have been included [34–36]. In this sense, the EV powertrain can be split into the following subsystems:

1. Auxiliary. In general, this subsystem consists on the power steering unit, the hotel climate control unit and the auxiliary supply unit.
2. Energy storage. This subsystem includes the energy source (batteries, ultracapacitors, etc.), the energy control unit and the energy recharge unit.
3. Electric propulsion. This subsystem is comprised of a vehicle controller, power electronic converter(s), electric motor(s), mechanical transmission and driving wheels.

---

[1] In general and depending on their configuration, HEVs can be classified as series, parallel and series/parallel, among other configurations.

[2] However, it is important to point out that the contributions of this thesis regarding field weakening operation (chapter 3) and electric machine sensorless control (chapter 4) are focused on the electric propulsion drive; thus, these solutions could be implemented in any electrified vehicle configuration including synchronous machine based drives.

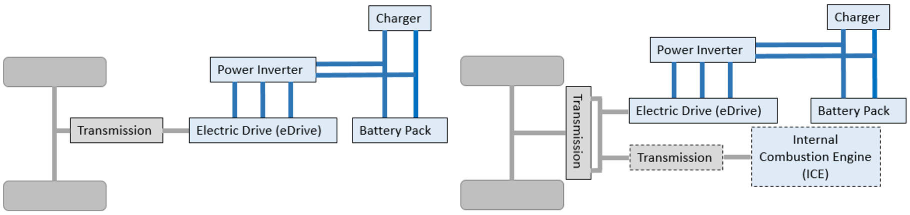

(a) Battery powered EV architecture. (b) Paralell HEV architecture.

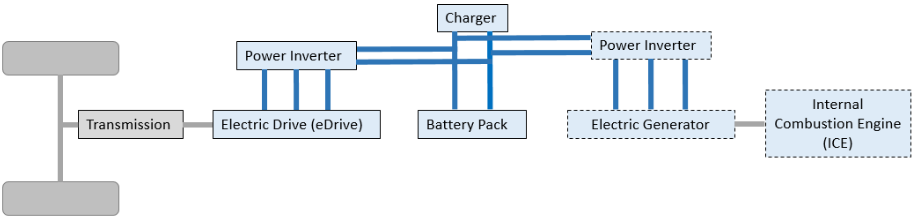

(c) Series HEV Architecture.

Figure 2.2: Typical EV and HEV architectures.

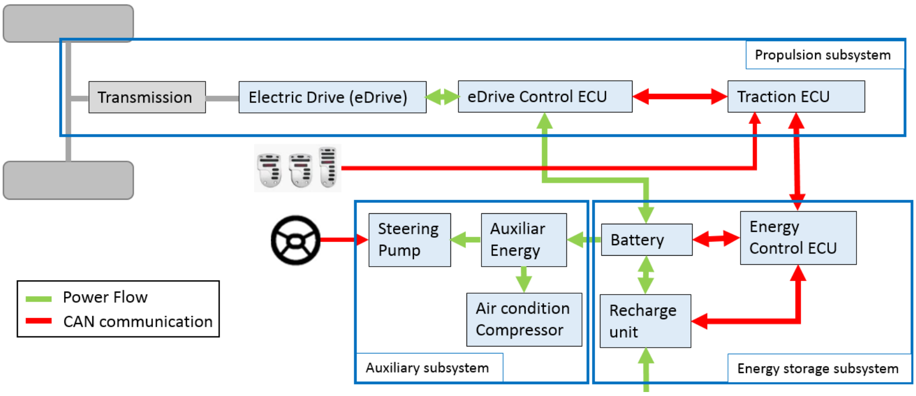

Figure 2.3: General EV powertrain configuration.

The auxiliary power supply subsystem provides the required power for all the EV auxiliaries, such as for the power steering units, adapting the voltage levels for each device. Auxiliary functionalities useful for passenger comfort, such as climate control, are also included in this powertrain subsystem [35, 36].

The Energy Storage Subsystem (ESS) stores the electrical energy in the battery and supplies it to the electric drive. The energy can be both provided or absorbed, depending on the vehicle's operating point and the state of charge (SoC) of the battery. The ESS must be sized to fulfill the range and acceleration requirements specified for the vehicle [37], and must also satisfy the required cycle and calendar life. The Energy Control ECU is the main control unit of the ESS. This unit manages the battery charge and is responsible for checking its correct performance during normal operation, sharing information with the powertrain management and control ECU, or with other vehicle domains. It protects and supervises all the battery cells, aiming to extend their life-cycle, while satisfying the electric drive power demands. Nowadays, one of the main research topics consists on the development of advanced methods for the precise estimation of the state-of-charge and state-of-health of the batteries [38, 39]. Additionally, special effort is being paid in the development of batteries with high cycling times and low maintenance costs. Lithium-ion (Li-ion) batteries with increased battery power capabilities [37] and other technologies such as Nickel-metal Hydride (NiMH) based batteries [40–42] or ZEBRA technology [37, 43] are being considered as promising candidates for future vehicles.

Finally, the electric propulsion subsystem is responsible for the conversion of the electric energy (stored in the battery or other energy storage technologies) into mechanical energy throughout the power electronics and the electric machine. Figure 2.4 shows the general diagram of the ECUs (traction ECU and eDrive control ECU) that constitute the EV propulsion subsystem architecture. The operation principle of the electric propulsion subsystem is as follows. The traction ECU collects the inputs requested by the driver and, depending on the vehicle and ESS subsystem status, calculates the optimum torque set-point in order to ensure a comfortable driving. It is important to note that an optimal energy management strategy must be included in the calculations [44–48]. The eDrive control ECU controls the operation of the electric motor to produce the required torque, according to the command received via CAN from the traction ECU. Then, the power electronics and the electric machine convert the electric energy into mechanical energy to propel the vehicle, or to enable regenerative braking for battery charging [49–51].

In this context, the work carried out in this thesis focuses on the research of advanced electric drive control strategies. Therefore, special interest is given

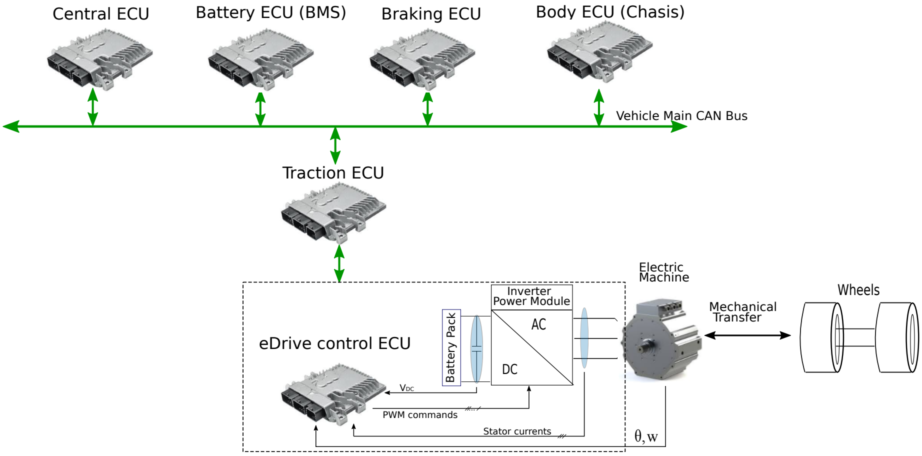

Figure 2.4: Wiring diagram and architecture of powertrain ECUs.

to the control algorithms to be implemented in the eDrive control ECU, as well as to the electric machine. In the following section, the most common machine topologies for EV applications are reviewed.

2.2 Machine technologies for vehicle electrification

2.2.1 Introduction

Electric machines (figure 2.4) are one of the key components of EV propulsion systems. The particular operation requirements of EVs, such as high speed operation, high acceleration rates and extreme ambient temperatures pose specific requirements for the electric machines to be used in EV applications [5, 52]. Additionally, these machines require high torque and power densities, high efficiencies throughout the full speed range and a high overload capacity [53–55]. High reliability, including fault-tolerance, is crucial [9], and low cost and simple construction is also desirable [56]. In order to meet the high power density requirements, the state of the art technologies require high density magnetic materials to produce the rotor flux, usually sintered neodymium-iron-boron (Nd-

FeB) alloys, and other Rare-Earth Elements (REE), such as dysprosium (Dy) and terbium (Tb) [8]. As an example, commercial HEVs and EVs such as Toyota Prius, Honda Insight, Chevrolet Volt, Nissan leaf and several vehicles from Renault and BMW use Permanent Magnet Synchronous Machines (PMSMs) based on REE materials [8].

The high demand of REEs in a number of sectors such as renewable energy systems and transportation has lead to a global concern about their possible depletion. From the economical and political perspective, the European Commission and the US Department of Energy have declared the continued use of REEs risky for their economies due to following reasons:

- Resource monopoly issues [9,57,58]. Up to date, China is the most important supplier of REEs (around 96 % of the worldwide production comes from this country).
- Risk of high price fluctuations [8, 59]. Due to this monopoly, sudden instabilities in REE prices may occur if, for example, export quotas from China are significantly reduced [60].

Due to these reasons, there is a growing need to replace or, at least, reduce the consumption of REEs. In this way, one interesting solution consists on recycling REEs, although in 2011 less than 1 % of REEs were recycled due to technological difficulties and lack of incentives [61, 62]. Researches focused on the reduction of the usage of heavy rare earth materials (such as Dy) are also being carried out [63, 64]. Another solution, which is attracting considerable attention in the automotive sector, is the replacement of rare-earth Permanent Magnets (PMs) by other materials, such alnico or ferrites. While the alnico PMs are not widely used due to their ease of demagnetization [9], the ferrite magnets are considered promising candidates to replace REE PMs because of their high electric resistivity, reduced price and their easy production [65, 66]. Finally, the usage of other rare-earth free machine technologies, such as Induction Machines (IMs), Switched Reluctance Machines (SRMs) and Synchronous Reluctance Machines (SynRMs) is also being considered for automotive applications [6].

In this sense, the following section reviews the commonly used machine technologies in the EV sector. This state of the art is concluded with a brief technological comparison between the reviewed alternatives.

2.2.2 Electric machine technologies including Rare-Earth Elements

In the last years, PMSMs have been widely used in EVs and HEVs propulsion systems. Although some researches have been carried out to reduce their magnet mass [63, 67], rare-earth PMs are commonly used in most of the applications [68, 69]. Since no excitation current is required, PMSMs have a high efficiency around the base speed [4] and high power density, which allows manufacturing light motors with high torque production capabilities. Compared to IMs, PMSMs of the same ratings can be constructed with between 30 % and 60 % less weight and with an efficiency improvement of 5% around the base speed [8].

However, PMSMs have some drawbacks, such as the need of additional current during field weakening operation, which leads to an increase of the power losses at high speed operation. Demagnetization problems induced by high rotor temperatures or high stator currents can also occur [9]. In addition, their overload capability is restricted by the magnet characteristics [53]. In any case, nowadays PMSMs are considered as the most suitable machines for EV and HEV applications [4, 70, 71]. According to a survey conducted in [6], up to 2010, 56 % of commercial electrified vehicles had PMSMs installed, showing a clear trend towards them in the near future.

Depending on the location of the magnets on the rotor, PMSMs can be broadly classified into two types (figure 2.5): Interior PMSMs (IPMSM), which have the permanent magnets buried inside the rotor, and Surface Mounted PMSMs (SM-PMSMs), which have their permanent magnets mounted on the surface of the rotor [4, 72]. In SM-PMSMs, the permanent magnets are directly facing the air gap and stator armature winding, making $L_d \simeq L_q$. Therefore, the reluctance torque is almost null and only magnetic torque can be produced.

In contrast and due to the salient poles, the d-axis reluctance in IPMSMs is higher than the one in the q-axis; as a consequence, $L_d < L_q$. The reluctance variation in the magnetic flux flow generates a reluctance torque in addition to the magnetic one, increasing the machine torque production capability [73, 74]. As in IPMSMs magnets are distant from the stator, less Foucault current losses are produced, causing less overheating. Thus, they are more protected against partial demagnetization [75].

In general, SM-PMSMs contain a smaller rotor diameter and inertia (which provides a good dynamic performance), while IPMSMs provide an extended field weakening operation range [72, 76]. Taking into account that saliency produces additional torque, increasing the power density, rare-earth IPMSM are the

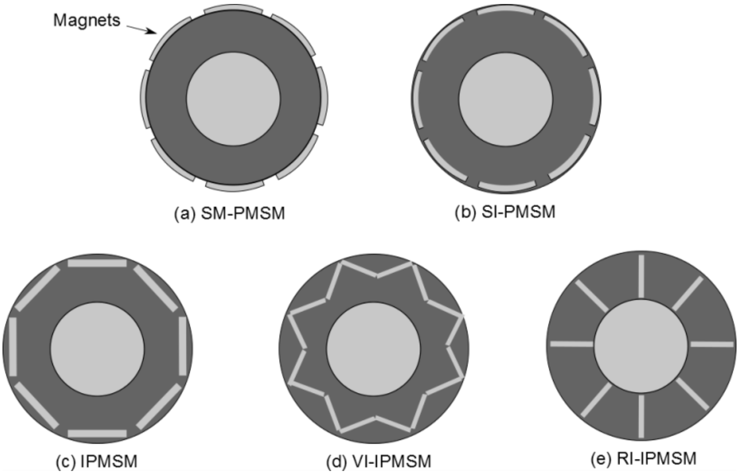

Figure 2.5: PMSM machine rotor topologies depending on the placement of the magnets.

most used machines in EV applications [4,77,78]. Finally, it must be taken into account that this saliency also facilitates the application of certain sensorless strategies [79–81], making this type of machine interesting for the implementation of electric drives including fault tolerant features.

2.2.3 Electric machine technologies without Rare-Earth Elements

Induction Machines

Up to date, Induction Machines (IMs) can be considered as one of the most matured technologies in AC machines [8,53]. According to [6], up to 2010, 29 % of electrified vehicles included this technology, being the trend towards IMs clear for the next years. Thus, currently this is the most popular rare-earth free technology. Some examples of commercial vehicles using IM technologies are the Tesla sport cars [82], General Motors EV1 [83] and a number of models provided by Renault, Daimler or BMW [8,84]. The most important advantages of this type of machine are their low cost, their robustness and their independence of PMs [85].

The dominant losses in IMs are the copper losses [53]. Due to the lower magnetization current in the range of field weakening, the copper losses are reduced and the IM provides a good efficiency at high speeds [9, 53]. Thus, it can be considered as a good alternative for sport cars which are intended to operate at high speeds.

In these type of machines, the constant power region can be extended up to 4 or 5 times the base speed, being this a key demand for current EVs [3, 9]. In contrast, IMs show a number of drawbacks, such as control limitations at low speeds and the need of high starting currents [8, 9]. The required magnetization current and the copper losses in the rotor decrease the efficiency around the base speed when compared to PMSMs. The magnetization current can be reduced including an air gap as small as possible, but this requires tight tolerances during fabrication, increasing production costs. Additional heat is produced in the rotor as a result of the losses, which requires cooling and restricts overload capabilities [53].

Due to their lower torque density and less efficiency, IMs are commonly used in full EVs and not in HEVs, where space restrictions are relevant.

Synchronous Reluctance Machines

Synchronous Reluctance Machines (SynRMs) can be considered as an alternative to conventional PMSMs. In these machines, the rotor is manufactured without magnets [86, 87] or assisted with small magnets (PM-assisted SynRM) [88].

The structure of a SynRM is similiar to an IPMSM. The main difference relies on the fact that the rotor is manufactured in a way that the asymmetry between the d- and q-axes is maximized. Therefore, the produced reluctance torque is maximized, the power density is increased and the field weakening performance at high speeds is improved [75]. Although conventional SynRMs do not have a high torque density, the design of a rotor with multiple flux barriers and the inclusion of ferrite PMs (to create a flux barrier on the quadrature axis) results in a high-saliency rotor (figure 2.6) with an increased power density and improved overall efficiency [8, 86, 89]. In terms of performance, the constant power region of a ferrite PM-assisted SynRM can be extended 3 or 4 times the base speed, resulting similar to the constant power region of an IPMSMs. As a drawback, demagnetization problems may arise at low operation temperatures, which can be avoided by preheating the machine before start or by following a proper design [90].

These features make the ferrite PM-assisted SynRM one of the most promising candidates for the next generation of EV and HEV drives [8, 9]. According

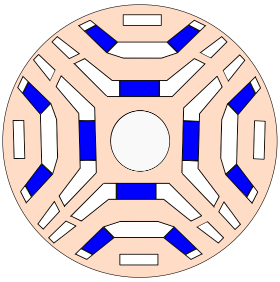

Figure 2.6: Typical location of ferrite magnets in a PM-assisted SynRM rotor.

to [91], modern ferrite PM-assisted SynRMs can produce 75 % of the torque of an IPMSM for the same size and liquid cooling technology. In this context, a significant amount of research has been carried out in the last years regarding SynRMs and PM-assisted SynRMs, with special attention on machine design and optimization aspects [92–95].

Switched Reluctance Machines

Switched Reluctance Machines (SRMs) can be considered as another promising rare-earth free machine candidates for EV applications [9]. In SRMs, the stator has wound field windings (similar to DC motors), and the rotor has neither windings, nor PMs (figure 2.7) [96]. Their operation is very different when compared to synchronous machines and IMs. At the excitation moment of each stator pole, the nearest rotor pole tends to come to the minimum reluctance position, producing torque [97].

SRMs have some advantages such as a simple structure, flexibility of control, high efficiency, lower cost, inherent fault tolerance and good thermal characteristic [3, 98, 99]. As the machine rotor does not have any windings or permanent magnets, this technology is suitable for very high speed drive applications [8, 100, 101]. SRMs offer a wide constant power region (up to 7 times the base speed) [9,102], being suitable for gearless EV drives. Their low rotor inertia provides fast acceleration capabilities, which is also an important requirement in the automotive industry [103].

High torque ripple, high noise and vibrations are the most important drawbacks of the SRM technology [104]. In order to produce maximum torque and reduce the torque ripple, many investigations have been carried out focused on

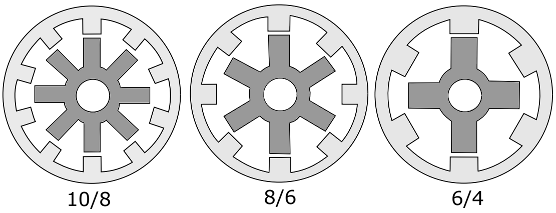

Figure 2.7: Most common SRM topologies.

the SRM design, [9, 105]. However, nowadays there are few available commercial EVs including SRM technologies. Range Rover and Toyota are currently working on this technology, which represents 1 % of the available electrified vehicles [6, 8, 9]. However, SRMs are expected to be potential candidates for the next generation of EVs.

2.2.4 Discussion on electric machine technologies

A great amount of scientific literature regarding the feasibility of these electric machine technologies for EV and HEV applications has been published in the last two decades. In this section, the most important conclusions provided by this literature have been briefly summarized.

According to several studies [6, 53–55, 84, 98], it is concluded that the most established machine technologies are the PMSMs and IMs. As concluded in [4, 106–108], considering their advantages and neglecting their high costs and REE dependency, PMSMs offer the best performance for their application in EV propulsion systems. However, the current effort in the research, development and design of rare-earth-free machine technologies is increasing the interest towards PM-assisted SynRMs or SRMs [9].

A qualitative comparison of the most relevant machine technologies considering a number of aspects and including economic factors is provided in table 2.1. It is concluded that the suitability of each machine technology would depend on the specific application, not being possible to assess the superiority of a particular technology over the others. However, considering their preponderance, the work carried out in this thesis will focus on synchronous machines with high reluctant torque, i.e., IPMSMs. Additionally, contributions will also be extended to non-rare earth based PM-assisted SynRM technologies, as they share the same control approaches with the IPMSMs.

Table 2.1: Performance comparison of current EV motor technologies.

Performance	**IMs**	**SRM**	**PMa. SynRM**	**PMSMs**
Fault tolerance	low	high	high	high
Power density	moderate	moderate	high	high
Efficiency	moderate	high	high	high
Cost	medium	low	medium	high
Wide speed range	☒	☑	☑	☑
Reliability	high	high	moderate	moderate
Control simplicity	☑	☑	☑	☑
Typ. control tech.	FOC/DTC	DITC/ADITC	FOC/DTC	FOC/DTC
Eff. at base speed	79-86 %	85-89 %	87-93 %	91-96 %
Torque ripple	low	high	low	low
Acoustic noise	low	moderate	moderate	moderate
Manufacturing costs	moderate	low	moderate	high

From the aforementioned literature, it can be also concluded that currently three-phase technologies are dominant for automotive synchronous machines. However, future trends are focused on providing fault tolerance to the propulsion system (in order to complete service under faulty conditions, although in derated operation mode). This desirable feature makes multiphase machines technologies an interesting research topic for their application in the automotive industry [109, 110]. Being the three-phase technology the most common in current EVs, the contributions of this thesis will be implemented for such architectures. However, multiphase systems could also benefit from the proposed control techniques, as these techniques could be particularized for the multiphase scenario.

2.3 Electromagnetic model of three-phase automotive synchronous machines

In this section, a detailed description of the electromagnetic model of a three-phase automotive synchronous machine is provided, as its knowledge is necessary in order to propose novel control algorithms, and is also required for the development of precise simulation models for the early design stages, where control algorithm validation is carried out.

2.3.1 Magnetic saturation on synchronous machines

When the total flux (which depends on the stator and rotor currents and on the PM flux) increases in the machine, saturation of the ferromagnetic parts may appear. This phenomena is known as magnetic field saturation, or just magnetic saturation. This effect occurs when an increase of the induced current does not increase the strength of the magnetic field proportionally [111]. As one of the main targets on automotive drives is to reduce the volume of the machine as much as possible, it is common that these machines exhibit high non-linearities (figure 2.8) due to the magnetic saturation phenomena.

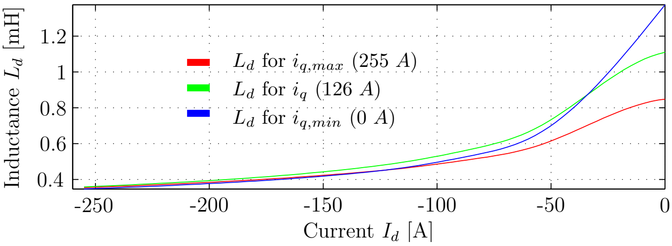

(a) Magnetic saturation effect in the d-axis inductance.

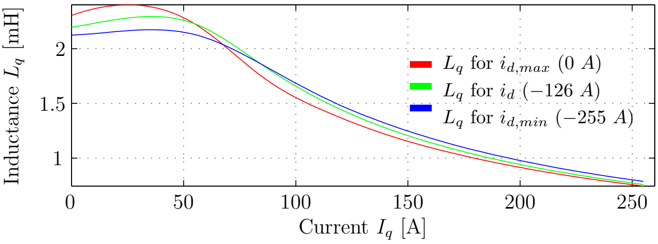

(b) Magnetic saturation effect in the q-axis inductance.

Figure 2.8: Magnetic saturation in the d- and q-axis inductances of an automotive PM-assisted SynRM.

For an IPMSM, when a high current value is applied in the q-axis, the iron saturates and, therefore, the d- and q-axis inductance values decrease, reducing the flux production capability of the machine [112]. On the other hand, when high negative d-axis current values are applied, they generally oppose to the saturation produced by the permanent magnet flux and the iron desatures [112]. As a result, the d-axis inductance increases. However, in some particular cases, such as in PM-assisted SynRMs with low PM flux linkage, the effect of the d-axis current can produce the opposite effect, introducing more saturation and reducing the inductances. As an example, the highly non-linear inductances of the PM-assisted SynRM machine studied in this thesis are presented in Figure 2.8, showing the aforementioned tendencies.

Inductances determine a large part of the electric machine behaviour and play an important role in the electromagnetic torque and voltage expressions, affecting directly the control precision, field weakening operation and dynamics. The particular requirements of EVs, such as the design of compact but powerful drives makes magnetic saturation not negligible and therefore required in the development of high fidelity machine models [112–115]. Taking this into account, in the following, the mathematical expressions that describe the behaviour of an automotive synchronous machine will be reformulated considering the magnetic saturation effect.

2.3.2 Synchronous machine dq model

Once the voltage equations of a three-phase synchronous machine are transformed into the synchronous dq reference frame (appendix A), the electromagnetic model of the machine can be based on the following stator voltage equations:

$$v_d = R_s i_d + \frac{d\Psi_d(i_d, i_q)}{dt} - \omega_e \Psi_q(i_d, i_q), \tag{2.1}$$

$$v_q = R_s i_q + \frac{d\Psi_q(i_d, i_q)}{dt} + \omega_e \Psi_d(i_d, i_q), \tag{2.2}$$

where v_d, v_q, i_d and i_q are the d- and q-axis stator voltages and currents; R_s is the stator resistance, ω_e is the motor electrical speed and $\Psi_d(i_d, i_q)$ and $\Psi_q(i_d, i_q)$ are the magnetic fluxes considering the non-linearities produced by the magnetic saturation. The mathematical relationship between the d- and q-axis fluxes, the $L_d(i_d, i_q)$ and $L_q(i_d, i_q)$ inductances and the PM flux $\Psi_{pm}(i_q)$ can be described as follows [112]:

$$\Psi_d(i_d, i_q) = L_d(i_d, i_q) i_d + \Psi_{pm}(i_q), \tag{2.3}$$

$$\Psi_q(i_d, i_q) = L_q(i_d, i_q) i_q. \tag{2.4}$$

As the influence of i_d in the saturation of the d-axis inductance and the PM flux cannot be easily decoupled, for simplicity, it is considered that i_d does not affect Ψ_{pm} and all its contribution influences the value of L_d [112].

Replacing (2.3) and (2.4) in (2.1) and (2.2), the stator voltage equations can be rewritten as:

$$v_d = R_s i_d + \frac{d}{dt}[L_d(i_d,i_q)i_d + \Psi_{pm}(i_q)] - w_e L_q(i_d,i_q)i_q = \tag{2.5}$$

$$= R_s i_d + L_d(i_d,i_q)\frac{di_d}{dt} + i_d\frac{\partial L_d(i_d,i_q)}{\partial i_d}\frac{\partial i_d}{dt} + i_d\frac{\partial L_d(i_d,i_q)}{\partial i_q}\frac{\partial i_q}{dt} + + \frac{\partial \Psi_{pm}(i_q)}{\partial i_q}\frac{\partial i_q}{dt} - w_e L_q(i_d,i_q)i_q, \tag{2.6}$$

$$v_q = R_s i_q + \frac{d}{dt}[L_q(i_d,i_q)iq] + w_e[L_d(i_d,i_q)i_d + \Psi_{pm}(i_q)] = \tag{2.7}$$

$$= R_s i_q + L_q(i_d,i_q)\frac{di_q}{dt} + i_q\frac{\partial L_q(i_d,i_q)}{\partial i_d}\frac{\partial i_d}{dt} + i_q\frac{\partial L_q(i_d,i_q)}{\partial i_q}\frac{\partial i_q}{dt} + + w_e[L_q(i_d,i_q)i_q + \Psi_{pm}(i_q)]. \tag{2.8}$$

Considering that the variation of the inductances with respect to the currents are small enough during transients, the following simplifications can be considered:

$$\frac{\partial L_d(i_d,i_q)}{\partial i_d} \cong 0; \frac{\partial L_q(i_d,i_q)}{\partial i_d} \cong 0; \tag{2.9}$$

$$\frac{\partial L_d(i_d,i_q)}{\partial i_q} \cong 0; \frac{\partial L_q(i_d,i_q)}{\partial i_q} \cong 0; \frac{\partial \Psi_{pm}(i_q)}{\partial i_q} \cong 0. \tag{2.10}$$

Thus, the machine electromagnetic model can be reformulated, obtaining the equations that correspond to the well known variable DQ (VQD) modelling approach [116]:

$$v_d = R_s i_d + L_d(i_d,i_q)\frac{di_d}{dt} - \omega_e L_q(i_d,i_q)i_q, \tag{2.11}$$

$$v_q = R_s i_q + L_q(i_d,i_q)\frac{di_q}{dt} + \omega_e[L_d(i_d,i_q)i_d + \Psi_{pm}(i_q)]. \tag{2.12}$$

The VDQ approach is accurate enough for this particular application. However, if the application requires a more accurate model during transients, it is recommended to use the flux based equations given by (2.1) and (2.2). Although other machine model approaches can be found in the scientific literature [117,118], in this work VDQ and flux based machine models have only been considered.

Once the voltage equations have been determined, the electromagnetic torque can be determined using the following expression:

$$T_{em} = \frac{3}{2}P[\Psi_d(i_d, i_q)i_q - \Psi_q(i_d, i_q)i_d], \tag{2.13}$$

where P is the machine pole-pair number.

Taking into account (2.3) and (2.4), (2.13) can be rewritten as follows:

$$T_{em} = \frac{3}{2}P\{\Psi_{pm}(i_q)i_q + [L_d(i_d, i_q) - L_q(i_d, i_q)]i_d i_q\}. \tag{2.14}$$

From (2.14), it can be deduced that the total torque production of a synchronous machine is obtained as a combination of two terms, i.e., the magnetic torque $3/2P\Psi_{pm}(i_q)i_q$ and the reluctance torque $3/2P\,[L_d(i_d, i_q) - L_q(i_d, i_q)]\,i_d i_q$ components.

As it has been advanced at the beginning of this chapter, in the particular case of SM-PMSM (where $L_d(i_d, i_q) \cong L_q(i_d, i_q)$), the reluctance torque can be neglected, and only the magnetic torque produced by the PMs is responsible for the total torque production. On the other hand, considering a conventional synchronous machine with a certain degree of saliency ($L_d(i_d, i_q) \neq L_q(i_d, i_q)$), it can be derived that the higher the difference $L_d(i_d, i_q) - L_q(i_d, i_q)$, the higher the reluctant torque. In this sense, the reluctance ratio $L_q(i_d, i_q)/L_d(i_d, i_q)$ is commonly defined. Therefore, these machines should be designed in a way that this ratio is maximized in order to obtain the sufficient torque from the reluctance torque component and maximize its power density.

2.4 Torque control of synchronous machines

2.4.1 Introduction

As stated in section 2.1, the eDrive control ECU is responsible for the torque production (commanded by the traction ECU) of the electric machine. Despite a variety of control approaches have been studied in recent years, such as non linear adaptive control techniques [119, 120], fuzzy logic based strategies [121, 122] or Model Predictive Controls (MPC) [123, 124], PI based Field Oriented

Control (FOC) and Direct Torque Control (DTC) are the most commonly used control approaches for EV synchronous machines [125–127].

DTC control techniques directly control the electromagnetic torque and the stator flux modulus, not requiring current regulator loops [10, 128]. The absence of coordinate transforms (appendix A) and PI controllers, together with the required low computational burden and their simple implementation make DTC control a widely adopted control strategy [125, 127, 129]. In addition, the regulators have little sensitivity to detuned parameters when compared to other control approaches [127]. In recent years, many researches have been carried out for the integration of advanced controllers such as fuzzy logics [130] or model predictive controls [131, 132] with traditional DTC strategies. However and in general, DTC produces high current and torque ripples, generating high acoustic noise [125, 133]. DTC also complicates torque control at low speed operation [125, 126] and presents variable switching frequency behaviour. Solutions can be implemented to overcome the aforementioned limitations [127], such as the implementation of DTC schemes for constant switching frequency operation [134,135], introduction of advanced control techniques such as fuzzy or neuro-fuzzy strategies [136,137] or advanced flux estimators in order to improve the low speed behaviour [138].

One of the main advantages of DTC is its fast dynamic response. However, in this particular application, such dynamics are not required, as transient must be slow enough to ensure passenger's comfort. Thus, considering the disadvantages related to the DTC approach, the most mature FOC approach has been selected in this thesis. Although the PI based FOC is the most common control approach, non linear controllers such as second order Sliding Mode Control (SMC) can be considered as appropriate when the synchronous machine to be controlled presents high non linearities [139]. In this context, this section focuses in the review and detailed analysis of both the PI based and second order SMC based FOC techniques.

2.4.2 Field oriented control

Proportional integral based FOC control

The FOC strategy consists of tracking the torque indirectly by controlling the measured stator currents. Figure 2.9 shows the general diagram of the FOC approach. It is based on the projection of the stator three-phase currents (i_U, i_V, i_W) into a two coordinate system (i_d, i_q) using the well known Clarke and Park transformations (appendix A). These projections lead to a control

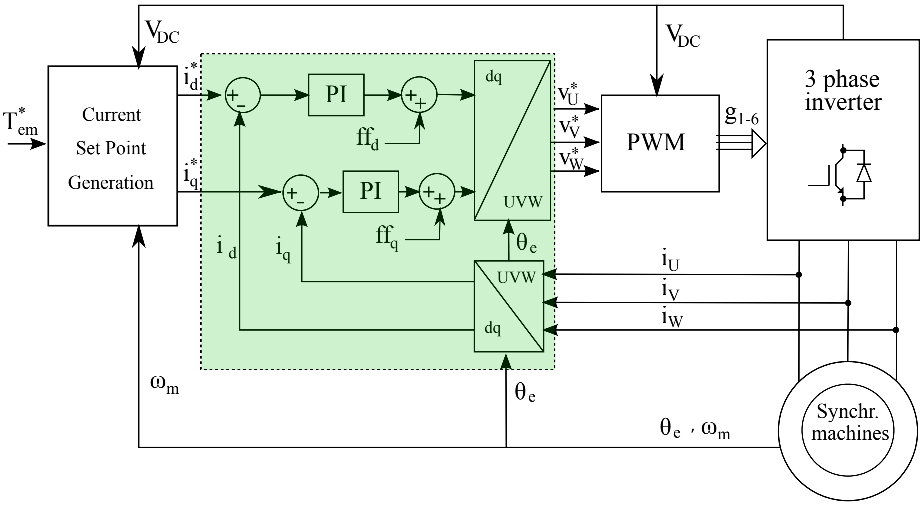

Figure 2.9: Conventional FOC control structure including the required optimum reference currents determination block.

structure similar to that of a DC machine [140]. Because the current space vector in the *dq* reference frame is static, the PI controllers operate on DC, rather than with sinusoidal signals. This isolates the controllers from the time variant winding currents and voltages. The d- and q-axis currents must track the desired i_d^* and i_q^* set points in order to achieve the desired torque (the generation of such set points will be thoroughly detailed in chapter 3). Finally, the reference voltages $\mathbf{v}_{UVW}^*$ obtained from the controller are synthesized in the machine stator using a modulation strategy such as Pulse Width Modulation (PWM) [141] or Space Vector Modulation (SVM) [142].

The addition of the feed-forward terms containing the back-EMF allow to decouple the direct and quadrature axes, improving the transient performance of the system. These terms, defined as ff_d and ff_q (figure 2.9) are [143]:

$$ff_d = -\omega_e L_q(i_d, i_q) i_q, \tag{2.15}$$

$$ff_q = \omega_e [L_d(i_d, i_q) i_d + \Psi_{pm}(i_q)]. \tag{2.16}$$

PI regulators have been traditionally implemented in the Laplace domain for multiple applications. However, it is highly recommended to work in the

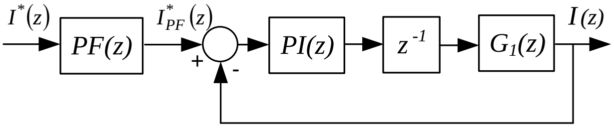

Figure 2.10: Simplified current control diagram in the z domain including a pre-filter.

z domain when higher accuracy is required [144]. A simplified diagram of the current control in the z domain is shown in figure 2.10, where the back-EMF component has not been considered for simplicity. The diagram includes the following elements:

- A plant transfer function in the z domain $G(z)$, expressed as:

$$\begin{aligned} G(z) &= z^{-1}(1-z^{-1})Z\left\{\frac{G_1(s)}{s}\right\} = \\ &= z^{-1}(1-z^{-1})Z\left\{\frac{1/R}{s[(L/R)s+1]}\right\} = \frac{1}{R}\frac{1-e^{-aT}}{z(z-e^{-aT})}, \end{aligned} \tag{2.17}$$

  where $a = R/L$ and T is the controller sampling time.

- The delays introduced in the system due to the time required by the DSP (Digital Signal Processor) for current sampling and control execution are taken into account including one sample delay (z^{-1}).

- The controller PI transfer function is derived from the corresponding expression in the Laplace domain. Adopting a backward Euler approximation, the PI transfer function can be expressed as:

$$PI(z) = K_p + K_i T\frac{z}{z-1} = \frac{(K_p + K_i T)z - K_p}{z-1}, \tag{2.18}$$

  where K_p and K_i are the proportional and the integral gains of the PI regulators.

- A pre-filter (PF) to cancel additional poles and zeros appearing in the system.

From figure 2.10, the Open Loop $OL(z)$ and the Closed Loop $CL(z)$ current transfer functions can be obtained as:

$$OL(z) = \frac{(K_p + K_iT)z - K_p}{z-1}\frac{1}{R}\frac{1-e^{-aT}}{z(z-e^{-aT})}, \tag{2.19}$$

$$CL(z) =$$
$$= \frac{(K_p + K_iT)(1-e^{-aT})(z - \frac{K_p}{K_p+K_iT})}{R\{z^3 - z^2(-1-e^{-aT}) + z[e^{-aT} + \frac{1}{R}(K_p+K_iT)(1-e^{-aT}) - \frac{K_p}{R}(1-e^{-aT})]\}}. \tag{2.20}$$

The general characteristic equation of the $CL(z)$ transfer function is defined as:

$$z^2 - 2e^{-w_nT}z + e^{-2w_nT}, \text{ where } T_{s,2\%} = \frac{5.8}{\xi w_n}, \tag{2.21}$$

being $T_{s,2\%}$ the settling-time (set to 2 %) and being ξ the damping factor. In this thesis, ξ has been set to 1 to avoid any overshoot.

Both the additional sample delay (figure 2.10) and the extra zero of the PI regulator in (2.18) include an additional pole and zero (c and b, respectively) in (2.21):

$$T(z) = K\frac{z-b}{(z^2 - 2e^{-w_nT}z + e^{-2w_nT})(z-c)}. \tag{2.22}$$

Therefore, the PI regulator adjustment consists of making (2.20) equal to (2.22). The additional pole and zero are then cancelled throughout the pre-filter (figure 2.10), whose expression is:

$$PF(z) = \frac{(1-b)(z-c)}{(1-c)(z-b)}. \tag{2.23}$$

In this way, the dynamic of the closed loop system matches perfectly with the second order equation of (2.21). Solving the system using the pole placement technique, the following solutions are obtained for c, K_p, K_i and b:

$$c = 1 + e^{-aT} - 2e^{w_n T}, \tag{2.24}$$

$$K_p = \frac{Rce^{-2w_n T}}{1 - e^{-aT}}, \tag{2.25}$$

$$K_i = \frac{1}{T}\left[\frac{R(e^{-2w_n T} + 2e^{-w_n T}c - e^{-aT})}{1 - e^{-aT}} - K_p\right], \tag{2.26}$$

$$b = \frac{K_p}{K_p + K_i T}. \tag{2.27}$$

If the magnetic saturation effect is taken into account, it is possible to improve the regulator's dynamic response taking into account its influence in the L_d and L_q values for the calculation of the control parameters. However, the proportional and integral gains of the PI regulator are commonly adjusted using nominal R and L values. As a result, the response of the controller changes when the machine parameters highly deviate from the nominal ones, although this deviations can be assumed in this particular application.

Sliding mode based FOC

The SMC is a nonlinear control strategy commonly characterized for its accuracy and robustness. The operation principle of this technique consists on designing a particular surface (sliding surface) to where the system states are addressed. Once there, the SMC selects a control law to keep the states on the neighbourhood of the sliding surface [145]. Robustness against parameter variations is one of the major advantages of this strategy, making the overall performance of the current closed-loop based on SMC very reliable [146]. Thus, it becomes an interesting candidate for controlling highly non-linear machines, as is the case of automotive IPMSM and PM-assisted SynRM machines.

Generally, two approaches based on the SMC technique can be followed:

- Standard (or first-order) SMC: This approach is considered as an appropriate solution for controlling electric drives connected to switching power converters [146, 147]. Two of the main benefits of the first order SMC are its high dynamic response during transients and its robustness. Even though using this approach the switching frequency of the power converter is variable, techniques to fix this frequency have been proposed in the scientific literature [145,148,149]. The discontinuous high frequency switching control can produce oscillations and many problems in different areas like the control of mechanical systems (chattering phenomenon) [139,150].

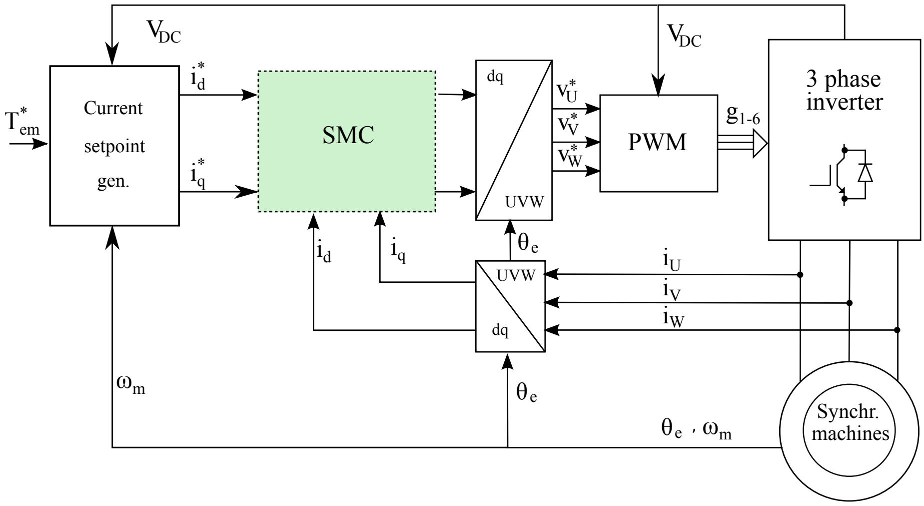

Figure 2.11: SMC torque control for synchronous machines.

- High-order SMC. Among them, the second order SMC is the most commonly used [151, 152]. The application of a second order SMC allows to retain the robustness characteristics of the first order SMC control algorithm at a fixed switching frequency. Additionally, possible chatter can be reduced [150, 151].

This work focuses on the second order SMC due to its advantages and suitability for the torque control of EV synchronous machines. Similar to the PI based FOC control, the second order SMC can be effectively used for current regulation and, thus, indirect torque regulation throughout optimal current set points (figure 2.11). In this sense and aiming to achieve satisfactory tracking performance for i_d and i_q, the following sliding functions are adopted [150]:

$$s_{i_d} = e_{i_d} + c_d \int e_{i_d} dt, \tag{2.28}$$

$$s_{i_q} = e_{i_q} + c_q \int e_{i_q} dt, \tag{2.29}$$

where $e_{i_d} = (i_d^* - i_d)$ and $e_{i_q} = (i_q^* - i_q)$, being c_d and c_q positive constants. The integral terms of (2.28) and (2.29) are incorporated to remove steady state errors that may arise in practice. Satisfactory tracking is achieved when $ds_{i_j}/dt = 0$, being $j = \{d, q\}$.

Taking the time derivative of the sliding functions, the following space state expressions are obtained:

$$\frac{ds_{id}}{dt} = \frac{de_{i_d}}{dt} + c_d e_{i_d} = \frac{d}{dt}(i_d^* - i_d) + c_d e_{i_d}, \tag{2.30}$$

$$\frac{ds_{iq}}{dt} = \frac{de_{i_q}}{dt} + c_q e_{i_q} = \frac{d}{dt}(i_q^* - i_q) + c_q e_{i_q}, \tag{2.31}$$

where $d(i_d^*)/dt \simeq d(i_q^*)/dt \simeq 0$ considering constant or slowly variant current references. Introducing (2.1) and (2.2) into (2.30) and (2.31), the motor dynamics can be rewritten as:

$$\frac{ds_{id}}{dt} = -\frac{di_d}{dt} + c_d e_{i_d} = -\frac{-R_s i_d + w_e \Psi_q(i_d, i_q)}{L_d(i_d, i_q)} - \frac{v_{d,ref}}{L_d(i_d, i_q)} + c_d e_{i_d}, \tag{2.32}$$

$$\frac{ds_{iq}}{dt} = -\frac{di_q}{dt} + c_q e_{i_q} = -\frac{-R_s i_q - w_e \Psi_d(i_d, i_q)}{L_q(i_d, i_q)} - \frac{v_{q,ref}}{L_q(i_d, i_q)} + c_q e_{i_q}. \tag{2.33}$$

where $v_{d,ref}$ and $v_{q,ref}$ are the voltages references to be applied by the SMC. This voltages can be obtained as [150]:

$$v_{d,ref} = v_{d,ST} + v_{d,eq}, \tag{2.34}$$

$$v_{q,ref} = v_{q,ST} + v_{q,eq}. \tag{2.35}$$

The terms $v_{d,eq}$ and $v_{q,eq}$ correspond to the equivalent control signals, which are obtained forcing $ds_{i_d}/dt = 0$ and $ds_{i_q}/dt = 0$ in (2.32) and (2.33), resulting in:

$$v_{d,eq} = \left[c_d e_{i_d} - \frac{-R_s i_d + w_e \Psi_q(i_d, i_q)}{L_d(i_d, i_q)} \right] L_d(i_d, i_q), \tag{2.36}$$

$$v_{q,eq} = \left[c_q e_{i_q} - \frac{-R_s i_q - w_e \Psi_d(i_d, i_q)}{L_q(i_d, i_q)} \right] L_q(i_d, i_q). \tag{2.37}$$

The components $v_{d,ST}$ and $v_{q,ST}$ are computed applying the Super-Twisting Algorithm (STA) [151]:

$$v_{j,ST} = L_j \left[\lambda_j |s_{i_j}|^{1/2} sgn(s_{i_j}) + \Omega_j \int sgn(s_{i_j}) dt \right], \tag{2.38}$$

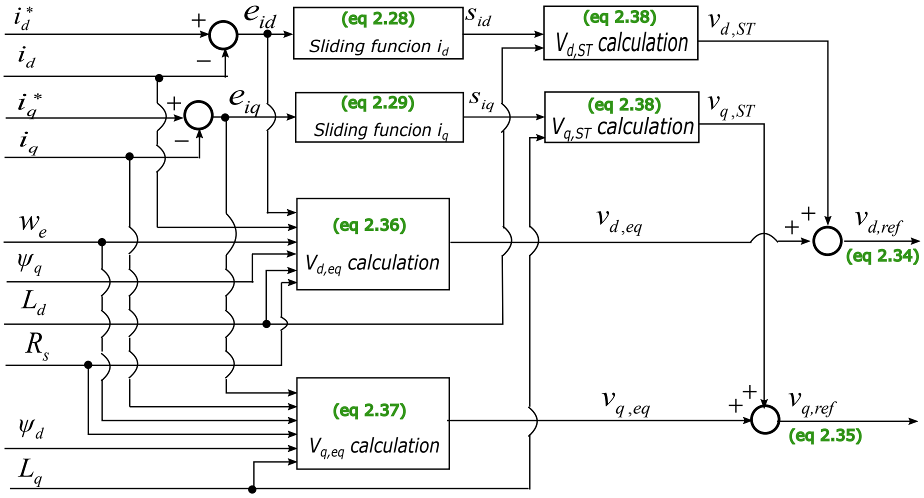

Figure 2.12: Diagram of the second order SMC control algorithm for synchronous machines.

where λ_j and Ω_j are positive gains to be tuned, being $sgn(s_{i_j}) = s_{i_j}/|s_{i_j}|$. The goal of the first terms of (2.38) is to guarantee that the sliding surfaces $s_{i_j} = 0$ are reached at finite time. In this sense, figure 2.12 shows the complete diagram of the second order SMC, including the calculations of both equivalent and ST terms.

Appendix B summarizes the mathematical equations required for properly tuning the second order SMC algorithm, including the equivalent voltages and STA parameters.

It is important to note that equivalent voltages are not strictly necessary for the second order SMC. However, they include a number of benefits [150]:

- They improve the system's transient response.
- The more accurately they are calculated, the lower is the control effort left to the STA algorithm.
- Although equivalent voltage components are machine parameter dependant, they do not decrease the control algorithm robustness, as it relies on the STA.

- Their incorporation simplifies the calculation of the sliding function constants c_d and c_q, as well as the STA constants λ_d, λ_q, Ω_d and Ω_q.

If magnetic saturation phenomena is not negligible, equivalent voltages of (2.34) and (2.35) can be calculated estimating the inductances L_d, L_q and the magnetic fluxes Ψ_d, Ψ_q from Look-up Tables (LUT) containing current dependant FEM or experimental data of such parameters, and using the currents i_d and i_q for their estimation.

2.4.3 High speed operation

Future trends in the EV industry include the usage of high speed electric machines[3]. In this way, their volume and size can be reduced when increasing their maximum operation speed while maintaining the power production capabilities, as less torque is required to deliver the same power [5]. As an illustrative example, the 3^{rd} generation Toyota Prius (launched in 2010) increased the motor mechanical speed from its previous version (2^{nd} generation, launched in 2006), from 6000 rpm up to 13900 rpm, keeping the same nominal power of 50 kW [8]. It is even expected in the near future that EV machines will operate at mechanical speeds beyond 15000 rpm [5].

High speed operation of automotive synchronous machines leads to a number of challenges to be overcome in order to ensure a correct system performance in the whole speed operation range. As the PM-assisted SynRM used in this thesis for the experimental validation of the proposed control algorithms can be considered as a high speed machine (with a maximum operation speed of 12000 rpm), high speed control issues become relevant in this particular case.

On the one hand, as the electrical frequency $f_e = w_e/2\pi$ increases proportionally to the electrical speed, this implies that a sufficiently high sampling frequency is required in order to ensure a correct reconstruction of the measured signals, such as stator currents or electrical rotor position [155–157]. As a consequence and depending on how fast the machine operates, an increase in the power electronics switching frequencies can be required for proper torque regulation, which, in some cases, is not possible using conventional Silicon (Si) based IGBT (Insulated Gate Bipolar Transistor) technology [12, 13, 158, 159]. The physical limits of Si devices give rise to a new generation of power devices based on Wide Band Gap (WBG) semiconductor materials, where the

---

[3] Electric machines are considered as high speed machines (HSEM) if they can operate beyond 10000 rpm [153, 154].

Silicon Carbide (SiC) and Gallium Nitride (GaN) are currently the most matured technologies [14, 15, 158, 160]. From the control implementation point of view, the limited computational capabilities of Digital Signal Processors (DSP) makes Field Programmable Gate Array (FPGA) technologies suitable for the implementation of high sampling rate control algorithms [16, 161, 162].

However, in some cases as in this thesis where only Si technology is available, it is necessary to rely on advances control approaches to obtain a correct torque regulation at high speeds [163,164], or consider techniques that compensate the effect of delays on the controllers. In this sense, this thesis has adopted a phase advance strategy in order to improve the torque regulation at high speeds [165]. When control approaches that make use of vector transformations are used (appendix A), it is important to consider the delays introduced in the system due to the measurements and control execution.

Considering the particular case of a FOC scheme including a symmetric Pulse Width Modulation (PWM) strategy (figure 2.13(a)), the voltage control output, calculated in the instant k (V_k^*) is effectivelly applied in the instant k+1.5. During this small time interval, the machine has rotated and, as a consequence, the angle to be applied to the inverse Park transformation should be advanced [8, 165, 166]:

$$\theta_e' = \theta_e + 1.5\omega_e T_s, \tag{2.39}$$

being T_s the control execution period. Similarly, when using asymmetric PWM (figure 2.13(b)), the delay should be compensated in the angle used for the inverse Park transformation as follows:

$$\theta_e' = \theta_e + 2\omega_e T_s. \tag{2.40}$$

It is important to remark that this solution extends the controllable speed range, but has its limitations [165].

On the other hand, when increasing the drive speed, the back-EMF of synchronous machines increases and, due to the limitation of the available DC-link voltage, field weakening control is mandatory [107,167]. In high speed machines, the field weakening operation region can be very large. Thus, robust field weaking control becomes relevant [168, 169]. During field weakening control, the stator voltage must be properly controlled in order to avoid uncontrolled regeneration. However, parameter uncertainties and non-linealities can make field weakening control of synchronous machines with high reluctance-ratio challenging [166].

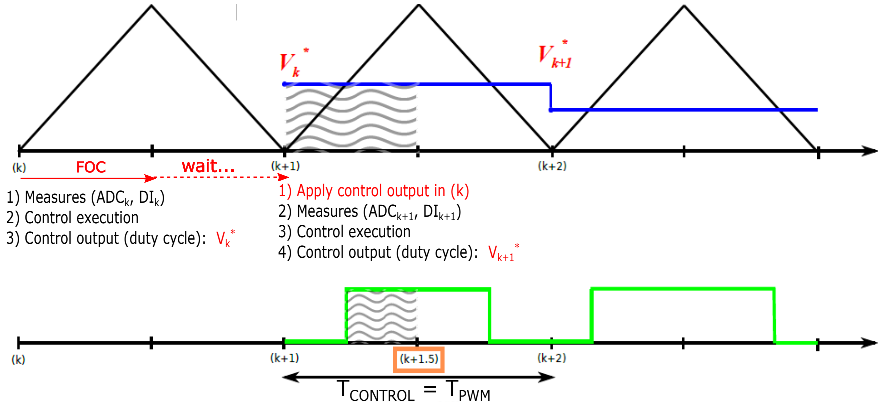

(a) Symmetric PWM.

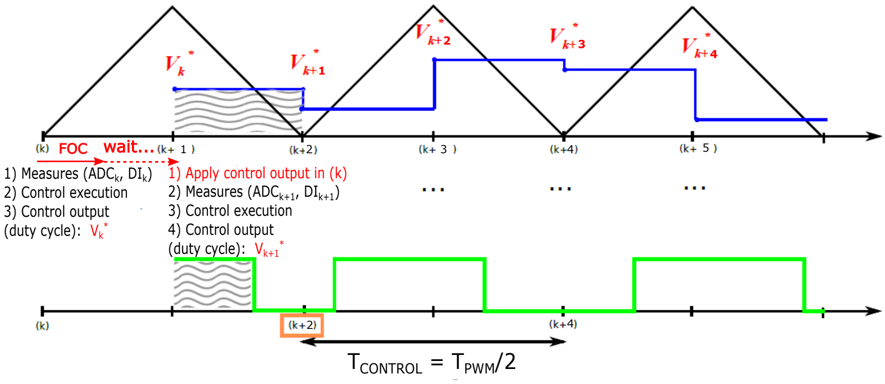

(b) Asymmetric PWM.

Figure 2.13: Symmetric and asymmetric PWM pulse generation and the delays associated with their usage.

2.4.4 Fault tolerance and limp-home capability

High reliability is crucial for EV applications [9, 17, 170]. As discussed in section 2.2.4, multiphase machine technologies are an interesting research topic due to their intrinsic fault tolerance. However, since three-phase synchronous machines are the most established technologies in EV drive propulsion systems, a great number of works regarding fault detection and fault-tolerant control of three-phase systems are available in the scientific literature [18, 170].

Fault detection and fault tolerance are important issues not only for the reliability of the drive system, but also for the proper operation of the vehicle under faulty conditions. These features make the development of Prognostic and Health Management Systems (PHMS) an attractive option to increase the safety and availability of EV end-users [17, 19, 171]. These methods rely on a Failure Mode and Effect Analysis (FMEA) where, once failures are classified by their risk priority, the degradation mechanisms that cause them are identified [20, 172–174]. From the FMEA analysis, a selection of the most critical degradation mechanisms and their corresponding measurable signals is conducted. Finally, the selected degradation mechanisms are taken into account in the development of PHMS strategies to predict system failures [175]. In general, most of the studies are focused on power semiconductor devices [176–179] and stator windings [180–184].

Conventional automotive synchronous machine control strategies require at least one DC voltage sensor, two or three current sensors and a resolver (or encoder) to ensure a correct control performance. By carrying out an FMEA, it is deduced that a resolver sensor failure would involve catastrophic consequences, as it provides the rotor position, mandatory for field orientation and also for closed-loop control. Taking into account the road vehicles functional safety standards (ISO26262), where fault tolerance against speed and position measurement failures must be ensured, many researches concerning position/speed estimation techniques (also known as sensorless control) are currently being carried out [21, 170, 185]. Although nowadays the elimination of such sensor is not straightforward, many studies are focused on the development of sensorless strategies which allow drivers to reach their destination safely despite the occurrence of a sensor fault. This concept is called limp-home operation [22, 23, 186, 187].

2.5 Conclusions

In this chapter, the fundamentals of an EV propulsion system have been reviewed. A detailed description of the powertrain domain and its main functional blocks has been provided, with an special emphasis in the electric drive and the control algorithms to be implemented in the eDrive control ECU.

Taking into account the particular requirements and working conditions of EVs, nowadays PMSMs are considered as the most suitable technologies for their application in the automotive sector. However, the increasing effort in the development of rare-earth free machines makes the PM-assisted SynRM technology to be considered as an interesting alternative for automotive applications. The work of this thesis will be focused on automotive IPMSM due to their high reluctant torque. Additionally, such contributions will be extended to rare-earth free PM-assisted SynRM drives, as they share the same control approaches.

Concerning control aspects, PI based FOC is one of the most matured control approaches for synchronous machines. However, taking into account the magnetic saturation effect of automotive drives, the usage of non linear control strategies such as the SMC based FOC are considered as appropriate. Although the SMC itself is robust enough against parameter deviations, the current references obtained throughout analytic calculations are highly dependent on machine electrical parameters. The high non-linearities together with electrical parameter variations due to machine ageing, manufacture tolerances and temperature dependency lead to possible controllability problems in the field weakening region. Due to the aforementioned reasons, it is confirmed the importance of relying on a robust field weakening control to ensure correct EV performance in the whole operation range.

One of the most important requirements in EV applications is the fault tolerance capability, where not only the reliability of the drive but also its proper operation under faulty conditions must be guaranteed. Recent studies focus their efforts in the detection and prediction of faults throughout estimation techniques. In this specific context, special interest is given to the development of robust techniques against resolver sensor failures (sensorless operation), because their incorrect performance involve catastrophic consequences. The near-future trend considers sensorless techniques for limp-home operation, i.e., to allow drivers reach their destination safely in a pseudo-optimal mode.

Taking into account the conclusions derived from review of the state of the art, the work carried out in this thesis presents two contributions. On the one hand, a reliable field weakening control strategy suitable for EV applications, which improves the overall control algorithm robustness under parameter deviations and uncertainties is presented in chapter 3. On the other, a novel hybrid sensorless strategy, which guarantees sufficient limp-home operation is presented in chapter 4.

Chapter 3

Look-up table based flux weakening strategy including novel voltage constraint tracking feedback

3.1 Introduction

In industrial applications, reliable regulation algorithms are required in order to control the torque production of an electric machine in the whole drive torque and speed operation range. According to the state of the art (chapter 2), the most common synchronous machine torque control approaches consist on regulating the machine stator currents in the synchronous dq reference frame [10, 11, 77, 107, 117, 188–194]. Among them, the PI based Field Oriented Control (FOC) is the preferred option in the industry [107]. This strategy must be complemented with an optimal current set-point generation algorithm to drive an EV propulsion system through the maximum efficiency points, including Field Weakening (FW) and deep FW operation when required.

In this context, a great amount of works dealing with FW control can be found in the scientific literature [10,77,107,167,188,191,195–199]. Some authors propose the usage of flowchart [77, 191] or PI based strategies [197–199]. In general, these FW algorithms only consider the i_d current modification [77, 190–192], which could be only valid for machines without deep FW operation requirements. For example, reference [200] proposes an optimized FW strategy, where either i_d^* or the phase angle of the reference current are the voltage loop control actions. The corresponding transfer function is defined, allowing the precise design and adjustment of the voltage control loop. The regulator is designed considering constant electrical parameters and DC-link voltage.

In order to provide deep FW operation, other approaches can be used. For example, an unified direct-flux vector control implemented in the stator flux reference frame is proposed in [168]. This method relies in the d-axis component of the stator voltage to control the stator flux, while torque is controlled throughout the q-axis component of the stator current. This strategy requires a stator flux estimator and an additional PI, which makes its implementation somehow complex. Similarly, analytic methods compute online the optimum current trajectories for the whole operation range of the machine [107], at the cost of increasing the computational burden [201–203]. These strategies can be combined with online parameter estimation algorithms [204, 205], providing additional robustness under parameter uncertainties. Nevertheless, the time required for estimation convergence prevents the usage of these approaches in EV applications with high dynamic response requirements.

In commercial EV drives it is of common practice to precalculate these set-points and store them in Look-up Tables (LUTs) [10, 11, 167, 188, 206, 207]. In this sense, figure 3.1 shows the general diagram of a torque control algorithm for synchronous machines including the current regulators and the optimal current set-point generation. Ideally, this last should be based on the knowledge of the reference electromagnetic torque (T_{em}^*), DC-link voltage (V_{DC}), machine mechanical speed (ω_{mech}) and rotor temperature ($T_{emp,rotor}$). Thus, machine electrical parameter identification is required in order to precisely precalculate these LUTs. FEM analysis [112, 208] or experimental procedures [112, 209] are commonly employed to obtain the electric machine d- and q-axis fluxes[1].

LUT based methods are preferred in the industry due to their low computational burden and simplicity. However, LUT approaches tune the control algorithm for an specific set of electrical parameters and may eventually loss control under parameter variations due to an incorrect FW regulation, i.e., exceeding the stator voltage limit and leading to an uncontrolled energy regeneration [169]. The high non-linearities caused by the magnetic saturation effect [112], together with electrical parameter variations due to machine ageing, manufacture toler-

---

[1] Permanent magnet flux and d- and q-axis inductances can be calculated from these fluxes following an appropriate procedure [112].

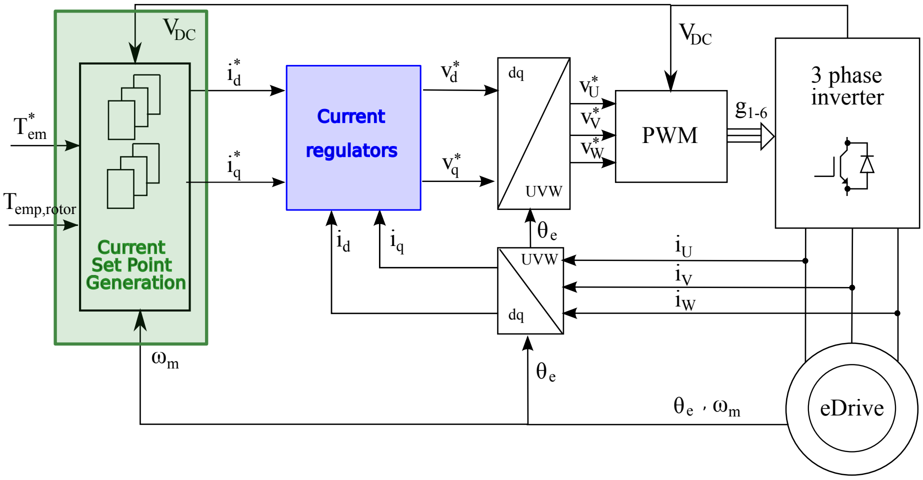

Figure 3.1: General diagram of a 4D-LUT based indirect torque control approach for synchronous machines.

ances and temperature dependency [210] confirm the importance of relying on a robust control strategy that ensures the correct operation of the EV drive during its whole life-cycle [211, 212].

In this chapter, a reliable FW control algorithm for EVs and/or HEVs mounting synchronous machines is proposed and fully validated. An IPMSM model is used for simulation validation, while the experimental validation is carried out with a 51 kW full scale automotive PM-assisted SynRM machine. An improvement of the LUT based control scheme, consisting of a robust hybrid 2D-LUT/voltage feedback based current set-point generator is proposed. The main advantage of the proposed algorithm is based on the fact that optimized LUT values are used unless parameter deviations jeopardize the stator voltage limit. The current set-point LUT data is calculated in order to minimize the copper losses at low speeds and magnetic losses at high speeds.

The chapter is organized as follows. Section 3.2 explains the operation regions of a synchronous machine, leading to the analytical solution for each of these regions. Sections 3.3 and 3.4 describe the LUT based algorithm precalculation and its dimensioning. Section 3.5 presents the proposed Voltage Constraint Tracking (VCT) flux weakening strategies. Sections 3.6 and 3.7 include simulation and experimental results that validate the proposed approach. Finally, conclusions are given in section 3.8.

3.2 Operation regions of synchronous machines

3.2.1 Voltage and current constraints

Synchronous machines exhibit torque and speed constraints due to inverter current rating and available DC-link voltage. These limitations must be taken into consideration [167] and can be expressed in terms of current and voltage as follows:

$$I \leq I_{max}, \tag{3.1}$$

$$V \leq V_{max}, \tag{3.2}$$

being I_{max} and V_{max} the maximum allowable stator current and voltage, respectively, and being I and V the instantaneous stator current and voltage vector modulus. From (3.1) and (3.2) and using the Clarke and Park transformations, the current and voltage limit curves in the dq reference frame (appendix A) can be rewritten as:

$$\sqrt{i_d^2 + i_q^2} \leq I_{max}, \tag{3.3}$$

$$\sqrt{v_d^2 + v_q^2} \leq V_{max}. \tag{3.4}$$

The voltage limit curve can be derived from the machine voltage equations in the dq coordinates. From (2.5) and (2.7), the dq voltage equations in steady-state ($di_{d,q}/dt = 0$) can be expressed as:

$$v_d = R_s i_d - \omega_e L_q(i_d, i_q) i_q, \tag{3.5}$$

$$v_q = R_s i_q + \omega_e L_d(i_d, i_q) i_d + \omega_e \Psi_{pm}(i_q). \tag{3.6}$$

In some cases, the stator resistance R_s can have a significant impact in the voltage limit and must be considered. However, the effect of R_s has been neglected in this particular application because its influence is low. Without considering the effect of R_s, (3.5) and (3.6) can be rewritten as:

$$v_d = -\omega_e L_q(i_d, i_q) i_q, \tag{3.7}$$
$$v_q = \omega_e L_d(i_d, i_q) i_d + \omega_e \Psi_{pm}. \tag{3.8}$$

Replacing (3.7) and (3.8) in (3.4), the voltage limit inequation (3.9) is obtained.

$$\sqrt{\left[\omega_e L_q(i_d, i_q) i_q\right]^2 + \left[\omega_e L_d(i_d, i_q) i_d + \omega_e \Psi_{pm}\right]^2} \leq V_{max}, \tag{3.9}$$

which can be rewritten as a speed dependant elliptical constraint:

$$L_d^2(i_d, i_q)\left[i_d + \frac{\Psi_{pm}}{L_d(i_d, i_q)}\right]^2 + L_q^2(i_d, i_q) i_q^2 \leq \left(\frac{V_{max}}{\omega_e}\right)^2. \tag{3.10}$$

The current limit curve (3.3) produces a circumference of radius I_{max} in the stator currents *dq* plane (figure 3.2). Similarly, (3.10) produces ellipses whose radius is reduced while the electrical machine speed increases (figure 3.2). Synchronous machines must be controlled such as the *dq* plane stator current vector lies simultaneously within the current constraint circumference and voltage constraint ellipse [167].

Taking these constraints into account, various optimal current trajectories can be obtained as a function of the mechanical speed and the reference torque. Figures 3.3 and 3.4 show optimal trajectory examples of the stator currents in the *dq* reference frame for $L_d = L_q$ (i.e. SM-PMSM) and for the general case, where $L_d \neq L_q$ (i.e. IPMSM or PM-assisted SynRM), respectively.

According to the previously defined current (3.3) and voltage (3.10) constraints, four operation regions can be distinguished for a synchronous machine (figure 3.5): Maximum Torque Per Ampere (MTPA) region, Field Weakening (FW) region (without and with torque production reduction) and Maximum Torque Per Voltage (MTPV) region. In the following, the analytical solutions of these optimal current trajectories are presented.

3.2.2 Maximum Torque Per Ampere region

An MTPA curve exists in the stator currents *dq* reference frame which ensures a maximum torque per applied current modulus (figure 3.5, region I). Minimum

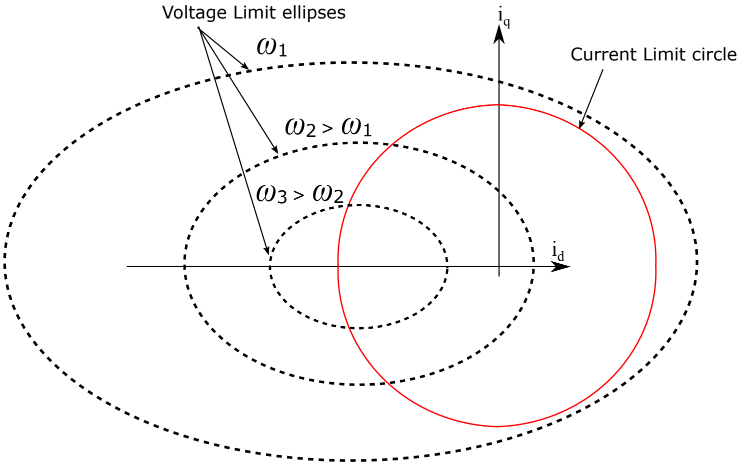

Figure 3.2: Current constraint circumferences and speed dependant voltage limit ellipses in the synchronous dq reference frame.

ohmic losses (predominant at low operation speed) are obtained if this curve is tracked.

In the particular case of SM-PMSM machines, where $L_d = L_q$, the MTPA trajectory (figure 3.3) is directly obtained from the torque equation (2.14). As i_d has no torque production capability, the i_d and i_q current pair that must be applied can be expressed as:

$$i_q = \frac{T_{em}}{\frac{3}{2}P\Psi_{pm}}, \tag{3.11}$$

$$i_d = 0. \tag{3.12}$$

For the general case where $L_d \neq L_q$, the MTPA curve corresponds to the following i_d and i_q current pair:

$$i_d = \frac{\Psi_{pm} \pm \sqrt{\Psi_{pm}^2 + 8I^2(L_d - L_q)^2}}{4(L_d - L_q)}, \tag{3.13}$$

$$i_q = \pm\sqrt{I^2 - i_q^2}, \tag{3.14}$$

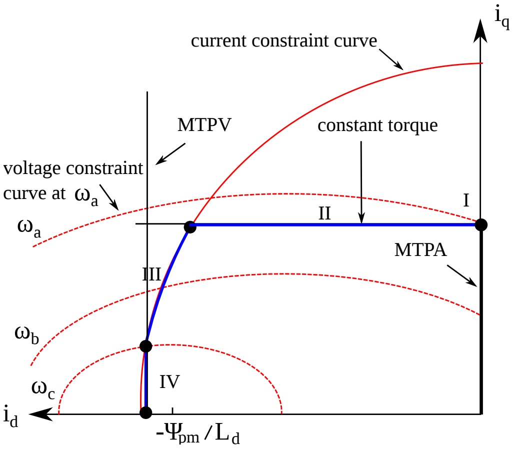

Figure 3.3: Optimum trajectory example of the stator currents in the dq plane for a SM-PMSM ($L_d = L_q$).

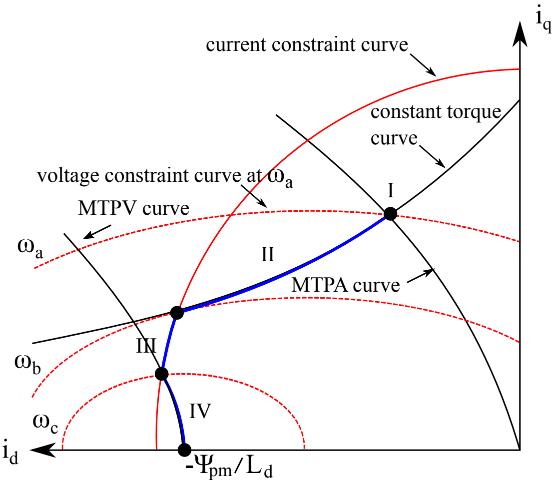

Figure 3.4: Optimum trajectory example of the stator currents in the dq plane for an IPMSM ($L_d \neq L_q$).

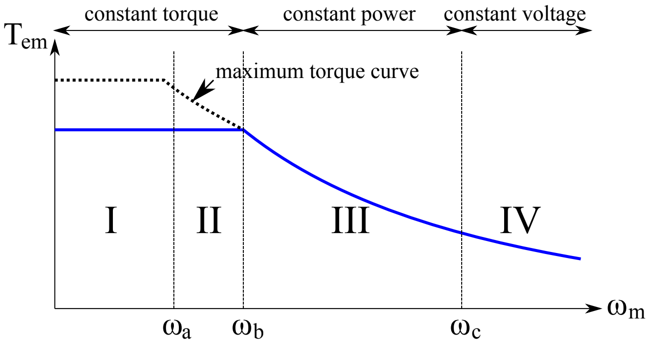

Figure 3.5: Optimum operation regions: MTPA (I), field weakening (II), field weakening with torque reduction (III) and MTPV (IV).

where $I = \sqrt{i_d^2 + i_q^2}$ is the current modulus. The solution of (3.13)-(3.14) relies on the resolution of a quartic polynomial, which is not straightforward.

It is possible to analytically calculate the MTPA solution for i_d^* and i_q^* from the desired torque set-point. The MTPA solution is formulated in [107] as a constrained minimization problem, where the function to be minimized is:

$$i_d^2 + i_q^2, \tag{3.15}$$

subject to the constraint

$$\frac{3}{2}P\left[\Psi_{pm}i_q + (L_d - L_q)i_d i_q\right] = T_{em}. \tag{3.16}$$

This problem can be solved using the Lagrangian approach, being the Lagrangian expression defined as [107]:

$$L(i_d, i_q, \lambda) = i_d^2 + i_q^2 + \lambda\{\frac{3}{2}P\left[\Psi_{pm}i_q + (L_d - L_q)i_d i_q\right] - T_{em}\}, \tag{3.17}$$

where λ is the Lagrangian multiplier. The conditions for minimizations are expressed as:

$$\frac{\partial L}{\partial i_d} = 0 \;\rightarrow\; 2i_d + \frac{3}{2}P\lambda(L_d - L_q)i_q = 0, \tag{3.18}$$

$$\frac{\partial L}{\partial i_q} = 0 \;\rightarrow\; 2i_q + \frac{3}{2}P\lambda\left[\Psi_{pm} + (L_d - L_q)i_d\right] = 0, \tag{3.19}$$

$$\frac{\partial L}{\partial \lambda} = 0 \;\rightarrow\; \frac{3}{2}P\left[\Psi_{pm} i_q + (L_d - L_q) i_d i_q\right] - T_{em} = 0. \tag{3.20}$$

Solving these equations for i_d, the following polynomic is obtained [107]:

$$i_d^4 + A_1 i_d^3 + B_1 i_d^2 + C_1 i_d + D_1 = 0, \tag{3.21}$$

where

$$A_1 = \frac{3\Psi_{pm}}{(L_d - L_q)}, \tag{3.22}$$

$$B_1 = \frac{3\Psi_{pm}^2}{(L_d - L_q)^2}, \tag{3.23}$$

$$C_1 = \frac{\Psi_{pm}^3}{(L_d - L_q)^3}, \tag{3.24}$$

and

$$D_1 = -\frac{16(T_{em}^*)^2}{9P^2(L_d - L_q)^2}. \tag{3.25}$$

Quartic polynomials are the highest order ones with an analytical solution. Ferrari's method can be used to solve (3.21). Selecting the right solution from the four possible ones, i_d^{MTPA} can be solved as [107]:

$$i_d^{MTPA} = -\frac{A_1}{4} - \frac{\eta_1}{2} - \frac{\mu_1}{2}, \tag{3.26}$$

where

$$\mu_1 = \sqrt{\frac{3}{4}A_1^2 - \eta_1^2 - 2B_1 - \frac{1}{4\eta_1}(4A_1B_1 - 8C_1 - A_1^3)}, \tag{3.27}$$

$$\eta_1 = \sqrt{\frac{A_1^2}{4} - B_1 + \gamma_1}, \tag{3.28}$$

$$\gamma_1 = \frac{B_1}{3} + \sqrt[3]{-\frac{\beta_1}{2} + \sqrt{\frac{\beta_1^2}{4} + \frac{\alpha_1^3}{27}}} + \sqrt[3]{-\frac{\beta_1}{2} - \sqrt{\frac{\beta_1^2}{4} + \frac{\alpha_1^3}{27}}}, \tag{3.29}$$

and

$$\alpha_1 = \frac{1}{3}(3A_1C_1 - 12D_1 - B_1^2), \tag{3.30}$$

$$\beta_1 = \frac{1}{27}(-2B_1^3 + 9A_1B_1C_1 + 72B_1D_1 - 27C_1^2 - 27A_1^2D_1). \tag{3.31}$$

Once i_d is determined for the MTPA solution, i_q^{MTPA} is calculated from (2.14).

3.2.3 Field Weakening region

In order to extend the speed operation region of a synchronous machine, the traditional control strategy consists of injecting negative i_d current, resulting in the so called FW control [213]. In this way, the current vector is maintained inside the voltage constraint ellipse.

In the region known as FW without torque reduction, this is achieved without losing torque capability (figure 3.5, region II). In the particular case of SM-PMSM (figure 3.3, region II), only i_d is reduced, while, in the general case (figure 3.4, region II) i_d is reduced and i_q is then recalculated to maintain the reference torque.

When the current constraint circumference is reached, the torque capability is limited in FW operation (figure 3.5, region III). In order to achieve maximum torque in this region, the current set-point vector must be positioned in the intersection between the voltage and current constraint curves.

For a given torque set-point, maximum available voltage and mechanical speed, it is possible to analytically determine the current set-points in FW operation [107], considering the following minimization problem:

$$\text{Minimize}: \; L_d^2 \left[i_d + \frac{\Psi_{pm}}{L_d} \right]^2 + L_q^2 i_q^2 \leq \left(\frac{V_{max}}{\omega_e} \right)^2, \tag{3.32}$$

subject to the constraint

$$\frac{3}{2} P[\Psi_{pm} i_q + (L_d - L_q) i_d i_q] = T_{em}. \tag{3.33}$$

The quartic polynomial for the FW solution is given by:

$$i_d^4 + A_2 i_d^3 + B_2 i_d^2 + C_2 i_d + D_2 = 0, \tag{3.34}$$

where

$$A_2 = \frac{2\Psi_{pm}}{(L_d - L_q)} \left[2 - \frac{L_q}{L_d} \right], \tag{3.35}$$

$$B_2 = \frac{\Psi_{pm}^2}{(L_d - L_q)^2} + \frac{4\Psi_{pm}^2}{L_d(L_d - L_q)} + \frac{\Psi_{pm}^2}{L_d^2} - \frac{V_{max}^2}{w_e^2 L_d^2}, \tag{3.36}$$

$$C_2 = \frac{2\Psi_{pm}}{L_d} \left[\frac{\Psi_{pm}^2}{(L_d - L_q)^2} + \frac{\Psi_{pm}^2}{L_d(L_d - L_q)} - \frac{V_{max}^2}{w_e^2 L_d (L_d - L_q)} \right], \tag{3.37}$$

$$D_2 = \frac{1}{(L_d - L_q)^2} \left[\frac{\Psi_{pm}^4}{L_d^2} + \frac{L_q^2}{L_d^2} \frac{4T_{em}^*}{9P^2} - \frac{V_{max}^2}{w_e}{}^2 \frac{\Psi_{pm}^2}{L_d^2} \right], \tag{3.38}$$

being V_{max} the maximum stator voltage magnitude.

The general solution is calculated similarly to the MTPA region:

$$i_d^{FW} = -\frac{A_2}{4} - \frac{\eta_2}{2} + \frac{\mu_2}{2}, \tag{3.39}$$

where η_2 and μ_2 are calculated from (3.27) and (3.28) using the new variables A_2, B_2, C_2 and D_2.

3.2.4 Maximum Torque Per Voltage region

In this operation region (also known as *deep field weakening region*), the torque production capability is maximized for a constant stator voltage value (figure 3.5, operation region IV). The MTPV region only exists for a particular machine if the $\Psi_{pm}/L_d \leq I_{max}$ condition is fulfilled.

In a SM-PMSM, the MTPV trajectory implies that i_d must be fixed to $-\Psi_{pm}/L_d$, while for the general case ($L_d \neq L_q$) the MTPV trajectory is [107]:

$$i_d^{MPTV} = \frac{\lambda_d - \Psi_{pm}}{L_d}, \tag{3.40}$$

$$i_q^{MPTV} = \frac{\sqrt{(V_s/w_e)^2 - \lambda_d^2}}{L_d}, \tag{3.41}$$

where

$$\lambda_d = \frac{-L_q\Psi_{pm} + \sqrt{L_q^2\Psi_{pm}^2 + 8(L_d - L_q)^2(V_s/w_e)^2}}{4(L_d - L_q)}. \tag{3.42}$$

3.3 LUT content calculation methods considering magnetic saturation

3.3.1 Introduction

The LUT content calculation can be straightforward when no magnetic saturation is present in the electric machine [214]. However, the effect of the magnetic saturation cannot be neglected in EV and HEV applications. In the following, two methods are presented in order to calculate the optimal current reference trajectories under magnetic saturation.

3.3.2 Iterative analytical LUT calculation

The influence of the magnetic saturation can be taken into account solving the equations of section 3.2 iteratively. Following this approach, machine inductances and permanent magnet flux values are updated for each iteration, and a convergence in the resulting current vector is obtained for all the operation points.

A flowchart diagram of the proposed iterative LUT calculation method is shown in figure 3.6. The operation principle of the implemented offline calculation algorithm is as follows:

1. The electrical parameters L_d, L_q and Ψ_{pm} are determined for a given pair of i_d^*, i_q^* currents (note that currents are set to 0 during the first iteration).

2. Taking into account the electrical parameters and a given reference torque, the current references for the MTPA region (i_d^{MTPA}, i_q^{MTPA}) are obtained throughout the analytic method described in section 3.2.2.

3. The flowchart checks whether the stator voltage V_s exceeds the maximum voltage available (V_{max}) or not. If the inverter voltage output is not saturated ($V_s < V_{max}$), the flowchart assumes that the drive is working in the MTPA region. Therefore, the calculated current references (i_d^{MTPA}, i_q^{MTPA}) will be applied to the flowchart for the following iteration.

4. If the inverter output voltage is saturated, FW and MTPV current trajectories are calculated simultaneously using the analytic expressions described in sections 3.2.3 and 3.2.4, respectively.

5. By comparing the values of i_d^{FW} and i_d^{MTPV}, the flowchart decides if the operation point corresponds to the MTPV region or the FW one, updating the current references for the next iteration.

Note that the implemented iterative procedure does not consider any current or power limitations of the propulsion system. Those limits can be included in the online torque control algorithm after the LUTs, improving the flexibility of the LUT data. Thanks to this, current and power limits can be easily tuned in the model, not requiring to recalculate the current trajectories.

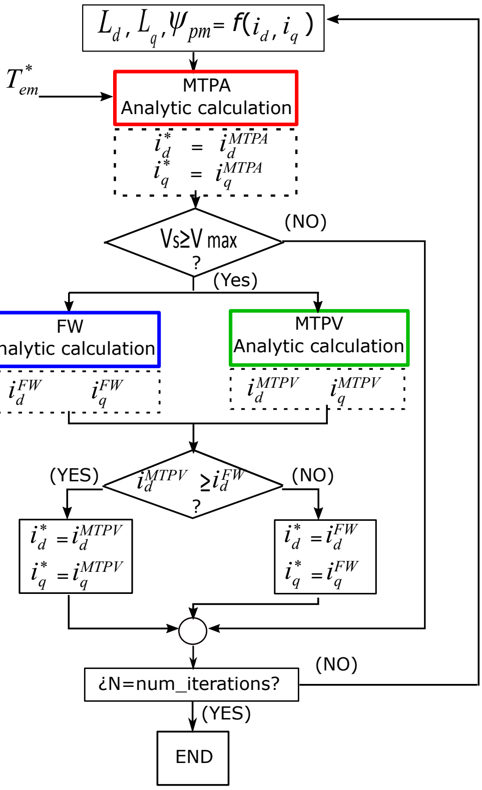

Figure 3.6: Proposed iterative flowchart for the offline current set-point LUT calculation under magnetic saturation.

3.3.3 LUT calculation using optimization methods

An alternative to the proposed iterative method consists of using optimization strategies. MATLAB tool *fmincon* aims to find the local minimum of a constrained non-linear multi-variable function. As an example, the required current references for the MTPA region using the MATLAB *fmincon* optimization strategy can be obtained as follows:

- Definition of the optimization function, which is evaluated for different

MTPA operation points:

$$[currents,\ fval] = \tag{3.43}$$

$$= fmincon(Cost, [..], [..], [..], [..], [..], [..], [..], Constr, options], \tag{3.44}$$

where *currents* is the optimum output value (in this particular case the output is a matrix $[i_d^*, i_q^*]$), $fval$ is the value of the objective function, *Cost* is the objective function to minimize (*cost function*), *Constr* defines the constraints and the optimization options are specified in *options*.

- Definition of the cost function *Cost* considering the MTPA region. The cost function aims to minimize the predominant losses in this operation region, i.e., copper losses (P_{CU}). Then, the cost function can be expressed as:

  $$P_{CU} = \frac{3}{2} R_s (i_d^2 + i_q^2). \tag{3.45}$$

- Definition of the minimization constraints. Two types of constraints can be distinguished. On the one hand, $c(x)$ represents the constraint where $c(x) \leq 0$ and, on the other, $ceq(x)$ represents the constraint $ceq(x) = 0$. The following constraints must be considered for this particular case:

  $$c(1) = i_d^* - i_{d,max}, \tag{3.46}$$

  $$c(2) = i_{d,min} - i_d^*, \tag{3.47}$$

  $$c(3) = i_q^* - i_{q,max}, \tag{3.48}$$

  $$c(4) = i_{q,min} - i_q^*, \tag{3.49}$$

  $$c(5) = V_s - V_{max}, \tag{3.50}$$

  $$ceq(1) = T_{em} - T_{em}^*, \tag{3.51}$$

  where $c(1)$, $c(2)$, $c(3)$ and $c(4)$ force the dq currents to be under their corresponding maximum limits, $c(5)$ ensures that the stator voltage remains under the maximum DC bus voltage and $ceq(1)$ tries to minimize the error between the estimated torque and the reference one.

In this work, the iterative method has been mainly used for LUT construction, although for some particular cases optimization methods have been employed.

3.4 LUT dimensioning optimization

The number of LUT dimensions has a direct impact in the amount of memory required by the microcontroller to store them. Thus, it is important to optimize the number of dimensions needed for a proper torque control of the machine. As explained in the introduction of this chapter, ideally 4D-LUTs could be required in order to precisely determine the current set-point of an EV drive in a given operation point. These dimensions are the reference torque (T_{em}^{*}), DC-link volt age (V_{DC}), mechanical speed (ω_{mech}) and rotor temperature ($T_{emp,rotor}$). In practice, the dimensions required by the current set-point generation LUTs can depend on the specific electric machine and application (for example, whether DC-link voltage varies or not), and also on the required torque production precision (rotor temperature dependency).

Rotor temperature can be obtained using telemetry systems or infrared sensors [215, 216], which avoids the usage of cables and brushes but requires additional hardware, or can be estimated from back-EMF observers [215, 216]. However, at low and zero speeds, such estimators tend to fail due to the lack of back-EMF. Thus, it is difficult to achieve a good rotor temperature estimation in the whole motor operation range. Due to the complexity and/or additional cost of the aforementioned solutions, rotor temperature consideration is not of common practice in industrial applications [216]. Generally, the deviations produced by temperature effects are accepted and no compensation action is performed.

As DC-link voltage varies in battery powered EV drives, this dimension must be considered in EV applications. However, the LUT dimension related to DC-link voltage variations can be eliminated using the speed normalization concept presented in [192].

From (3.10) and neglecting the effect of the stator resistance, the maximum stator voltage is obtained as:

$$V_{max} = \omega_e \sqrt{(L_d i_d + \Psi_{pm})^2 + (L_q i_q)^2}. \tag{3.52}$$

In a two-level three-phase Voltage Source Inverter (VSI) fed machine, the maximum achievable phase voltage for the linear modulation region when Space Vector modulation or PWM with third harmonic injection is adopted is:

$$V_{max} = \frac{V_{DC}}{\sqrt{3}}. \tag{3.53}$$

A normalized voltage (V_{DC}^{norm}), which can be the minimum or the nominal

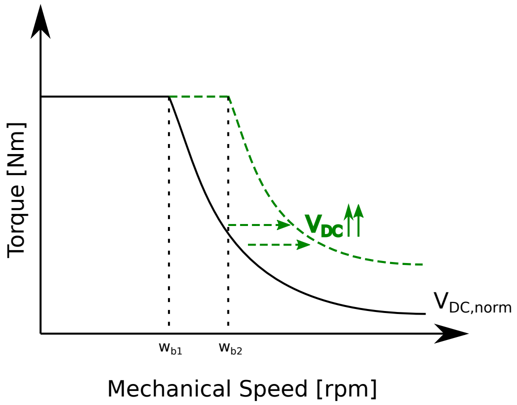

Figure 3.7: Speed normalization strategy.

DC-link voltage value, can be selected to define the μ normalization coefficient [192]:

$$\mu = \frac{V_{DC}}{V_{DC}^{norm}}. \tag{3.54}$$

Substituting (3.54) into (3.53), the following expression is obtained:

$$V_{max} = \frac{V_{DC}}{\sqrt{3}} = \frac{\mu V_{DC}^{norm}}{\sqrt{3}} = \mu V_{max}^{norm}, \tag{3.55}$$

while substituting (3.55) into (3.52), the following speed normalization equation is obtained:

$$\omega_e = \frac{\mu V_{max}^{norm}}{\sqrt{(L_d i_d + \Psi_{pm})^2 + (L_q i_q)^2}} = \mu \omega_e^{norm}. \tag{3.56}$$

From (3.56), when the DC-link voltage increases, ω_e^{norm} becomes smaller than the real electrical speed ω_e. This is equivalent to a displacement of the speed vs torque curve towards the right side (figure 3.7), expanding the voltage limit. The opposite occurs when the DC-link voltage decreases. Thus, the normalized speed can be calculated and used as an input for a 2D-LUT (with ω_{norm} and T_{em}^{*} as inputs) calculated for the normalization DC-link voltage (V_{DC}^{norm}) operation conditions.

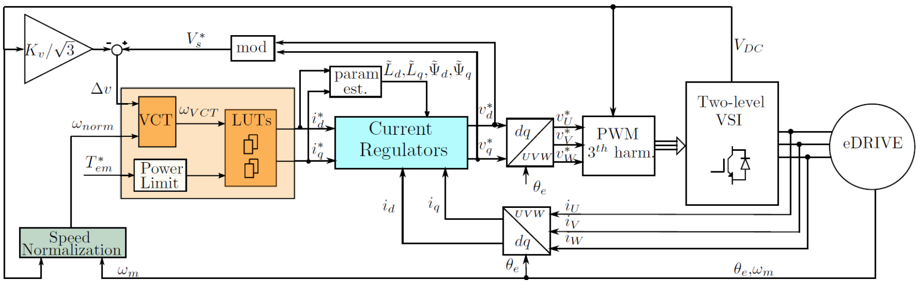

Figure 3.8: General diagram of the proposed current regulators with hybrid 2D-LUT/VCT based feedback control strategy.

Equation (3.56) can be also expressed in terms of mechanical speed (ω_m), obtaining the speed normalization equation used in the application:

$$\omega_m = \mu\omega_{norm}. \tag{3.57}$$

Advantages of this approach become clear, because the amount of memory needed for the implementation of the algorithm in a microprocessor is highly reduced, keeping the same precision as when a 3D-LUT is used.

3.5 Proposed 2D-LUT/VCT hybrid FW strategies

3.5.1 Introduction

From sections 3.2.2, 3.2.3 and 3.2.4, it becomes clear that the calculations to obtain i_d^* and i_q^* for a given operation point depend on the machine electrical parameters. From (3.10), it can be derived that variations in the d- and q-axis inductances modify the voltage limit ellipse (figure 3.4), leading to possible controllability problems in FW and MTPV operation [169]. The high non-linearities caused by the magnetic saturation [112] together with electrical parameter variations due to machine ageing, manufacture tolerances and temperature dependencies are responsible for such parameter deviations.

In this thesis, a 2D-LUT based FW control strategy including a novel Voltage Constraint Tracking (VCT) feedback is proposed (figure 3.8). The LUTs

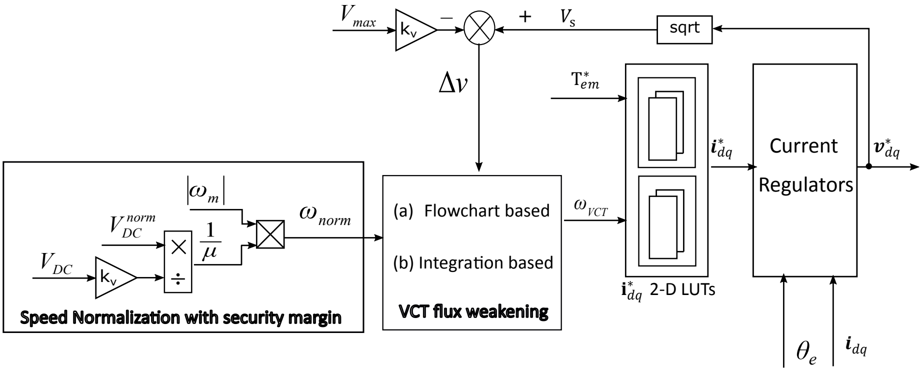

Figure 3.9: LUT based current reference determination using the speed normalization concept and proposed flowchart and integration based VCT feedback strategies.

dimension optimization is achieved thanks to the speed normalization concept described in the previous section. The normalized speed ω_{norm} is controlled using a VCT regulator (figure 3.9), which aims to maintain the stator voltage vector close to the voltage limit margin in the FW and MTPV regions, according to the error produced between the current control reference voltage V_s^* and the voltage limit V_{max}:

$$\Delta v = V_s^* - K_v V_{max} = \sqrt{(v_d^*)^2 + (v_q^*)^2} - K_v \frac{V_{DC}}{\sqrt{3}}, \tag{3.58}$$

where K_v provides a security margin ($K_v < 1$) in order to ensure that the voltage limit is never reached. In this sense, two solutions for the VCT regulation have been proposed, as shown in figure 3.10:

- Flowchart based normalized speed control.
- Integration based normalized speed control.

The main advantages of these methods are that no machine parameters are needed in their calculations and that they provide additional robustness to the LUT method under parameter variations. In the following, both VCT alternatives are described in detail, and the selection of the most appropriate strategy that will be implemented in the experimental platform is carried out considering their features and performance in a Matlab/Simulink based simulation platform.

3.5.2 Flowchart based VCT regulator

The proposed flowchart based VCT strategy follows the diagram shown in figure 3.10. This strategy is based on the solution proposed in [191]. At the beginning, the algorithm checks whether V_s is higher or lower than the voltage limit, i.e., it checks the sign of Δv. If $\Delta v \geq 0$, the variable *status* is set to 0 to indicate that VCT strategy should be activated.

If *status* $= 1$, the voltage limit is not reached so no VCT strategy is activated; thus, the output speed remains invariable. When entering in FW (*status* $= 0$), the flowchart is divided into two branches, by checking again the sign of Δv. If $\Delta v \geq 0$, branch "A" will be selected. Otherwise, branch "B" will be activated.

In branch "A", the normalized speed needs to be increased in order to force the system into a deeper FW operation and keep the stator voltage inside the voltage limit (figure 3.11):

$$\omega_{VCT}(k) = \omega_{VCT}(k-1) + \alpha|\Delta v|, \tag{3.59}$$

where α is a positive parameter.

On the other hand, when branch "B" is activated, the normalized speed should be reduced in order to follow the voltage constraint:

$$\omega_{VCT}(k) = \omega_{VCT}(k-1) - \beta|\Delta v|, \tag{3.60}$$

being β a positive parameter.

Both α and β parameters should be manually adjusted for each particular application. The decision of whether the VCT strategy needs to continue activated or not is processed in branch "B". If the calculated normalized speed $\omega_{VCT}(k)$ is smaller than the reference normalized speed $\omega_{norm}(k)$, the flowchart assumes that VCT operation should be stopped. Therefore, *status* signal is set to 1 and the flowchart re-starts its algorithm, analysing the polarity of Δv.

In summary, the proposed algorithm decides whether to modify or keep the commanded normalized speed. When the FW is activated, branch "A" and "B" modify the commanded normalized speed, in order to maintain the voltage vector close to the DC-link voltage limit.

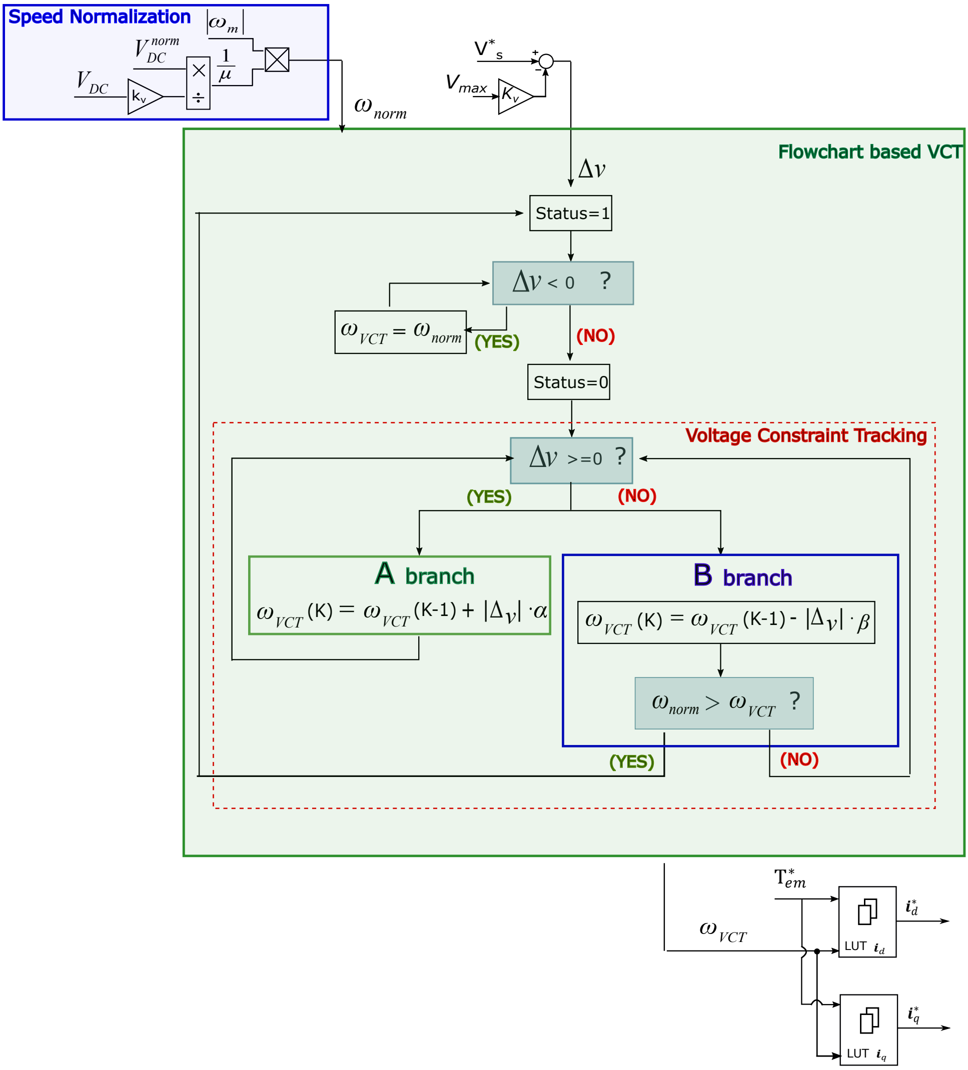

Figure 3.10: Flowchart based VCT for normalized speed command determination.

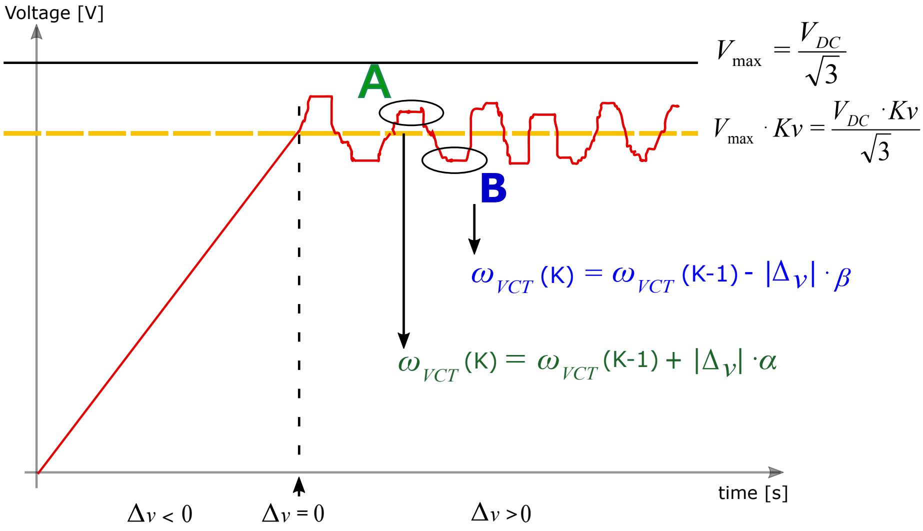

Figure 3.11: Operation mode of the flowchart based VCT.

This strategy needs to set α and β. Normally α must be high enough to ensure a quick return of the voltage vector inside the voltage limit curve, and β must be adjusted in a way to guarantee a correct reference speed determination during VCT regulation.

3.5.3 Integration based VCT regulator

In figure 3.12, a diagram of the proposed integration based VCT feedback is shown. This strategy also aims to correct the commanded normalized speed, ensuring that the inverter output voltage remains under the voltage limit in both FW and MTPV regions.

The integration based voltage closed loop algorithm in the k instant is defined by:

$$\omega_{VCT}(k) = \omega_{norm}(k) + \delta\omega(k), \tag{3.61}$$

being

$$\delta\omega(k) = \delta\omega(k-1) + \alpha\Delta v, \tag{3.62}$$

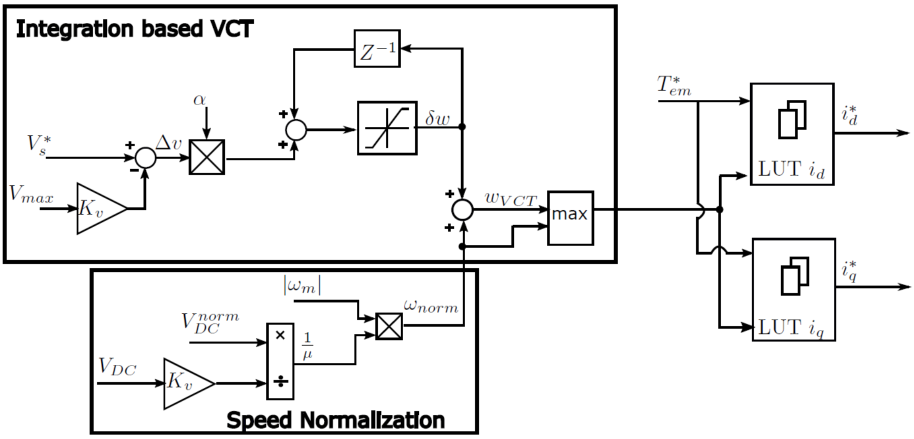

Figure 3.12: Diagram of the hybrid LUT/VCT current set-point generator with the integration based VCT feedback control.

where α is a positive constant and $\delta\omega(k)$ is a correction term, saturated as follows:

$$\delta\omega(k) = \begin{cases} 0 & if\ \delta\omega(k) \leq 0, \\ \delta\omega(k) & if\ \delta\omega(k) > 0. \end{cases} \tag{3.63}$$

When the inverter output voltage exceeds the maximum voltage limit including the security margin ($\Delta v > 0$), the term $\delta\omega(k)$ becomes positive, increasing the value of $\omega_{VCT}(k)$ until the voltage error Δv becomes zero. Therefore, the dq current set-points are simultaneously modified (the reference current vector is maintained within the voltage ellipse constraint) in order to keep the stator voltage controlled. In contrast, when the inverter output voltage is not saturated ($\Delta v \leq 0$), the correction term $\delta\omega(k)$ is negative. Taking into account the saturation effect defined in (3.63), the corrector term does not affect the normalized speed, and $\omega_{VCT}(k) = \omega_{norm}(k)$.

The main advantage of both proposed methods relies on the fact that they only modify the theoretically or experimentally predefined optimum set-points when it is required, maintaining the LUT values when deviations are sufficiently small to ensure machine controllability.

In terms of parameters adjustment, the integration based approach only re-

Table 3.1: Most significant nominal parameters of the simulated IPMSM machine.

Parameter	**Symbol**	**Value**	**Units**
Maximum power	P_N	100	kW
Maximum speed	w_{max}	3500	rpm
Stator Resistance	R_s	0.04	Ω
d-axis nominal inductance	L_d	1	mH
q-axis nominal inductance	L_q	1.7	mH
Permanent Magnet Flux linkage	Ψ_{PM}	0.178	Wb

quires to tune an additional control parameter (α). In contrast, two parameters are required (α and β) for the flowchart based VCT regulator. The added computational burden of this strategy is lower than the flowchart based regulator.

3.6 Simulation results

In order to compare and validate throughout simulation the proposed control strategies, a 100 kW automotive IPMSM including magnetic saturation has been simulated in the Matlab/Simulink environment. The torque control algorithm, including the VCT regulator and the LUTs, is executed every 90 μs. The Variable DQ (VDQ) approach [116] has been followed for IPMSM modelling, and LUTs have been calculated based on the IPMSM magnetic model (section 3.3.2). Table 3.1 shows the most significant nominal parameters of the simulated IPMSM. This machine presents typical saturation profiles of a medium-power IPMSM automotive propulsion electric machine (figure 3.13). Regarding the current control algorithm, a conventional PI based FOC has been integrated in order to carry out the following simulations.

In order to validate the controllability of the IPMSM in FW using the proposed VCT strategies, the following parameter deviations have been set: $\delta\Psi_{pm} = +10\%$ and $\delta L_d = +10\%$.

Figure 3.14 shows the simulation results of the proposed control approaches. When VCT control is not active in the loop, the voltage limit is exceeded and the system becomes unstable due to the electrical parameter variations (figure 3.14(a)). However, an effective VCT control is achieved when using both proposed strategies (figure 3.14(a)). The current vector trajectory in the dq plane and its correspondence to the operation modes is shown in figure 3.15. A

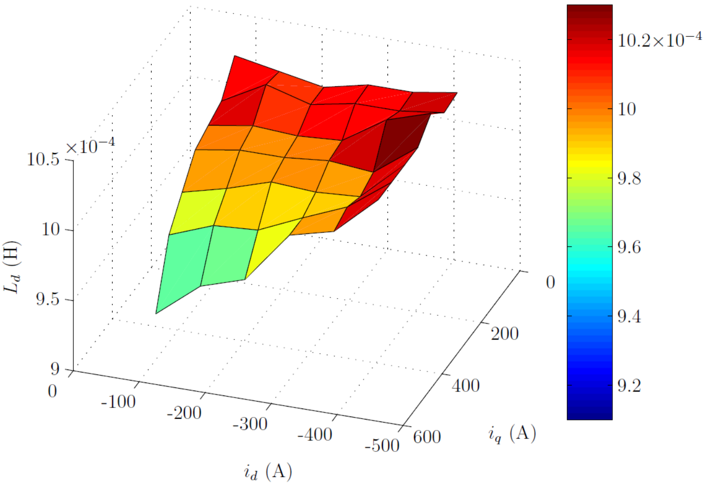

(a) d-axis inductance of the IPMSM.

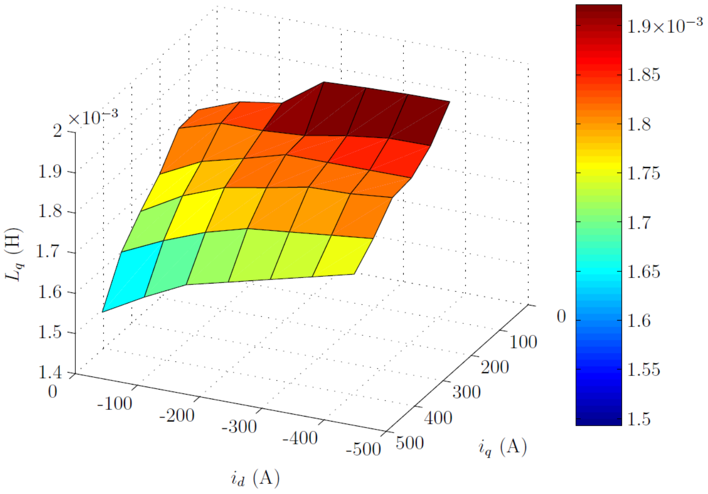

(b) q-axis inductance of the IPMSM.

Figure 3.13: Simulated IPMSM d- and q-axis inductances considering magnetic saturation.

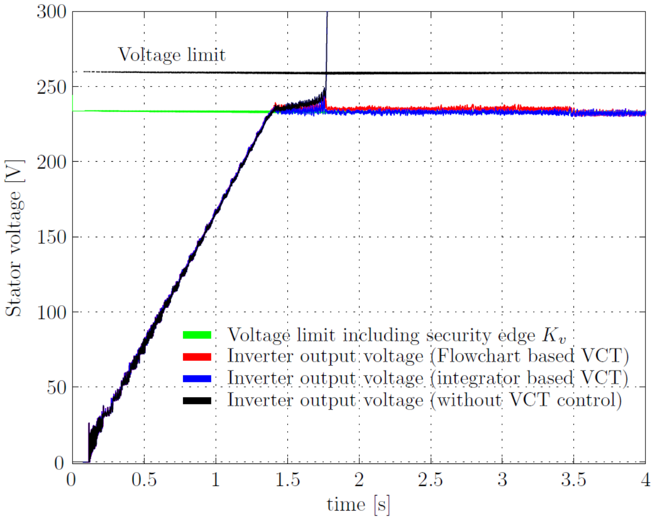

(a) VCT voltage control results of the proposed LUT based feedback control strategies.

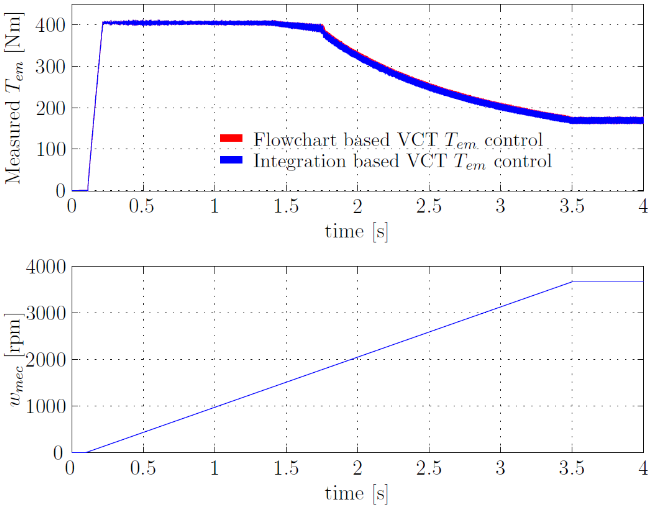

(b) VCT torque control results of the proposed LUT based feedback control strategies.

Figure 3.14: Proposed VCT based IPMSM control strategies (simulation results).

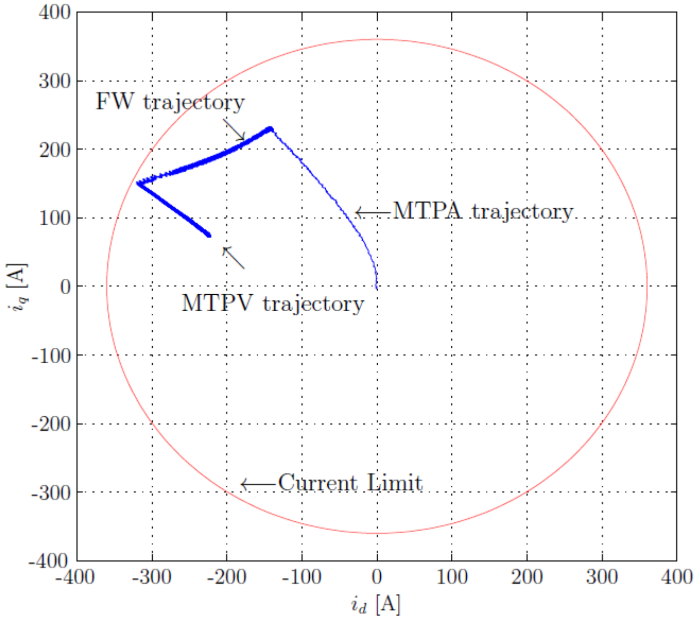

Figure 3.15: Simulated IPMSM dq plane current vector trajectory (using the integration based VCT algorithm) and its correspondence to each operation mode.

proper FW control is achieved through the whole drive operation range despite the introduced parameter variation (figure 3.14(b)).

In order to adjust the VCT regulation parameters (α, β for the flowchart based and α for the integration based VCT), simulations have been carried out considering ±10% errors in the electrical parameters. The parameters adjustment has been carried out following a trial and error method.

In the case of the flowchart based VCT strategy (figure 3.16), both α and β must be adjusted to correctly control the system in FW operation with the VCT. As it can be seen from figure 3.16(a), α parameters must be adjusted high enough to guarantee that the system remains under the maximum voltage limit. Similarly, from figure 3.16(b) it is deduced that β adjustment must ensure a correct speed return when the VCT algorithm is not required. In this particular

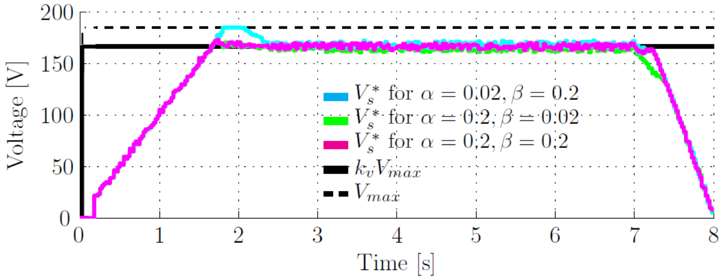

(a) Stator voltage V_s control for various values of α, β.

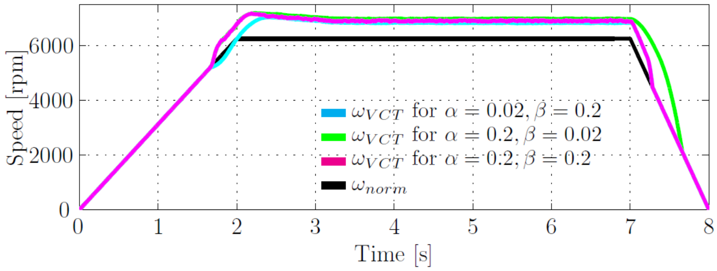

(b) w_{norm} vs w_{VCT} for various values of α,β.

Figure 3.16: Simulation results carried out for the control parameter adjustment (α, β) of the flowchart based VCT strategy.

application, α and β values have been set as $\alpha = \beta = 0.2$. However, they are not strictly required to be the same.

When using the integration based VCT strategy (figure 3.17), the system losses control if no VCT regulation is achieved ($\alpha = 0$), driving V_s^* into saturation. Taking into account the EV drive dynamics and according to simulation, a value of α between 0.01 and 0.1 has been considered.

Finally, in order to analyse and compare the system's performance using the proposed strategies, performance indices have been adopted [217], being the system optimum when the index reaches a minimum value. The performance index used is the Integral of the Square of the Error (ISE), defined as:

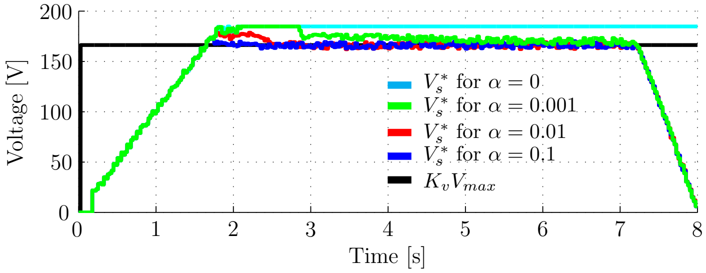

(a) Stator voltage V_s control for various values of α.

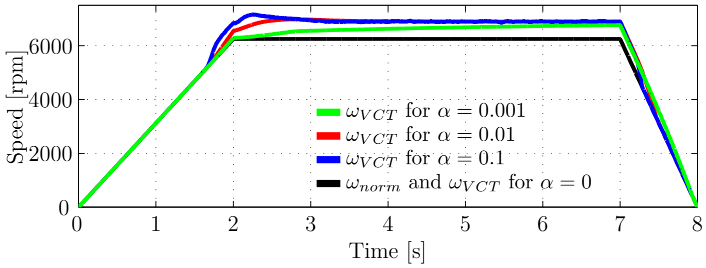

(b) w_{norm} vs w_{VCT} for various values of α.

Figure 3.17: Simulation results carried out for the control parameters adjustment (α) of the integration based VCT strategy.

$$ISE = \int_0^T e^2(t)dt. \tag{3.64}$$

where $e(t)$ is the instantaneous difference between the commanded and the actual stator voltage.

Figure 3.18 shows the results obtained using both flowchart and integrator based VCT control techniques, assuming various parameter deviation levels. In the three conditions tested, the integrator based VCT technique minimizes the ISE index.

Taking into account the results provided by the ISE performance index analysis and considering the simplicity and the low computational cost requirement of the application, the integration based VCT strategy has been considered for its usage in the experimental platform.

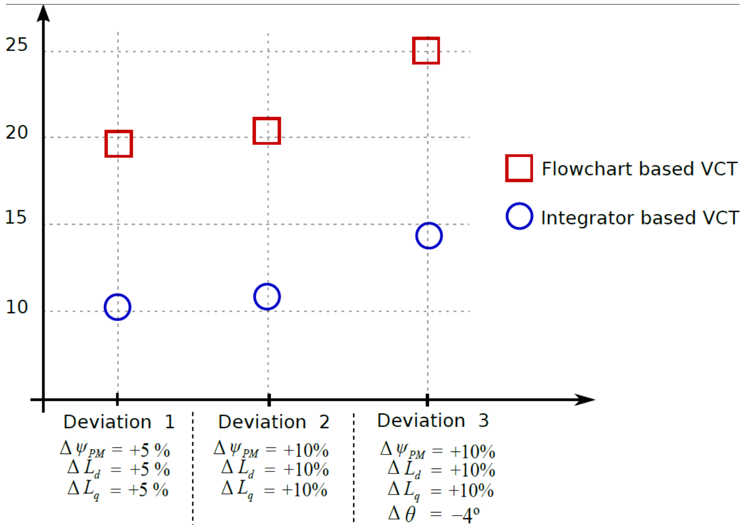

Figure 3.18: Comparison of the VCT based alternatives using the ISE performance index.

3.7 Experimental results

The proposed 2D-LUT/VCT feedback based current set-point generation strategy has been validated in a 51 kW automotive PM-Assisted SynRM, whose most significant parameters are listed in table 3.2. The d- and q-axis inductances and magnetic fluxes obtained throughout Finite Element Model (FEM) analysis are shown in figures 3.19 and 3.20. The details of the test bench used to carry out the experimental results are included in appendix C. Taking into account the nature of this machine, the effects of magnetic saturation and cross coupling in the machine's electrical behaviour have an important impact and cannot be neglected.

The switching frequency of the converter has been set to 10 kHz. A dead-time compensation algorithm [218] has been carried out in order to minimize its effect. The optimal current set-point LUTs have been precalculated using the FEM data of the machine and the calculation approach described in section 3.3. As for the torque controller, the conventional FOC control strategy has been replaced by a SMC control (section 2) because of the high non-linearities of the

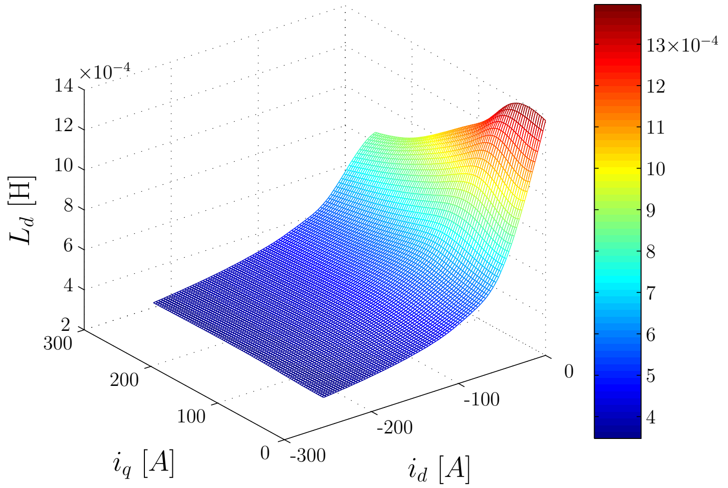

(a) Inductance L_d

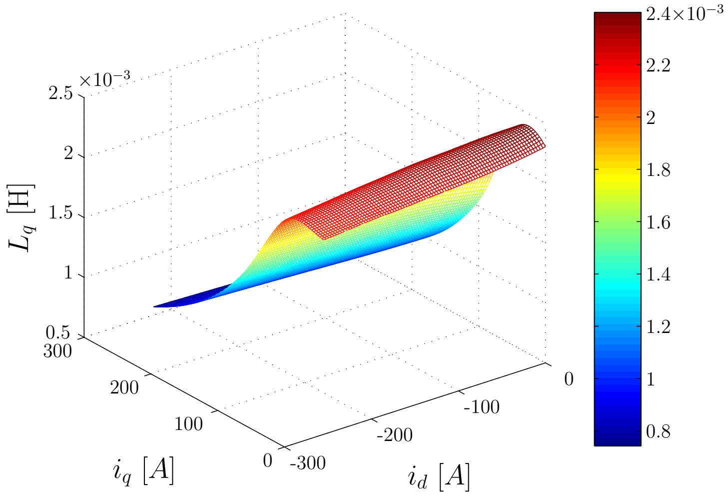

(b) Inductance L_q

Figure 3.19: PM-Assisted SynRM d- and q-axis inductances according to the provided FEM analysis.

Table 3.2: Nominal parameters of the PM-Assisted SynRM.

Item	**Symbol**	**Value**	**Units**
Nominal power	P_N	51	kW
Maximum speed	w_{max}	12000	rpm
Machine Pole Pairs	P	3	-
Stator Resistance	R_s	1.74	mΩ
d-axis nominal inductance	L_d	0.7	mH
q-axis nominal inductance	L_q	1.7	mH
Permanent Magnet Flux linkage	Ψ_{pm}	0.38	Wb
Stator nominal current	I_{nom}	255	A
DC-link nominal voltage	$V_{DC,nom}$	320	V

Table 3.3: SMC parameter settings.

Target control dynamics		
Item	**Symbol**	**Value**
Damping coefficient	ξ	1
Settling time	T_s	10 ms
$c_{d,q}$ selection and STA parameters		
Item	**Symbol**	**Value**
Sliding function parameters	$c_{d,q}$	580
STA parameter Ω	$\Omega_{d,q}$	$1.682e^5$
STA parameter λ	$\lambda_{d,q}$	$2.8532e^3$
VCT parameters		
Item	**Symbol**	**Value**
DC-link voltage security margin	k_v	0.9
VCT positive constant	α	0.01

electrical parameters, and also because of the SMC robustness against parameter variations, which can be significant in automotive drives. The control dynamic requirements and the SMC parameters used for this application are listed in Table 3.3.

Figures 3.21 and 3.22 show the results of the proposed SMC control strategy when conventional LUT based and hybrid 2D-LUT/VCT approaches are used for current set-point determination, at machine maximum torque (130 Nm). The

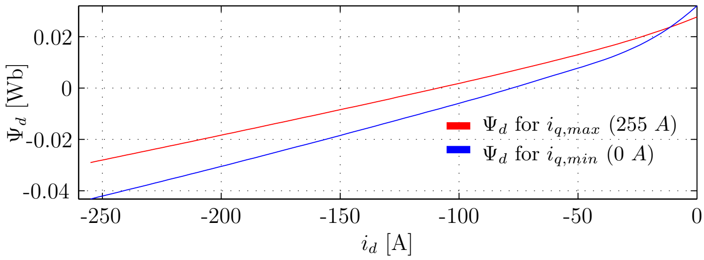

(a) Flux Ψ_d for minimum and maximum q-axis currents

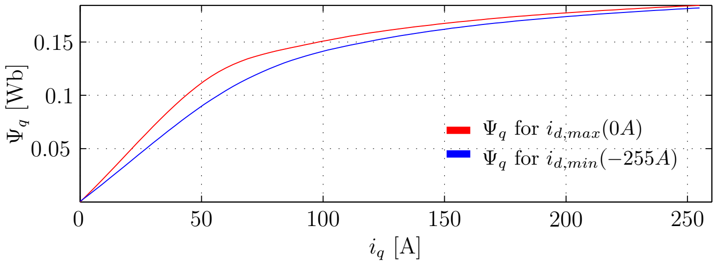

(b) Flux Ψ_q for minimum and maximum d-axis currents

Figure 3.20: PM-Assisted SynRM d- and q-axis fluxes according to the provided FEM analysis.

SMC current regulation is satisfactory, producing a low torque ripple (figure 3.22)[2]. If the VCT feedback is not included (figure 3.21), the stator voltage surpasses the voltage limit for a given mechanical speed, and the system is driven into an uncontrolled regeneration. This means that the maximum speed of the vehicle would be significantly reduced in a real EV application. In this particular case, the maximum machine speed of 12000 rpm corresponds to a maximum vehicle speed of 120 km/h. Taking into account that the control gets lost at around 4000 rpm, the vehicle maximum speed would be limited to 40 km/h, which would be unacceptable for the end-user. This issue is due to the fact that there are significant differences between the FEM data and the experimental machine, mainly due to the following reasons:

---

[2] As in real EV applications, electromagnetic torque has been indirectly measured from the stator currents.

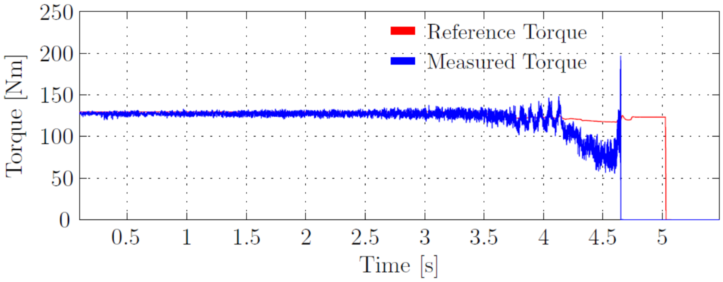

(a) Torque Control without VCT.

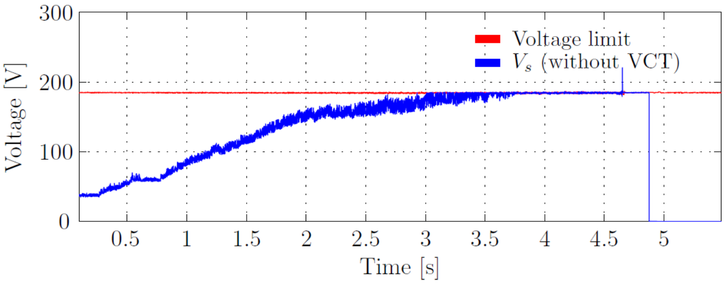

(b) Stator Voltage Control without VCT.

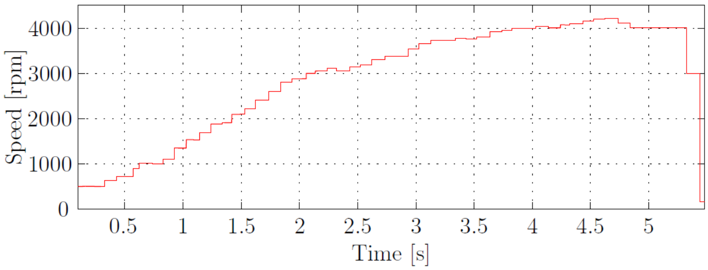

(c) Mechanical Speed.

Figure 3.21: SMC torque control, stator voltage V_s control and mechanical speed results without the VCT control strategy.

- No rotor temperature measurement is available. FEM analysis has been carried out for a particular set of stator winding and magnets temperatures. Therefore, the LUTs do not take into consideration the parameter variations produced by the temperature.

- Small deviations between the specified and the real airgap (due to manufacturing and mounting tolerances) highly affect the electrical parameters of the machine. This aspect is aggravated in PM-assisted SynRM machines, due to the sensitivity of ferrite magnets to this particular parameter.

- A 2.5D FEM model has been considered and, as a consequence, no information about the stray inductances of the winding heads can be obtained from the simulations. These stray inductances increase the resulting phase inductances, obtaining higher terminal voltages than expected.

However, system robustness is guaranteed when the hybrid LUT control strategy is included (figures 3.22(a), 3.22(b) and 3.22(c)). A robust torque and FW control performance is achieved in the whole operating range (figure 3.23) using the second order SMC control strategy combined with the proposed optimal current set-point generation. Current references are properly modified by the VCT algorithm (figure 3.23(b)), while torque production capability is reduced once the current limit is reached (figures 3.23(a) and 3.23(b)), and also during MTPV, in order to ensure the required voltage regulation. As it can be seen in figure 3.23(c), smooth transitions between the different operation regions is achieved. The corresponding current vector trajectory throughout the different operation regions in the dq plane is shown in figure 3.24.

The difference between the torque set-point and the actual torque (measured using a torquimeter) reveals the aforementioned mismatch between the real electrical parameters and the ones predicted by FEM analysis, as deviations of around 15 Nm have been confirmed at constant torque region and for maximum torque set-point.

Figure 3.25 shows the torque regulation for transients (in this case, torque changes from motoring to regenerative braking). Being an EV propulsion system, torque reference transients are ramped in order to improve the comfort of the passengers. Both the SMC regulators and the hybrid set-point generator prove to be robust in the occurrence of such torque transients. The SMC control equivalent voltages $v_{d,eq}$ and $v_{q,eq}$ are required to obtain a satisfactory transient response.

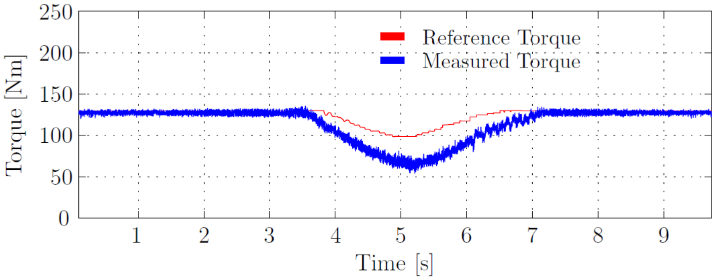

(a) Torque Control with VCT.

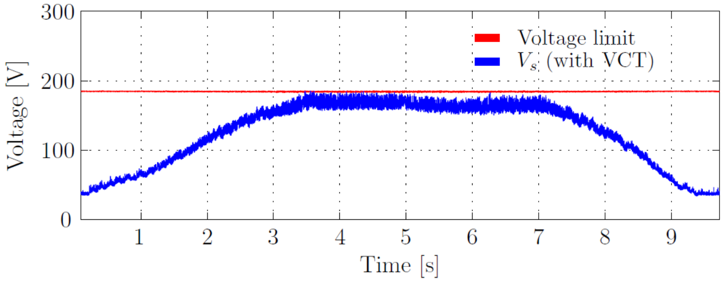

(b) Stator Voltage Control with VCT.

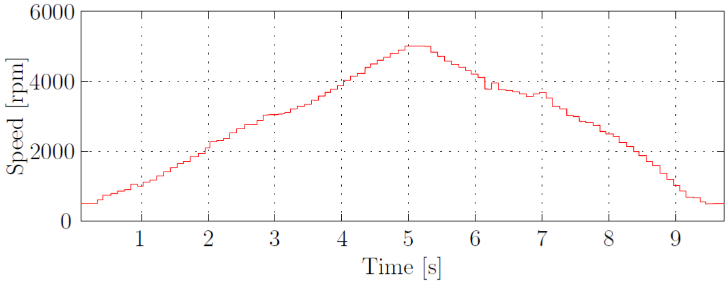

(c) Mechanical Speed.

Figure 3.22: SMC torque control, stator voltage V_s control and mechanical speed results with the VCT control strategy.

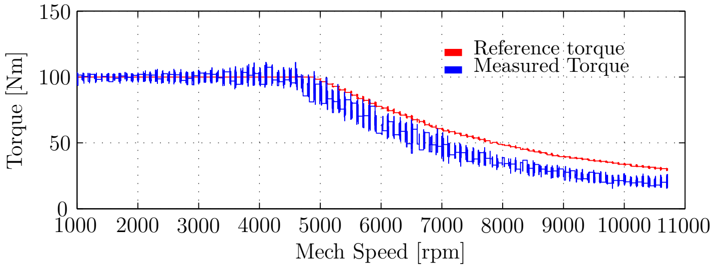

(a) Torque Control

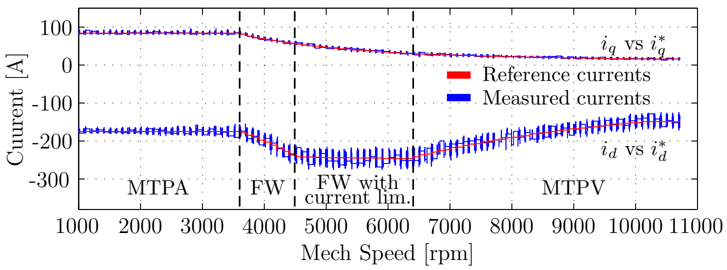

(b) Current Control

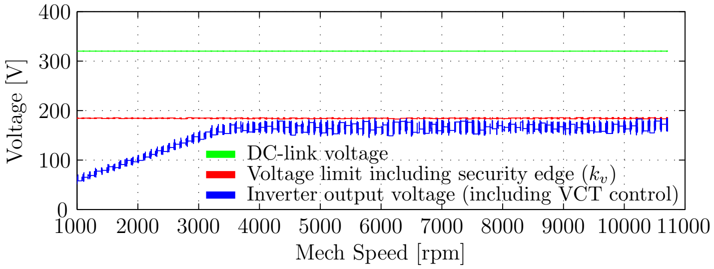

(c) Stator Voltage Control

Figure 3.23: Torque, current and stator voltage regulation experimental results using the proposed hybrid LUT/VCT based FW strategy.

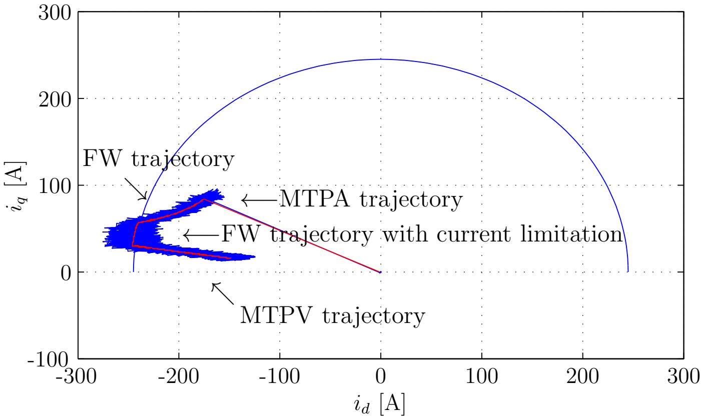

Figure 3.24: Current trajectories in the dq axis (current vector reference in red; measured current vector in blue).

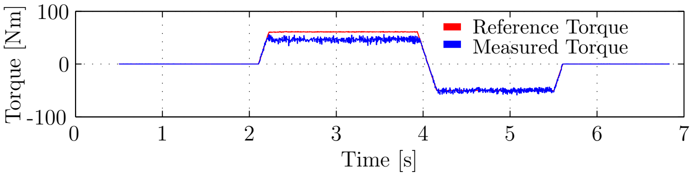

(a) Torque Control

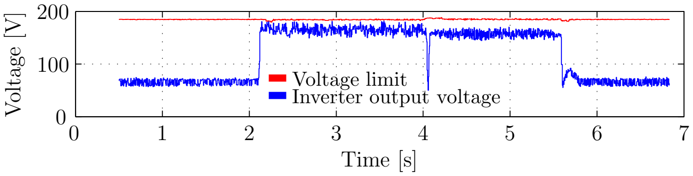

(b) Stator Voltage Control using VCT

Figure 3.25: Torque control stability using the VCT strategy when changing from motor driving to reverse braking at constant speed of 7000 rpm.

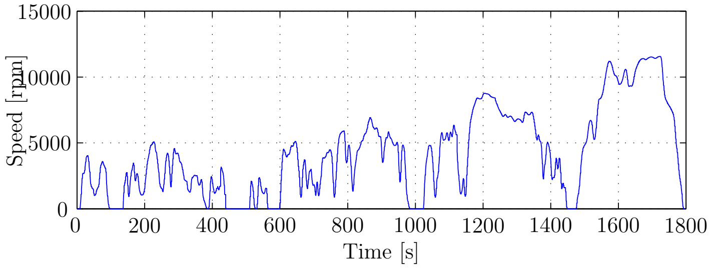

(a) Mechanical Speed

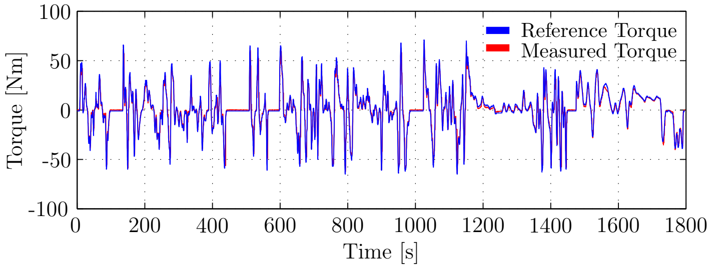

(b) Torque

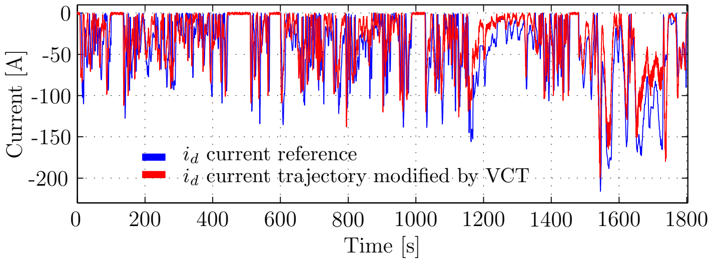

(c) VCT influence in d-axis current

Figure 3.26: Worldwide harmonized Light vehicles Test Procedure (WLTP) results.

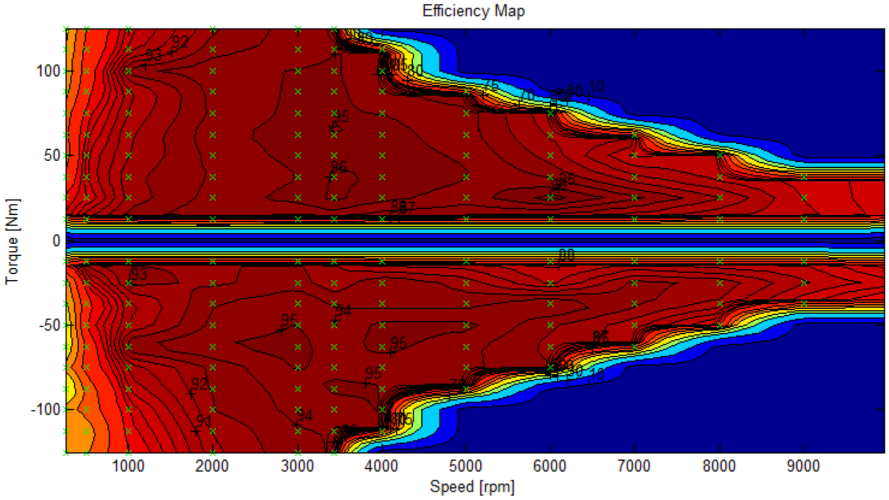

Figure 3.27: PM-assisted SynRM efficiency map in the whole operation range.

In order to evaluate the drive performance under real driving conditions, a standard Worldwide harmonized Light vehicles Test Procedure (WLTP) has been carried out. Driving cycles aim to analyze a vehicle's performance in terms of consumption, pollution and efficiency, among other factors. The WLTP is an specific driving cycle supposed to represent light duty vehicle operation and its accuracy ensures more realistic results than conventional driving cycles [219]. The last speed profile and torque response in both urban and extra urban cycles are shown in figure 3.26, including the torque response of the SynRM machine, which satisfactorily follows the reference requested by the driving cycle. Figure 3.26(c) shows how the VCT feedback acts modifying the d-axis current set-point when required. These results corroborate that the proposed strategy is ready to be implemented in real EVs and/or HEVs.

Finally, the efficiency map of the evaluated PM-assisted SynRM controlled with the proposed approach is shown in figure 3.27. The machine efficiency peak is above 95 % in a vast region around 4000 rpm, and above 90 % between 1000 rpm to 8000 rpm.

3.8 Conclusions

In this chapter, a FW control strategy that combines second order SMC current regulators with an optimal hybrid 2D-LUT/VCT based current set-point generation algorithm has been proposed, ensuring a satisfactory torque regulation in the whole machine operation range under parameter variations. Two VCT regulators have been developed and validated in simulation: the flowchart based and integration based VCT regulators. As it has been demonstrated by simulation, both solutions ensure controllability in the whole operation range, being activated only when the voltage constraint limit is reached. Additionally, a smooth tracking of the voltage limit is guaranteed. The main advantage of the aforementioned strategies is that no machine parameters are needed in their calculations. However, analysing the required control parameters (the flowchart strategy requires to adjust 2 parameters, against 1 parameter required by the integration based method) and considering computational burden, only the integration based VCT has been experimentally tested.

Experimental tests have been carried out in a state of the art test bench which emulates the EV and/or HEV real application, validating the proposed VCT approach, both under speed and torque variations and also under emulated real driving cycles conditions. Finally, it is important to point out that the proposed strategy can be easily extended to other synchronous machine types, such as pure SynRMs and PMSMs.

Chapter 4

Hybrid sensorless control solution for limp-home operation of automotive synchronous machines

4.1 Introduction

As stated in the state of the art (chapter 2), the safety and reliability requirements in EV applications have encouraged the research of fault tolerant strategies. Besides, the requirements of the international standard for functional safety ISO 26262 have also motivated the development of fail secure drives. In this sense, the Failure Mode and Effect Analysis (FMEA) is an established quality method in the automotive industry, which is proposed by the ISO 26262 [220–222]. One of the most critical failures detected by FMEAs in the context of an EV drive system is the resolver (or encoder)[1] sensor fault during driving, as it is essential for rotor flux angle determination.

Resolver fault tolerant strategies are conceived to operate in a derated mode, i.e., enabling the passengers to reach their destination despite the occurrence of a fault. This degraded operation mode is also known as limp-home sensorless

---

[1] In the following, this work will focus on resolver faults, although the proposal has the same validity for electric machines mounting encoders.

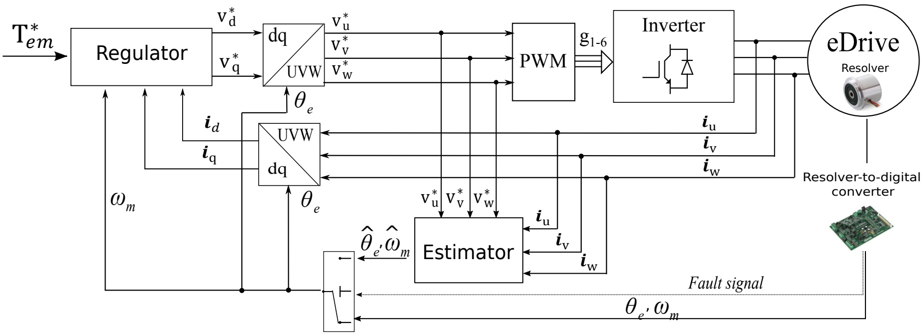

Figure 4.1: General diagram of an EV sensorless control strategy, including fault detection and control reconfiguration.

control. During this situation, a sensorless torque control is activated in order to maintain the system under control. As a first step, the identification of a position sensor fault is required. Automotive resolver-to-digital converters, such as the Analog Devices AD2S1210 or Tamagawa AU6803, to name a few, provide fault detection functions that detect abnormal resolver operation. Once the resolver fault is detected, an angle estimation technique based on the knowledge of the electric magnitudes of the machine (voltages and currents) must be conducted, making the development of a limp-home sensorless control possible (figure 4.1).

In this context, a great amount of observer based sensorless approaches have been reported in the scientific literature. The Extended Kalman Filter (EKF) is one of the most established technique for rotor angle estimation [223–225], being it suitable for non linear and noisy systems [223, 226]. However, the complex tuning of the covariance matrices of the EKF equations [70, 223, 227, 228], together with the high computational burden required during the state space estimation process [227, 229] are the major drawbacks of this method. Other sensorless techniques use deterministic strategies, such as Extended Luenberger Observer (ELO) based strategies [230, 231]. Sliding Mode Observers (SMO) are also another common alternative for rotor position estimation [232, 233]. The main advantage of SMO techniques is their robustness and low sensitivity to machine parameter variations. However, their limited sampling rate produces chattering problems, requiring additional robust strategies to overcome rotor position estimation errors [234, 235]. Other popular methods are based on Model Reference Adaptive Systems (MRAS), where estimation is carried out by comparing a reference and an adjustable model [23,231]. Besides, advanced strategies based on artificial intelligence, such as neural networks or fuzzy logic have been also recently studied [236–238].

The selection of the most suitable sensorless technique would depend on the requirements of the particular application. In an EV scenario, the limited microcontroller CPU computational capability[2], together with the increasing need of executing a great number of additional functions and the high sampling frequency required by the torque control algorithm[3], makes desirable to rely on simple sensorless algorithms with a low computational cost [22]. In this context, Phase Locked Loop (PLL) based estimators can be considered appropriate for automotive applications due to their ease of implementation [235,239,240].

In the EV context, it is required to operate in a wide speed range, including low speeds and standstill. At low speeds, the back-EMF magnitude is not high enough, making estimation inaccurate [241–243]. In industrial applications, this problem is generally solved using an open-loop strategy at start-up (I/f or V/f) [244,245]. However, it becomes clear that these alternatives cannot be considered for an EV propulsion system. For this reason, these techniques must be complemented with other approaches at low speeds, such as magnetic saliency based angle detection methods [241,242,246–248]. These techniques, also known as injection methods, introduce probe signals into the machine terminals, and they can be divided into two main categories:

- Strategies based on the modification of the PWM pattern, including a voltage test pulse, or applying specific switching states during the measurement period [79–81,249–252].

- Tecnhiques based on the High Frequency Injection (HFI) of voltage vectors in the static $\alpha\beta$ frame, or in the rotating dq synchronous reference frame, in order to obtain information about the rotor position [79–81,253–256].

A certain level of saliency between the d- and q-axes is required in the machine for their correct operation. In general, these techniques are not able to distinguish between the north and south poles of the magnet; thus, they must be complemented with other algorithms at their starting.

---

[2] Some of the most established automotive compliant microcontrollers are the Freescale MPC5643L (120 MHz), MPC5675K (180 MHz), MPC5744P (200 MHz) and the Texas Instruments TMS570 (180 MHz).

[3] Common electric machine control sampling frequencies are between 10 kHz and 20 kHz when using conventional Si devices.

The successful application of HFI based techniques has been reported for SynRMs [226,257] and for IPMSMs [246,258,259], being also possible to extend their usage to SM-PMSMs by exploiting the saliency resulting from the magnetic saturation produced by the magnets flux in the d-axis [246,247]. As a drawback, these techniques introduce additional power losses due to the injection of HF components, and their use should be limited as much as possible.

A number of sensorless algorithms that combine back-EMF estimators with injection based strategies have been proposed in the scientific literature [234, 259]. The usage of two sensorless algorithms operating at different speed ranges requires a transition method to guarantee a correct and smooth sensorless operation. Several changeover techniques rely on weighting coefficients to perform the transition [80,247,259–262]. Other methods propose the application of weighted averages of the estimated quantities during a given speed interval [228].

Taking all the latter into account, a novel hybrid sensorless control algorithm that provides limp-home operation for automotive synchronous machines is proposed in this thesis. This strategy combines a HFI technique with a PLL based back-EMF estimator. In order to minimize additional power losses, the HFI is disabled when the machine is driven at medium/high speeds. This contribution provides smooth transitions, determining the angle polarity to the HFI algorithm when a PLL-to-HFI transition is carried out. Additionally, speed reversal capability is provided to the PLL based estimator. Finally, the proposed strategy is successfully combined with the proposed hybrid 2-D LUT/VCT field weakening approach (chapter 3), and is validated throughout simulation and experimental tests in an automotive platform.

This chapter is organized as follows. The proposed hybrid sensorless structure is described in Section 4.2. Sections 4.3 and 4.4 include simulation and experimental results that validate the proposal. Finally, conclusions are given in section 4.5.

4.2 Proposed hybrid sensorless strategy

In this section, the main blocks that constitute the proposed sensorless approach, i.e., the PLL based back-EMF estimator, the HFI technique and the overall control structure and smooth transition strategy are described.

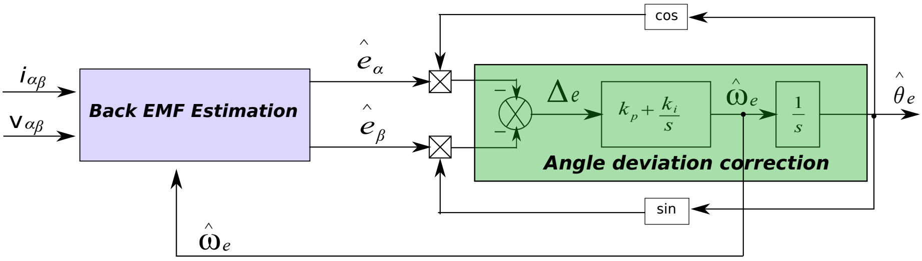

Figure 4.2: PLL based rotor position estimation diagram.

4.2.1 Phase Locked Loop based back-EMF estimator

Traditionally, PLLs have been used for the synchronization of power converters with the grid [263–265]. However, it is also possible to effectively use PLL structures for rotor position and speed estimation of synchronous machines, making it possible the implementation of PLL based sensorless control algorithms [235].

The PLL structure used in this work is shown in figure 4.2. Its operation principle consists of two main tasks: (i) the back-EMF estimation in the $\alpha\beta$ reference frame and (ii) the PLL based estimated angle deviation corrector.

Neglecting the magnetic saturation effect, the stator voltage equations in the $\alpha\beta$ reference frame can be expressed as:

$$v_\alpha = R_s i_\alpha + \frac{d\Psi_\alpha}{dt}, \tag{4.1}$$

$$v_\beta = R_s i_\beta + \frac{d\Psi_\beta}{dt}, \tag{4.2}$$

where v_α and v_β are the stator voltages, i_α and i_β are the stator currents, R_s is the stator resistance and Ψ_α and Ψ_β are the stator magnetic fluxes, which can be mathematically represented as:

$$\Psi_\alpha = L_s i_\alpha + \Psi_{pm} cos(\theta_e), \tag{4.3}$$

$$\Psi_\beta = L_s i_\beta + \Psi_{pm} sin(\theta_e), \tag{4.4}$$

being L_s the stator inductance and θ_e the rotor electrical angle. For simplicity, the stator inductance has been considered constant in this work[4].

---

[4] Particularly, in this work the simplification $L_s = (Ld + Lq)/2$ has been considered for salient synchronous machines.

Substituting (4.3) and (4.4) into (4.1) and (4.2), the stator voltage equations can be rewritten as follows:

$$v_\alpha = R_s i_\alpha + L_s \frac{di_\alpha}{dt} - \omega_e \Psi_{pm} sin(\theta_e), \tag{4.5}$$

$$v_\beta = R_s i_\beta + L_s \frac{di_\beta}{dt} + \omega_e \Psi_{pm} cos(\theta_e), \tag{4.6}$$

where the back-EMF voltage components in the $\alpha\beta$ reference frame are:

$$e_\alpha = -\omega_e \Psi_{pm} sin(\theta_e), \tag{4.7}$$

$$e_\beta = \omega_e \Psi_{pm} cos(\theta_e). \tag{4.8}$$

Substituting (4.7) and (4.8) into (4.5) and (4.6), the estimated back-EMF components can be represented as a function of the stator voltages and currents in the $\alpha\beta$ reference frame:

$$\widehat{e}_\alpha = v_\alpha - R_s i_\alpha - L_s \frac{di_\alpha}{dt}, \tag{4.9}$$

$$\widehat{e}_\beta = v_\beta - R_s i_\beta - L_s \frac{di_\beta}{dt}. \tag{4.10}$$

On the other hand, the sinusoidal stator currents in the $\alpha\beta$ reference frame can be represented as:

$$i_\alpha = I cos(\omega_e t + \phi), \tag{4.11}$$

$$i_\beta = I sin(\omega_e t + \phi), \tag{4.12}$$

where I is the rotating current vector amplitude and ϕ is the phase lag. Calculating the time derivatives of the currents, the following expressions are obtained:

$$\frac{di_\alpha}{dt} = -I\omega_e sin(\omega_e t + \phi) = -\omega_e i_\beta, \tag{4.13}$$

$$\frac{di_\beta}{dt} = I\omega_e cos(\omega_e t + \phi) = \omega_e i_\alpha. \tag{4.14}$$

Introducing (4.13) and (4.14) in (4.9) and (4.10), the outputs of the back-EMF estimator block shown in figure 4.2 are obtained:

$$\widehat{e}_\alpha = v_\alpha - R_s i_\alpha + L_s \widehat{\omega}_e i_\beta, \tag{4.15}$$

$$\widehat{e}_\beta = v_\beta - R_s i_\beta - L_s \widehat{\omega}_e i_\alpha. \tag{4.16}$$

Note that the estimated speed $\widehat{\omega}_e$ is required, as a feedback, in order to perform the back-EMF estimation (figure 4.2).

Considering that the PLL estimator block (figure 4.2) estimates the rotor position $\widehat{\theta}_e$ close to the real one, the following expression can be assumed:

$$\widehat{\theta}_e = \theta_e + \Delta_e, \tag{4.17}$$

where Δ_e is the error between the estimated and the real rotor electrical angle.

Operating the back-EMF components of (4.7) and (4.8), calculated in the structure of figure 4.2, and applying common trigonometric relations, the following result is obtained:

$$-\widehat{e}_\alpha cos(\theta_e) - \widehat{e}_\beta sin(\theta_e) = \widehat{\omega}_e \Psi_{pm} sin(\Delta_e). \tag{4.18}$$

Assuming the estimation error Δ_e very small, (4.18) can be linearised as:

$$\widehat{w}_e \Psi_{pm} sin(\Delta_e) \simeq \widehat{\omega}_e \Psi_{pm} \Delta_e. \tag{4.19}$$

Thus, following the structure of figure 4.2, the PLL based strategy regulates Δ_e to zero, making $\widehat{\theta}_e$ converge to θ_e.

It is important to remark that conventional PLL structures have a well known issue, as they fail when the rotation direction changes due to the following reasons [240]:

- The PI regulator K_p and K_i gains calculated for positive speed operation are not valid for negative speeds. Thus, these gains must be adapted accordingly.
- An offset of 180^o is obtained in the estimated angle when the machine speed is negative.

These limitations are overcome in this work during transitions, reconfiguring the PLL structure, as it will be explained in section 4.2.3.

4.2.2 High Frequency Injection technique

The HFI strategy used in this work introduces a HF voltage test signal into the stator terminals in order to obtain the information required for the determination of the electrical angle at low speeds and standstill. In this sense, the general sensorless torque control diagram, including the HFI technique, is shown in figure 4.3. The introduced HF voltage test signal produces additional HF components in the stator currents. An adequate measured current post processing procedure allows to determine the rotor position. It is important to point out that, in an EV, the usage of this technique does not interfere in its mechanical operation, as the machine is not be able to follow the HF torque produced by the injected test signal.

In this context, the HF perturbation is added to the $\alpha\beta$ reference voltages produced by the current regulation loop, and can be expressed as follows [246] (figure 4.3, HFI vector block):

$$\mathbf{v}_i = \begin{bmatrix} v_\alpha \\ v_\beta \end{bmatrix} = V_i \begin{bmatrix} -sin(\omega_i t) \\ cos(\omega_i t) \end{bmatrix}, \tag{4.20}$$

were V_i is the amplitude of the introduced HF voltage and w_i is the high frequency rotation speed.

Due to the saliency of the machine and thanks to the HFI, the measured currents contain information of the rotor position at the generated high frequency current components:

$$\mathbf{i}_i = \begin{bmatrix} i_{\alpha,i} \\ i_{\beta,i} \end{bmatrix} = \begin{bmatrix} I_0 cos(\omega_i t) + I_1 cos(2\theta_e - \omega_i t) \\ I_0 sin(\omega_i t) + I_1 sin(2\theta_e - \omega_i t) \end{bmatrix}, \tag{4.21}$$

where I_0 and I_1 correspond to amplitudes of the positive and negative rotating sequence components of the HF stator currents, respectively.

As it can be seen from (4.21), only the negative sequence component contains rotor position information. Thus, the measured currents need to be correctly processed in order to extract this angle. In this sense, the following four post-processing steps must be carried out (figure 4.4):

1. As a first step, a Band Pass Filter (BPF) must be added in order to remove the fundamental component.

2. After that, a coordinate rotation transforms the HF current into a rotating frame synchronous to the injected HF voltage vector.

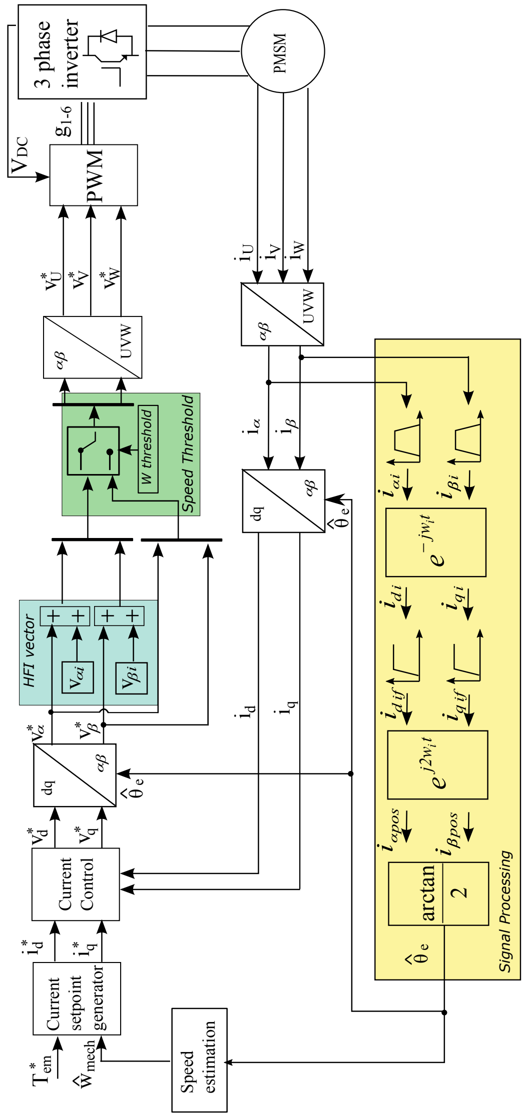

Figure 4.3: General diagram of a HFI sensorless control strategy, including HF voltage vector injection and measured current post-processing blocks.

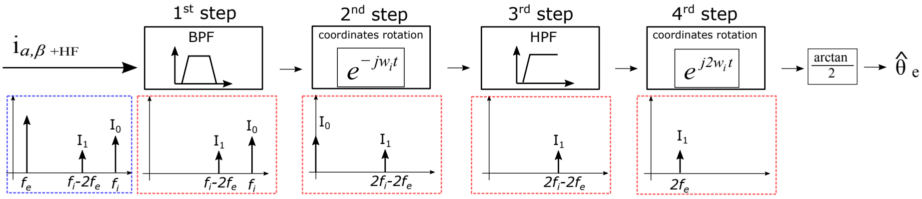

Figure 4.4: HFI sensorless strategy current processing.

3. A High Pass Filter (HPF) is included in order to remove the components produced by the previous rotation transformation.
4. A back rotation to the synchronous frame with the negative sequence obtains the following current components containing the position information:

$$\begin{bmatrix} i_\alpha \\ i_\beta \end{bmatrix} = I_{HF} \begin{bmatrix} cos(2\theta_e) \\ sin(2\theta_e) \end{bmatrix}. \tag{4.22}$$

From (4.22), the obtained angle $2\theta_e$ needs to be restored to θ_e, ensuring that the determined angle considers the correct PM polarity. Otherwise, the estimated angle could be π rad off from the actual rotor angle, leading to a possible catastrophic event. This is mandatory, because this technique cannot distinguish between the north and south poles of the rotor magnetic field.

In order to properly adjust the HFI based sensorless controller, three important requirements must be considered:

1. The frequency of the injected rotating voltage perturbation component must be determined. Commonly, this frequency is set around 10 times higher than the electrical machine fundamental frequency and 10 times lower than the power converter switching frequency [266]. For example, a value of $f_i = \omega_i/2\pi = 1$ kHz is typically used for power converters with a switching frequency of around 10 kHz [246, 247].
2. The injected voltage amplitude V_i is generally selected throughout an empirical process, taking into account that an excessively low voltage amplitude will not produce enough HF current to conduct a correct angle determination, and that current fluctuations and additional power losses will be greater when increasing the value of V_i [266].

3. A speed threshold ω_{th} to determine the transition point between the HFI and the PLL based estimator needs to be empirically adjusted (figure 4.3, speed threshold block). This threshold must be the lowest value that ensures that there is enough back-EMF for the PLL to correctly estimate the rotor position. In this way, the injection of HF perturbations is minimized.

Note that the usage of a BPF and a HPF in the current post-processing stage produces delays that must be compensated. These delays can introduce significant offsets in the estimated angle, reducing the drive efficiency and torque production capability. Additionally, these deviations, if great enough, can complicate the smooth transition between the HFI and the back-EMF estimation based algorithms.

4.2.3 Smooth transition procedure of the proposed sensorless algorithm

The general diagram of the proposed hybrid sensorless control algorithm, focusing on the transition between the HFI technique and the PLL based back-EMF estimator, is shown in figure 4.5.

The proposed transition procedure from medium to low speeds (and vice versa) is illustrated in figure 4.6. The PLL estimates the angular position above the speed threshold $|\omega 1|$, while the HFI is deactivated. When the machine reduces its speed and the operation speed is between $|\omega 1|$ and $|\omega 2|$, the angle obtained from the PLL is still used by the controller, while the HFI technique is activated to start converging. An hysteresis band between $|\omega 1|$ and $|\omega 3|$ is included to effectively change from the angle provided by the PLL to the one provided by the HFI, avoiding multiple changes around these speeds. The opposite procedure is carried out when accelerating. As stated before, these speed thresholds are selected considering a compromise between the existence of a sufficient back-EMF for the PLL based estimator and the minimization of the additional power losses produced by the HFI.

The first issue that must overcome the proposed transition structure is the speed reversal limitation of the PLL (section 4.2.1). The proposed structure schedules the PI regulator coefficients as a function of the sign of the estimated speed. Additionally, an offset of π is added to the estimated angle during speed reversal. The PLL reconfiguration (figure 4.5) is performed without adding any disturbance to the system, as it is performed at low speeds (positive or negative),

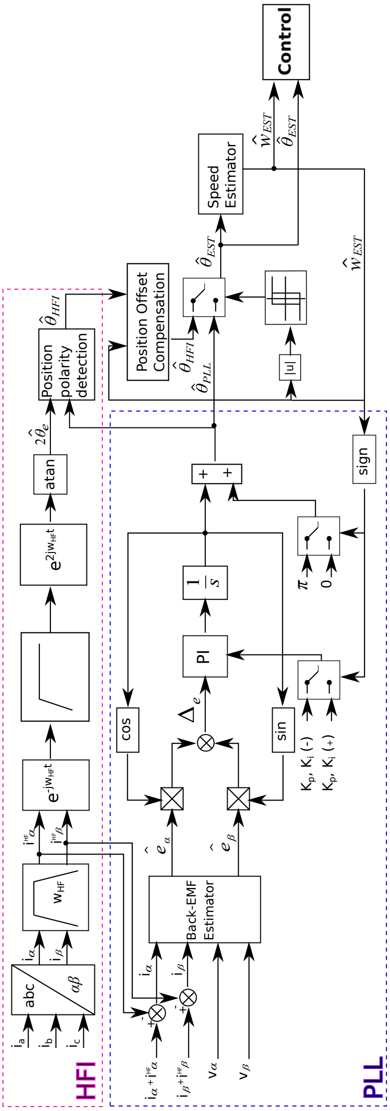

Figure 4.5: Hybrid angle estimation block diagram with the transition strategy between the PLL and HFI.

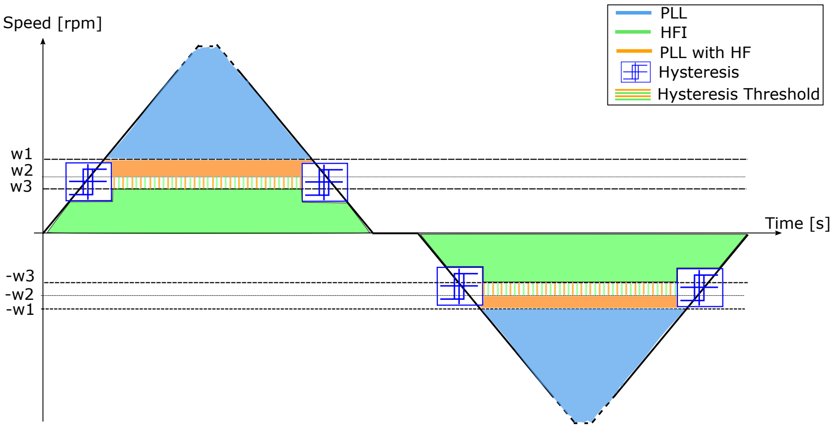

Figure 4.6: Hybrid sensorless control strategy along wide speed range and including transitions.

while the HFI technique is active and the angle estimated by the PLL is not being considered by the controller.

On the other hand and taking into account that HFI is restricted to low speed operation and standstill, the angle polarity must be checked each time the HFI algorithm is reactivated to properly restore θ_e from $2\theta_e$ (section 4.2.2). The proposed position polarity determination strategy is based on the information obtained from the PLL based back-EMF estimator (figure 4.5, position polarity detection block). The algorithm determines the polarity from the angle estimated by the PLL (figure 4.7):

$$Offset = \begin{cases} 0 & \text{if} \ \ \widehat{\theta}_e = \frac{\pi}{2} \pm HystBand, \\ \pi & \text{if} \ \ \widehat{\theta}_e = \frac{3\pi}{2} \pm HystBand, \end{cases} \tag{4.23}$$

where $HystBand$ is an hysteresis band included due to the following reasons:

(a) This band is included in order to avoid errors in the polarity determination due to possible angle offsets between both estimators.

(b) The polarity detection block must be robust enough against angle estimation errors produced due to errors due to noisy measured currents.

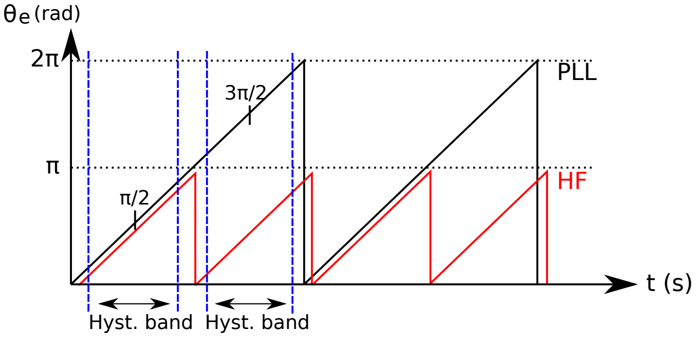

Figure 4.7: Angle polarity determination strategy for transitions from PLL based estimation to HFI.

In this way, a robust position polarity detection and, consequently, a reliable change between PLL and HFI modes is ensured. The polarity estimation performed by means of the PLL information is robust, because there is enough back-EMF for the PLL during the speed range in which the polarity determination is carried out.

Additionally, a speed dependant LUT is included in the sensorless structure (figure 4.5, position offset compensation block) in order to compensate the offsets produced due to the usage of filters in the HFI post-processing. The phase differences introduced by the aforementioned filters are calculated offline and the corresponding position errors are mapped and compensated for all the HFI operation points.

Once the estimated $\widehat{\theta}_{EST}$ position is obtained (figure 4.5), the rotor speed is calculated from its sawtooth (figure 4.5). As the use of derivative calculations under noisy environments are a common source of errors, a robust speed determination method is introduced (figure 4.8). Firstly, the position sawtooth gradient is obtained setting a delay d between samples. After that, a sawtooth error compensation block is included in order to avoid errors produced by 2π-to-0 transitions (or vice versa). Once the speed $\hat{\omega}_e$ is obtained, a glitch suppressor strategy cancels evident unreal glitches that can occur due to noises. Finally, a low pass filter is added to reduce possible remaining noise. The cutting frequency of this filter must be set according the acceleration dynamics of the drive.

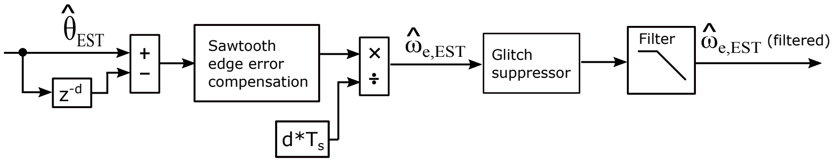

Figure 4.8: Speed estimation process from $\widehat{\theta}_{EST}$.

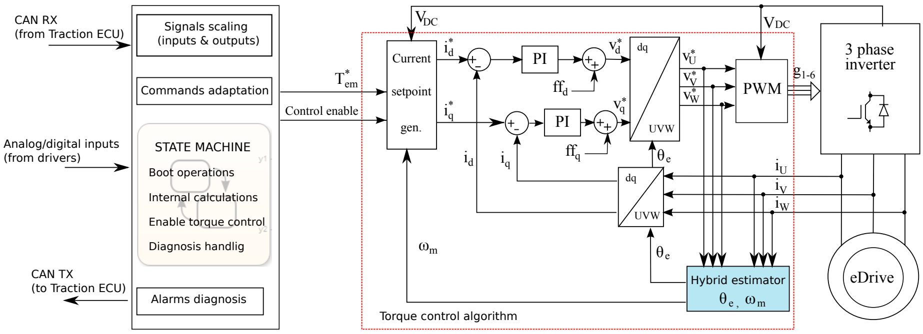

Figure 4.9: Diagram of the simulation model implemented in Matlab/Simulink for the validation of the proposed hybrid sensorless control.

4.3 Simulation results

In order to validate the proposed hybrid sensorless strategy throughout simulation, a 64 kW automotive SM-PMSM and its corresponding power electronics and torque control algorithm (including the hybrid angle and speed estimator) have been implemented in Matlab/Simulink (figure 4.9). A Model in the Loop (MiL) approach has been followed, taking care of the communications and programming protocols of the EV industry

Regarding the control algorithm, a conventional PI based FOC strategy has been used for current regulation. The most significant nominal parameters of the SM-PMSM are listed in table 4.1. The machine employed in this particular case is highly linear; thus, the magnetic saturation is negligible. However, considering the magnetic saturation effect of the PM flux in the d-axis inductance, a saliency level of 10 % has been included in the model ($L_d = 0.9L_q$). In this way, the performance of the proposed sensorless algorithm is studied in

Table 4.1: Most significant nominal parameters of the simulated SM-PMSM.

Parameter	**Symbol**	**Value**	**Units**
Nominal power	P_N	64	kW
Nominal torque	T_N	145	Nm
Maximum speed	ω_{max}	8000	rpm
Stator Resistance	R_s	0.0191	Ω
d-axis nominal inductance	L_d	0.263	mH
q-axis nominal inductance	L_q	0.292	mH
Permanent Magnet Flux linkage	Ψ_{PM}	0.0731	Wb

simulation for synchronous machines with low saliency. As the saliency is very low, the i_d current has not been considered for torque production and $i_d = 0$ control has been adopted for the MTPA region (section 3.2.2). Being a machine without a MTPV region, a conventional flowchart based i_d regulation has been included for FW control. In this context, the proposed hybrid sensorless algorithm adjustment parameters are provided in table 4.2. These parameters have been adjusted experimentally. Note that the filters used for the HF current processing stage (figure 4.4) have been obtained throughout the MATLAB fdatool toolbox.

On the one hand, figure 4.10 shows the simulation results obtained using only the PLL for the estimation of the rotor angle (in this particular case, without closing the loop with the estimated angle) from medium/high to low speeds and standstill. As it has been advanced in the state of the art, this method is only suitable for its implementation at medium/high speeds. Simulation results show that the error between the position provided by the resolver θ_e versus the estimated position $\widehat{\theta_e}$ is very low at medium/high speeds (figures 4.10(a) and 4.10(b)). However, this error significantly increases when lowering the speed, up to a point where angle tracking is lost by the PLL (at around 100 rpm). Thus, these results provide valuable information for the selection of the transition points of the proposed hybrid sensorless controller.

On the other hand, figure 4.11 shows the results obtained for the HFI strategy at very low and zero speeds. As it can be seen, the HFI technique is able to track the angle up to standstill and with a very low estimation error (figure 4.11(b)), proving that a combination of both techniques is adequate for developing a wide speed sensorless control. The mechanical speed is also accurately estimated using the proposed robust estimator (figure 4.11(c)).

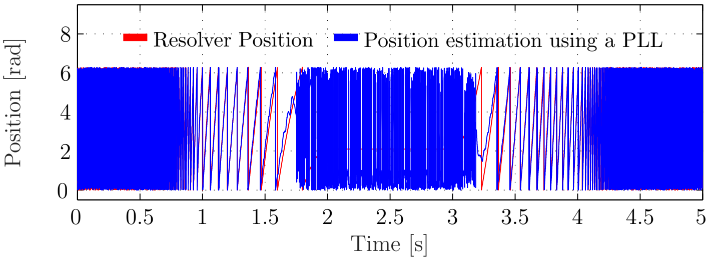

(a) Estimated rotor angle (PLL) vs real rotor angle.

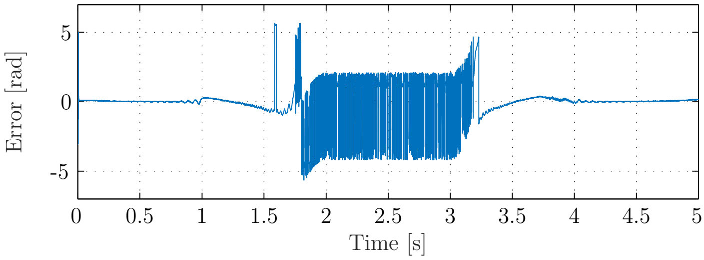

(b) Position error of the PLL estimation.

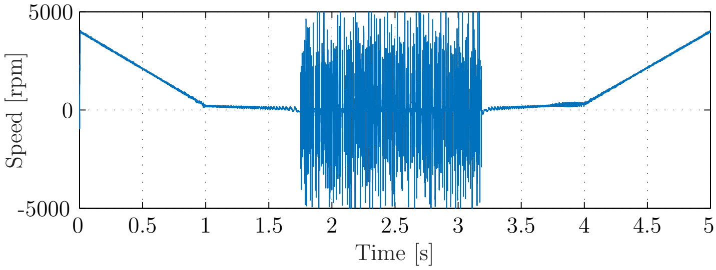

(c) Estimated mechanical speed of the machine using the PLL.

Figure 4.10: PLL position estimation from high speed to standstill in the simulated SM-PMSM.

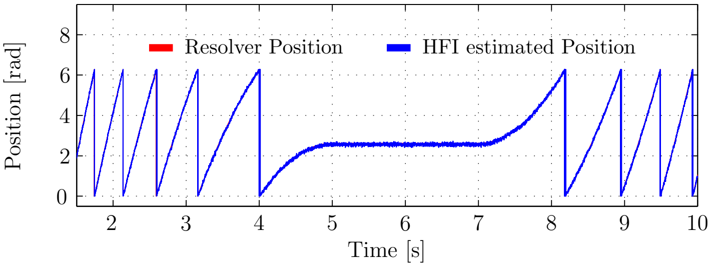

(a) Estimated rotor angle (HFI) vs real rotor angle.

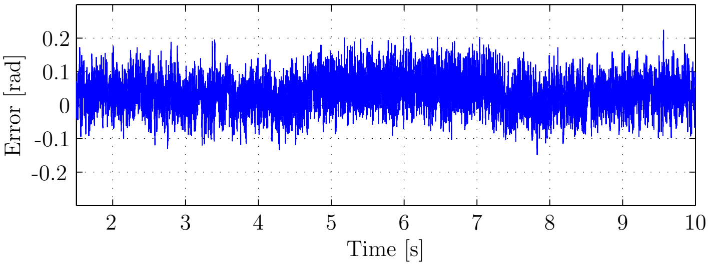

(b) Position error between resolver and HFI estimation.

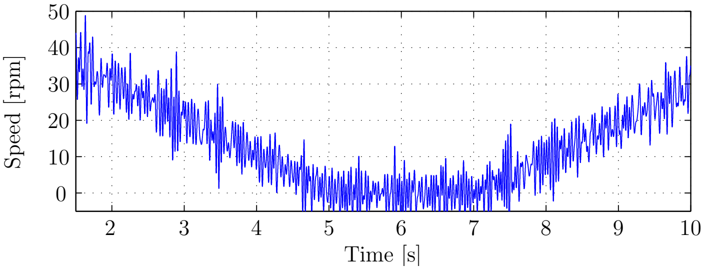

(c) Estimated mechanical speed of the machine using the HFI technique.

Figure 4.11: HFI technique position estimation at low speeds and standstill in the simulated SM-PMSM.

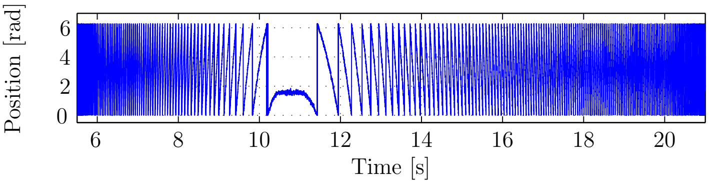

(a) Estimated position with the proposed hybrid sensorless structure.

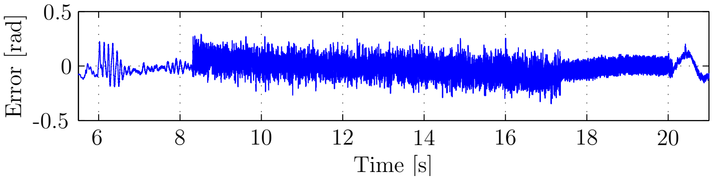

(b) Position error between resolver and the proposed hybrid sensorless.

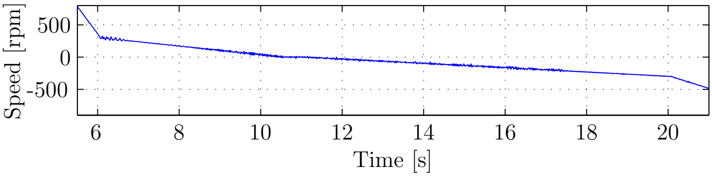

(c) Speed estimation with the proposed hybrid sensorless structure.

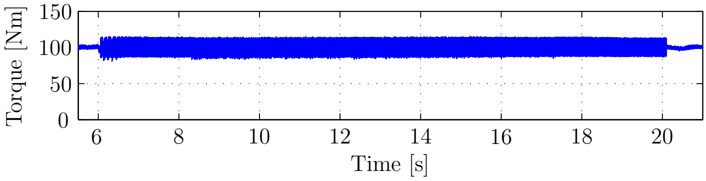

(d) Estimated torque.

Figure 4.12: Proposed hybrid sensorless control for 100 Nm (simulation results).

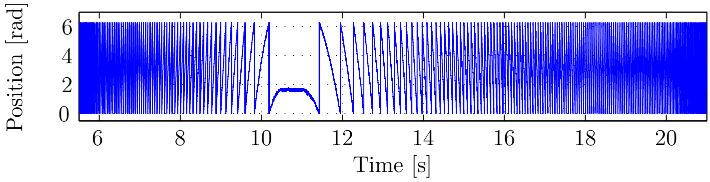

(a) Estimated position with the proposed hybrid sensorless structure.

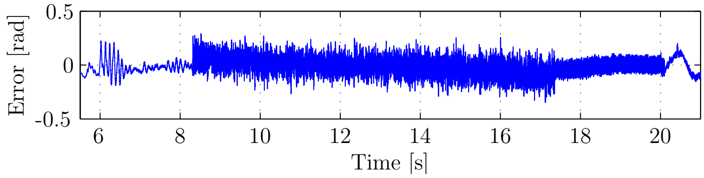

(b) Position error between resolver and the proposed hybrid sensorless.

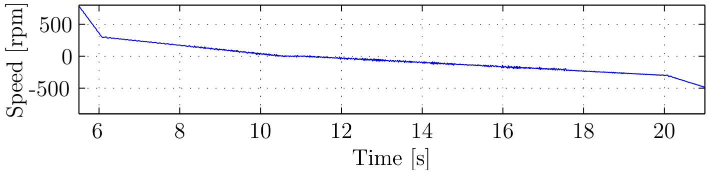

(c) Speed estimation with the proposed hybrid sensorless structure.

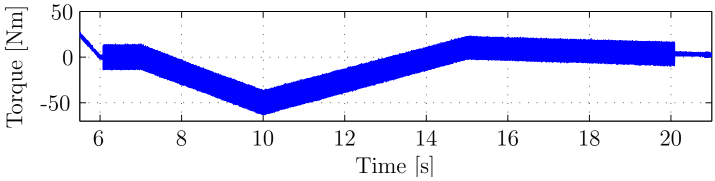

(d) Estimated torque.

Figure 4.13: Proposed hybrid sensorless control in four quadrant operation (simulation results).

Table 4.2: Proposed hybrid sensorless algorithm parameter settings for SM-PMSM simulation tests.

HFI technique parameters			
Item	**Symbol**	**Value**	**Units**
Voltage amplitude	V_i	30	V
Frequency	f_i	1000	Hz

PLL based back-EMF estimator parameters			
Item	**Symbol**	**Value**	**Units**
Positive proportional gain	K_p^+	1.7426	-
Positive integral gain	K_i^+	476.51	-
Negative proportional gain	K_p^-	10	-
Negative integral gain	K_i^-	200	-

Transition algorithm parameters			
Item	**Symbol**	**Value**	**Units**
PLL speed threshold	$\omega 1$	300	rpm
Hysteresis limit speed thrshold	$\omega 2$	225	rpm
HFI technique speed threshold	$\omega 3$	150	rpm
Hysteresis band	$HystBand$	1.5	rad
Speed compensator delay	d	50	samples

Figures 4.12 and 4.13 provide the simulation results obtained with the proposed hybrid sensorless control (closing the loop with the estimated angle) for 100 Nm and for four quadrant operation, respectively. The PLL-to-HFI and HFI-to-PLL transitions are smoothly carried out, following the transition criteria described in figure 4.6. As it can be seen in figure 4.13(d), additional torque ripple is produced due to the HF signal injected in the interval $[-\omega_1, \omega_1]$, increasing the power losses of the system. Both sensorless strategies (PLL and HFI techniques) introduce an error of the electrical angle within the range of ± 0.25 rad (figures 4.11, 4.12 and 4.13), which can be considered as an acceptable result for closing the loop with the estimated angle. The simulation results show that the proposed hybrid sensorless solution provides the required limp-home capability.

Table 4.3: Proposed hybrid sensorless algorithm parameter settings for experimental tests in the automotive 51 kW PM-assisted SynRM machine.

HFI technique parameters			
Item	**Symbol**	**Value**	**Units**
Voltage amplitude	V_i	60	V
Frequency	f_i	1000	Hz

PLL based back-EMF estimator parameters			
Item	**Symbol**	**Value**	**Units**
Positive proportional gain	K_p^+	5	-
Positive integral gain	K_i^+	1500	-
Negative proportional gain	K_p^-	5	-
Negative integral gain	K_i^-	200	-

Transition algorithm parameters			
Item	**Symbol**	**Value**	**Units**
PLL speed threshold	$\omega 1$	1000	rpm
Hysteresis limit speed thrshold	$\omega 2$	975	rpm
HFI technique speed threshold	$\omega 3$	800	rpm
Hysteresis band	$HystBand$	1.5	rad
Speed compensator delay	d	50	samples

4.4 Experimental results

Finally, the proposed hybrid sensorless strategy has been validated in the 51 kW PM-assisted SynRM used in chapter 3. This machine has high non linearities and a significant saliency (figure 3.19). The most relevant nominal parameters of the machine are summarized in table 3.2. The automotive test bench used for the experimental validation is detailed in appendix C. Regarding the control algorithm, a second order SMC has been used for current regulation, while the proposed hybrid LUT/VTC based algorithm has been included for FW regulation (chapter 3).

The most significant parameters of the proposed hybrid sensorless strategy are shown in table 4.3. Again, these parameters have been adjusted experimentally. At a first stage and using a trial and error procedure, the minimum V_i and ω_i HFI algorithm parameters have been determined. In this particular situation, V_i has been set to 60 V (18.75 % of the available DC bus), with a rotating frequency $f_i = \omega_i/2\pi$ of 1 kHz and the following speed thresholds: $\omega 1$, $\omega 2$ and $\omega 3$ of 1000 rpm, 975 rpm and 800 rpm, respectively. This means that the HFI is active below 8.83 % of the SynRM speed range.

With regard to the tuning of the HFI algorithm filters, the same procedure followed in simulation (section 4.3) has been carried out. In the speed determination procedure, the distance between samples has been set to d = 50 and a 4^{th} order IIR Butterworth low pass filter with a cut off frequency of f_c=10 Hz has been included.

Filter design requires special attention when implementing a HFI technique in a microprocessor, as the accuracy of the angle estimation directly depends on the correct adjustment of the filters. There are two important aspects to bear in mind when implementing such filters:

(a) Frequency specifications: Proper sample frequency (f_s), passing frequency (f_{pass}) and stop frequency (f_{stop}) are needed to ensure a correct operation in the frequency bands.

(b) Filter order: High order filters discriminate better the unwanted frequency components, at the cost of significantly incrementing the computational burden.

Figure 4.14 shows experimental results of the current processing procedure (section 4.2.2) required to extract the rotor position information. Additionally, an analysis of the current processing stage in the frequency domain is provided in figure 4.15, where[5]:

1. In figure 4.15(a), the PM-assisted SynRM is rotating at around 9.76 Hz and the HF signal is injected at 1000 Hz.

2. Once the fundamental frequency is removed using the BPF (figure 4.15(b)), the HF components lie on 1000 Hz and $(1000 - 2 \times 9.76)$ Hz, i.e. 976 Hz.

3. In figure 4.15(c), a rotation of coordinates moves the HF current at 1000 Hz to DC, while the position signal is moved 1000 Hz further away, lying on $(2000 - 2 \times 9.76)$ Hz , i.e. 1982 Hz.

4. The effect of the HPF used to remove the DC component produced by the previous rotation transformation is shown in figure 4.15(d).

---

[5] Slight inaccuracies are consequence of the FFT processing and low sampling frequency.

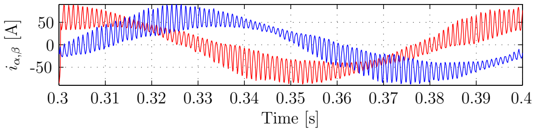

(a) $i_{\alpha\beta}$ measured including HF.

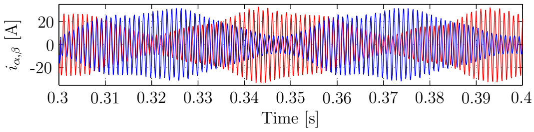

(b) Step 1: $i_{\alpha\beta}$ after BPF.

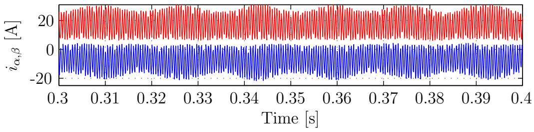

(c) Step 2: $i_{\alpha\beta}$ after the coordinates rotation.

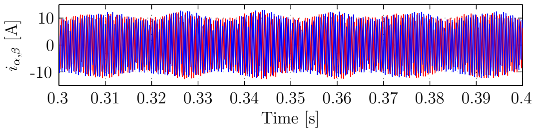

(d) Step 3: $i_{\alpha\beta}$ after HPF.

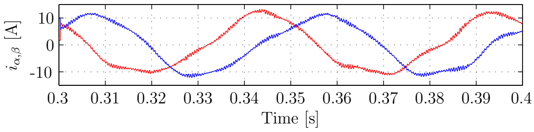

(e) Step 4: $i_{\alpha\beta}$ after the coordinates rotation.

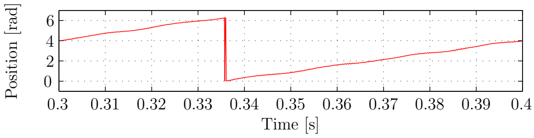

(f) Obtained rotor position.

Figure 4.14: Measured currents post-processing to obtain the rotor position.

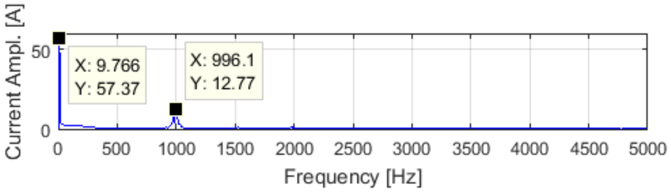

(a) i_α measured spectrum including HF.

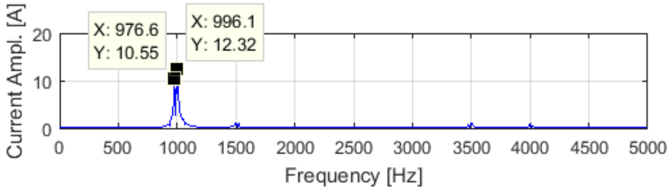

(b) Step 1: i_α spectrum after BPF.

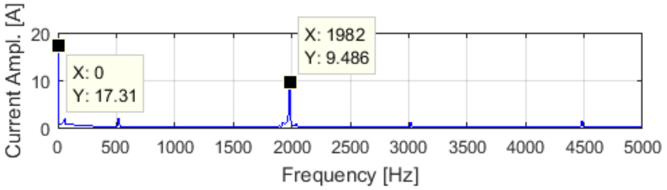

(c) Step 2: i_α spectrum after coordinates rotation.

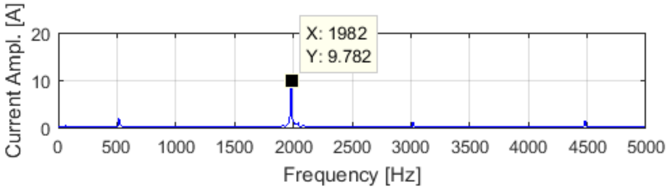

(d) Step 3: i_α spectrum after HPF.

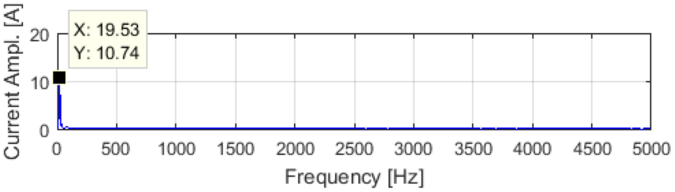

(e) Step 4: i_α spectrum after coordinates rotation.

Figure 4.15: Current signal processing in the frequency domain.

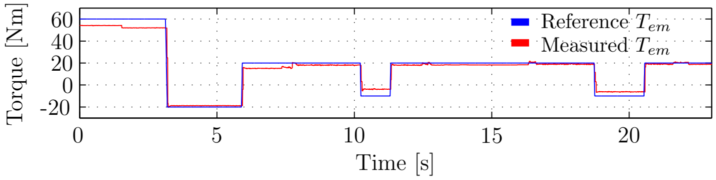

(a) Torque control (reference torque vs measured torque using a torquimeter).

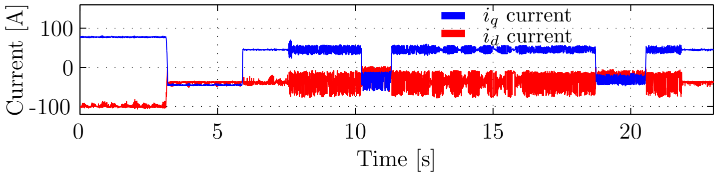

(b) Measured currents in the dq axis.

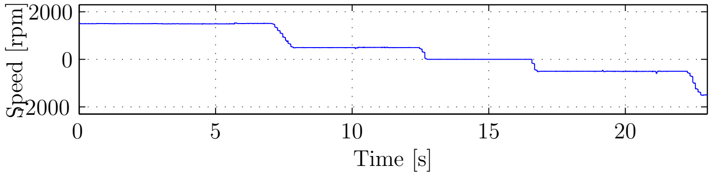

(c) Mechanical speed.

Figure 4.16: Hybrid sensorless torque control experimental results in four quadrant operation.

5. Finally, in figure 4.15(e), a back rotation to the synchronous frame is used to obtain the current component containing the position information at 2×9.76 Hz, i.e. 19.53 Hz.

The speed oscillations in the estimated angle are produced by the load machine speed control when operating at low speeds, and are not related to the HFI algorithm.

Regarding the sensorless torque control, figure 4.16 shows the satisfactory performance of the proposed hybrid algorithm in four quadrant operation. Figure 4.16(b) clearly shows the additional ripple produced by the HFI when oper-

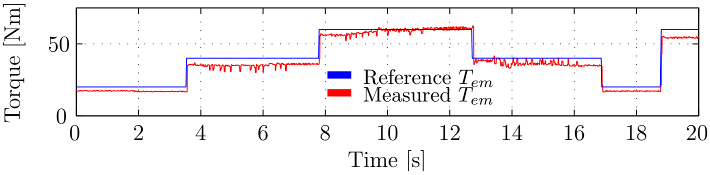

(a) Torque control (reference torque vs measured torque using a torquimeter).

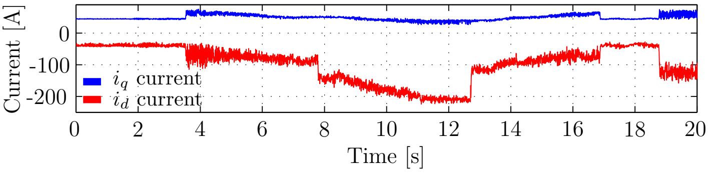

(b) Measured currents in the dq axis.

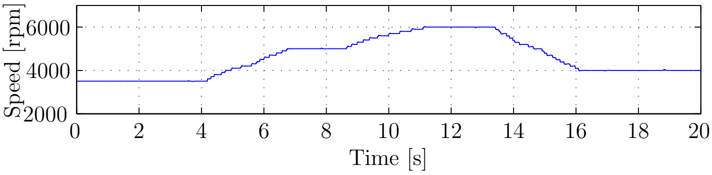

(c) Mechanical speed.

Figure 4.17: Hybrid sensorless torque control experimental results at medium/high speeds and interacting with the proposed VCT based FW control.

ating below 1000 rpm[6]. From figures 4.16(a) and 4.16(b), it can be deduced that the proposed transition procedure ensures smooth operation between the PLL and the HFI technique. Additionally, the estimation algorithm provides the sufficient field orientation, as the measured torque (using a torquimeter) follows the reference one with a very low error (figure 4.16(a)). It is important to note that the torquimeter is not able to measure the high frequency component of the electromagnetic torque (the HF torque is filtered by the mechanical load).

---

[6] An acoustic noise increase has been appreciated during HFI. However, no measurement device has been available for its quantification.

Finally, figure 4.17 shows the hybrid sensorless performance at medium/high speeds, interacting satisfactorily with the proposed FW algorithm (chapter 3). The experimental results confirm the validity of the proposal for limp-home operation.

4.5 Conclusions

From the state of the art, it has been concluded the importance of relying on fault tolerant strategies in EV applications, such as sensorless control. In this chapter, a hybrid sensorless strategy that combines a PLL and a HFI technique has been proposed to provide limp-home capability to EVs under rotor position sensor (resolver or encoder) fault. The contribution has been validated throughout simulation for a SM-PMSM, and has been experimentally tested for a PM-assisted SynRM, concluding its suitability for both low and high salient synchronous machines.

This contribution has been experimentally validated up to 60 Nm and 6000 rpm (approximately 50 % of the machine torque/speed range), providing the sufficient operation range for limp-home. Finally, it has been demonstrated that the proposed sensorless strategy can be successfully combined with advanced control strategies such as the second order SMC or the proposed hybrid 2-D LUT/VCT FW algorithm.

Chapter 5

Conclusions and future work

5.1 Conclusions and summary of the most relevant contributions

According to the state of the art, the IPMSM is one of the most established electric machine technology in modern EV propulsion systems due to its high reluctant torque, high power density, good efficiency around base speed and extended field weakening range. Despite the maturity of this technology and for several reasons, rare-earth free machines such as PM-assisted SynRMs are currently being investigated as an alternative. The behaviour of both automotive IPMSMs and PM-assisted SynRMs can be described using the same mathematical equations, making it possible to use the same approaches for their electromagnetic torque regulation.

Due to an automotive synchronous machine design and functional requirements (i.e., operation beyond the base speed), FW control is mandatory. In this context, a great number of FW control solutions can be found in the literature. As the MTPA and MTPV regions require complex calculations, specially considering that these machines are highly non-linear, the optimum current set points are generally determined following the well established Look up Table (LUT) based approach. The optimal d- and q-axis current references are precalculated and stored in LUTs. However, these set points depend entirely on the knowledge of the machine electric parameters, jeopardizing the system controllability in field weakening operation if significant parameter deviations occur. Therefore, it is of relevant importance to rely on robust control strategies that ensure machine controllability in the whole EV operation range under parameter uncertainties.

As a first contribution, this thesis presents two novel hybrid LUT/VCT based FW control strategies that significantly improve the robustness of current torque control strategies in field weakening. The proposed strategies consider the optimization of the LUT dimensions, minimizing the amount of memory required for their implementation in an automotive microcontroller. In this sense, it is demonstrated that 2-D LUTs (which only consider the mechanical speed and the torque set-point) can be effectively used for proper torque regulation, as the dimension that corresponds to the DC link voltage can be eliminated using the speed normalization concept. On the other hand, two alternative VCT feedback loops (flowchart based and integration based VCT approaches) are introduced in the dimension related with the mechanical speed of the machine, ensuring proper field weakening operation under significant parameter deviations. Both strategies guarantee that the system remains under the maximum voltage constraint in both field weakening and deep field weakening operation regions, and are only active when a predefined voltage constraint limit is reached.

Simulation results that validate both strategies have been carried out using a detailed IPMSM model in Matlab/Simulink, and deviations of +10 % have been imposed to the electrical parameters. If no additional robust strategy is included to the LUT based set-point generation algorithm, controllability is only guaranteed up to 51 % of the EV speed operation range for this particular machine. This limitation is unacceptable from the end-user point of view. The usage of the proposed VCT feedbacks overcomes this issue and, once applied, the machine can work in the whole operation range following a pseudo-optimal operation.

The main advantage of these VCT feedbacks relies on the fact that no machine parameter knowledge is required in their implementation. Regarding practical implementation aspects, the flowchart based method requires to set two control parameters, while only one parameter is required for the integration based method. Besides, the computational burden is lower in the integration based strategy than in the flowchart one. It is also demonstrated by simulation that a slightly better voltage constraint regulation is achieved using the integrator based alternative. Due to these reasons, the integration based VCT has been considered for the experimental validation. Regarding current regulators, the commonly used PI based FOC strategy has been replaced by a second order

SMC due to its suitability for controlling machines suffering high non-linearities.

The experimental validation has been conducted in a 51 kW PM-assisted SynRM. LUT content has been precalculated using the data provided by the manufacturers and obtained from 2.5D FEM analysis. Significant deviations between FEM data and the real machine have been found, specially due to possible manufacturing tolerances. It has been demonstrated that, when the VCT feedback has not been included, uncontrolled regeneration was produced at 30 % of the vehicle maximum speed due to incorrect FW control. In this particular case, the vehicle maximum speed would be limited to 40 km/h, which would be also unacceptable for the end-user. However, system robustness is guaranteed in the whole speed operation range when the proposed additional control loop is included. The proposed strategy has also been evaluated under real driving conditions throughout the standard Worldwide harmonized Light vehicles test Procedure (WLTP). The results confirm that the proposed strategy is ready to be implemented in real EVs.

The proposed FW control strategy can be also considered useful for large scale machine production, as it simplifies the pre-commissioning of each machine unit. Additionally, the VCT regulator only operates when required (in a pseudo-optimal operation point), and maintains the predefined set points (theoretically in an optimal operation point) when proper FW control is achieved with LUT data.

On the other hand, it has been found that reliability is being considered as a crucial requirement for future EV propulsion systems. The content of the ISO 26262 automotive safety standard has motivated the development of fail secure drive systems. One of the most critical failures in an EV concerns to the resolver sensor, whose fault would involve catastrophic consequences for the system. Therefore, special effort is being given nowadays to the development of resolver fault tolerant strategies, conceived to operate in a degraded mode, also known as limp-home operation. During such operation, a sensorless control strategy must be used in order to guarantee the continuous operation of the machine.

EV sensorless operation requires a back-EMF estimator for the estimation of the rotor position at medium to high speeds and a saliency based technique at low speeds and standstill. In this context, this thesis proposes a hybrid sensorless strategy based on a PLL estimator and a HFI based saliency detection technique. The combination of two techniques requires a correct procedure in order to ensure a smooth transition between them. A great number of hybrid sensorless strategies have been proposed in the scientific literature, being the use of weighting coefficients one of the most common changeover methods. Taking into account the additional power losses and mechanical stress introduced by the HFI in the system, it is highly recommended to restrict its use, avoiding unnecessary injection during medium/high speed operation. The used HFI requires an on the fly angular position polarity determination when the system returns from PLL to HFI sensorless operation. In this sense, the reviewed scientific bibliography did not provide detailed information concerning this issue. In this context, the second contribution of this thesis has been focused on the development of a hybrid sensorless algorithm, incorporating a robust transition strategy including the magnets polarity determination. Additionally, a solution to overcome the PLL speed reversal limitations has also been provided.

The proposed limp-home sensorless strategy has been preliminarily validated in Matlab/Simulink for a synchronous machine with low saliency. On the other hand, this algorithm has been experimentally validated in a 51 kW automotive PM-assisted SynRM platform with significant saliency. Experimental results show that approximately 50 % of the torque production capability and speed range of the machine has been successfully maintained using the proposal, allowing the sufficient limp-home capability for the EV in derated mode. Additionally, it has been demonstrated that the proposed sensorless strategy can be successfully combined with advanced control strategies such as the second order SMC, or the previously proposed hybrid 2-D LUT/VCT strategy.

5.2 Publications derived from this thesis

In the following, the journal and conference publications derived from this thesis are presented. Table 5.1 shows the correspondence between the publications and the content of the chapters of this thesis.

5.2.1 Publications in scientific journals

The following publications, which are fully related with the content of this thesis, have been published in scientific journals:

J1) **E. Trancho**, E. Ibarra, A. Arias, I. Kortabarria, J. Jurgens, L. Marengo, A. Fricasse, J. Gragger. "*PM-Assisted Synchronous Reluctance Machine Flux Weakening Control for EV and HEV Applications*", IEEE Transactions on Industrial Electronics, vol. 65, no 4, pp. 2986-2995, April 2018.

Ranking (2016): Q1 (Automation and Control Systems, 1/59).

Journal Citations Reports (JCR) Impact Factor (2016): 7.168.

Table 5.1: Publications derived from this thesis and their correspondence with document chapters.

Chapter	Title	Publication
2	Electric vehicle drive systems: Electric machines and control	J2, J4, C7
3	Look-up table based flux weakening strategy including novel voltage constraint tracking feedback	J1, C2, C4, C6
4	Hybrid sensorless control solutions for limp-home operation of automotive synchronous machines	J3, C1, C3, C5

In this paper, a novel robust torque control strategy against parameter variations and uncertainties for PM-assisted SynRM drives applied to EVs and HEVs is presented. The proposed strategy focuses on field weakening and deep field weakening operation, and it guarantees electric vehicle drive controllability in the whole speed/torque operation range and during the whole propulsion system lifetime. The proposal is experimentally validated in a full scale automotive test bench including a 51 kW prototype for being further implemented in real hybrid and electric vehicles.

J2) **E. Trancho**, E. Ibarra, A. Arias, N. Sabihi, I. López. "*Ibilgailu elektrikoen propultsio-sistemak: motore electrikoak eta horien kontrola*", EKAIA, special issue on power electronics and power systems, pp 61-82, 2017.

This article provides an updated state of the art regarding the electric machine technology used in current EV and HEV applications. In this context, the most common torque control strategies are explained and compared. On the other hand, position and speed sensorless control strategies are discussed and, finally, challenges and future trends of EV/HEV electric drive technology are provided.

On the other hand, the following publications are partially related with the thesis and have been submitted to be considered for publication in two relevant scientific journals:

J3) **E. Trancho**, E. Ibarra, I. Kortabarria, P. Prieto, I. Martínez de Alegria, J. Andreu, I. López. "*Efficiency Loss Evaluation of High Frequency Injec-*

tion based Sensorless Control in Light-duty EVs under Standardized Urban Driving Cycles", Applied Energy (Elsevier). Under review.

Ranking (2016): Q1 (Energy and Fuels, 6/92).

Journal Citations Reports (JCR) Impact Factor (2016): 7.182

In this paper, a hybrid position estimation strategy suitable for a variety of synchronous machines is presented and experimental validated in a 51 kW PM-assisted SynRM. The sensorless algorithm operation requirements are determined from the experimental results. The impact of the additional motor and inverter power losses produced by the HFI technique along real automotive driving cycles are quantified using state of the art digital simulation, demonstrating the feasibility of sensorless operation in EV applications from an efficiency point of view.

J4) A. Arias, E. Ibarra, **E. Trancho**, R. Griñó, I. Kortabarria, J. Caum. "*Novel Control Solution for High Speed PMSM Applied to EV and HEV*", Journal of the Franklin Institute - Engineering and Applied Mathematics (Elsevier). Under review.

Ranking (2016): Q1 (Automation and Control Systems, 14/60)

Journal Citations Reports (JCR) Impact Factor (2016): 3.139

The trend for next generation automotive electric machines consists on increasing the mechanical speed and, hence, the electrical frequency of the synthesized stator voltages and currents. This can lead to relevant control challenges when using conventional control structures with sampling period constraints. In this paper, the FOC stability under high speed operation is studied using theoretical and simulation approaches. A control structure that overcomes these stability problems and extends the speed operation range of a PMSM without significant magnetic saturation is presented.

5.2.2 Conference publications

The following conference publications are fully related with the content of this thesis:

C1) **E. Trancho**, E. Ibarra, A. Arias, I. Kortabarria, P. Prieto, "*A practical approach to HFI based Sensorless Control of PM-assisted Synchronous*

Reluctance Machines applied to EVs and HEVs", in Proc. of the IEEE Industrial Electronics Society Conference (IECON), pp. 1735-1740. Beijing (China), 2017.

This paper presents practical implementation details of the HFI sensorless technique, giving special attention to signal processing, offset compensation due to filtering delays and robust speed estimation. The approach is validated in an automotive PM-assisted SynRM of 51 kW.

C2) **E. Trancho**, E. Ibarra, A. Arias, C. Salazar, I. López, A. Díaz de Gereñu, A. Peña, "*IPMSM Torque Control Strategies based on LUTs and VCT feedback for Robust Control under Machine Parameter Variations*", in Proc. of the IEEE Industrial Electronics Society Conference (IECON), pp. 2833-2838. Florence (Italy), 2016.

In this paper, two novel hybrid IPMSM control strategies, which combine LUTs and VCT feedbacks, are proposed in order to overcome controllability issues during field weakening operation and under machine parameter deviations. Simulation results that demonstrate the validity of the proposed approaches are presented, and both strategies are compared in terms of complexity and performance.

C3) **E. Trancho**, E. Ibarra, A. Arias, C. Salazar, I. López, A. Díaz de Gereñu, A. Peña, "*A Novel PMSM Hybrid Sensorless Control Strategy for EV Applications Based on PLL and HFI*", in Proc. of the IEEE Industrial Electronics Society Conference (IECON), pp. 2833-2838. Florence (Italy), 2016.

In this paper, a novel hybrid sensorless control strategy for PMSM drives applied to EVs is presented. This sensorless strategy covers a wide speed range and also has speed reversal capability. It combines a HFI technique for low and zero speed operation, and a PLL for medium and high speed operation. A solution to achieve a smooth transitions between the PLL and the HFI strategies is also proposed, allowing to correctly detect the rotor position polarity when HFI takes part. Simulation results that show the validity of the proposal are provided.

C4) **E. Trancho**, E. Ibarra, A. Arias, I. Kortabarria, "*Control óptimo de par para máquinas SynRM aplicadas a vehículo eléctrico*", in Proc. of the Seminario Anual de Automática, Electrónica Industrial e Instrumentación (SAAEI), pp. 1-6. Valencia (Spain), 2017.

This paper analyses the design of a reliable torque control algorithm for a PM-assisted SynRM. On the one hand, An offline optimal current reference calculation procedure is explained for the whole speed operation range. On the other, the PI based FOC current regulator adjustment in the z domain is mathematically deduced. Experimental results are provided to validate the implemented control structure.

C5) **E. Trancho**, E. Ibarra, A. Arias, C. Salazar, I. López, A. Díaz de Gereñu, "*Full Speed Range Sensorless Control of Permanent Magnet Synchronous Machines for EV and HEV Applications: State of the Art*", in Proc. of the Seminario Anual de Automática, Electrónica Industrial e Instrumentación (SAAEI), pp. 1-6. Elche (Spain), 2016.

This paper reviews the most significant rotor position and speed estimation methods for PMSMs. Additionally, the paper discusses their suitability for EV and HEV applications. An hybrid sensorless algorithm combining the HFI technique for low speed regions and standstill, and an EKF based solution for medium and high speed regions is implemented. Sensorless simulation results are given to show the suitability of the selected technique for EV applications.

C6) E. Ibarra, **E. Trancho**, M. Dendaluce, A. Díaz de Gereñu, C. Salazar, A. Peña, "*MTPA and Field Weakening Strategies for IPMSMs: State of the Art and Computational Analysis*", in Proc. of the Seminario Anual de Automática, Electrónica Industrial e Instrumentación (SAAEI), pp. 1-6. Elche (Spain), 2016.

In this paper, various Maximum Torque Per Ampere (MTPA) and field weakening control alternatives for PMSMs are reviewed. The computational resources needed for their real-time execution in an automotive certified microprocessor are analysed. A Processor in the Loop (PIL) platform based on the dSPACE TargetLink software has been used in order to carry out the aforementioned analysis, determining the convenience of a LUT based approach for low computational burden.

On the other hand, the following conference publication is partially related with the content of this thesis:

C7) N. Zabihi, I. López, **E. Trancho**, E. Ibarra, A. Peña, "*Switched Reluctance Machines for Electric Vehicles: State of the Art*", in Proc. of the Seminario Anual de Automática, Electrónica Industrial e Instrumentación (SAAEI), pp. 1-6. Elche (Spain), 2016.

In this paper, a state of the art of the most relevant SRM topologies is provided, and their advantages and disadvantages are discussed. Additionally, the most common torque control strategies for SRM drives are categorized, which is followed by a summary of researches that focus on torque ripple and mechanical vibration reduction.

5.3 Industrialization of proposed control solutions

The proposed hybrid LUT/VCT based field weakening algorithm has been successfully implemented in an EV mounting an IPMSM. Up to the date of presentation of this thesis, this vehicle has been certified for on road driving and has covered more than 8000 km.

5.4 Future work

Considering the work carried out in this thesis, the author proposes the following research lines for future investigation:

To extend the main thesis contributions to multiphase synchronous machine technologies

Nowadays, three phase machines are the dominant technologies for automotive propulsion applications. Nevertheless, future trends are focused on providing fault tolerant capabilities and the highest possible power densities to EV propulsion systems, making multiphase machine technologies of great interest.

This thesis has been focused on the development of robust field weakening control algorithms and of fault tolerant control against encoder/resolver failures for three-phase synchronous machines. An interesting research line would be to particularize the proposed control strategies to the multiphase scenario. In this context, a number of multiphase topologies could be investigated:

- Dual (or multiple) three-phase configurations.
- Star connected multiphase systems with an odd phase-number, such as 5-phase, 7-phase and 9-phase configurations.
- Multiphase topologies with open windings and odd phase-number, such as 3-phase, 5-phase, 7-phase or 9-phase configurations.

If feasible, it would also be of interest to particularize the proposed field weakening and sensorless techniques for their operation under open circuit faults in machine windings or power electronics devices of such multiphase systems.

Development of robust torque regulation strategies for next generation high speed synchronous machines

As it can be derived from the state of the art, future trends in EV applications include the development of high speed synchronous machines (with mechanical speeds above 15000 rpm) in order to maximize the power density of the electric drive. This trend can lead to relevant control challenges when using conventional control structures with limited switching frequencies.

A future research line would include the research and development of advanced high speed current regulation strategies for automotive synchronous machines that take into account the high non-linearities of this particular machines produced by magnetic saturation.

Investigation on resolver/encoder fault prediction and smooth transition between healthy and limp-home operation

In this thesis, a novel sensorless control solution for limp-home operation has been successfully implemented in a real automotive drive. However, for applications where the reconfiguration between sensored and sensorless operation should be provided while the vehicle is in motion, it is of great interest to provide tools that can predict the occurrence of a sensor fault in advance. In this way, the control algorithm can anticipate to the fault and take the required actions, ensuring a smooth transition between sensored and sensorless operation, while maintaining passenger safety and comfort.

Finally, it would also be of interest to incorporate a start-up procedure to the proposed sensorless strategy, using an approach presented in the scientific literature, or providing a novel initial angle determination solution.

5.5 Acknowledgements

This work has been partially supported by the European Union under the European Project SYRNEMO (grand number 605075), and by the Government of the Basque Country under regional projects KT4ETRANS (KK-2015/00047 and KK-2016/00061) and FPGAmc (EMAITEK programme).

Appendix A

Vector transformations

A.1 Clarke transformation

The Clarke vector transformation (figure A.1) can be used to convert a magnitude represented in a three-phase reference frame (xyz) into a two-phase system ($\alpha\beta o$). In this context, the Clarke matrix is defined as:

$$\begin{bmatrix} X_\alpha \\ X_\beta \\ X_0 \end{bmatrix} = K_1 \begin{bmatrix} 1 & -\frac{1}{2} & -\frac{1}{2} \\ 0 & \frac{\sqrt{3}}{2} & -\frac{\sqrt{3}}{2} \\ K_2 & K_2 & K_2 \end{bmatrix} \begin{bmatrix} x \\ y \\ z \end{bmatrix}, \tag{A.1}$$

where $[UVW]$ and $[X_\alpha X_\beta X_0]$ are the electrical magnitude components in the three-phase and $\alpha\beta$ reference frames, respectively, being the homopolar component $X_o = 0$ for a balanced system. On the other hand, K_1 and K_2 are constants that can take two sets of values:

1. The first set of values consists of defining $K_1 = \sqrt{2/3}$ and $K_2 = 1/\sqrt{2}$. This approach is known as the power invariant transformation. Under these considerations, the value of the power is maintained between both reference systems.

2. Clarke constants can be also defined as $K_1 = 2/3$ and $K_2 = 1/2$ in order to maintain the amplitude of the vector across the transformation. Using this approach, the power and torque equations in the $\alpha\beta o$ plane must be multiplied by $3/2$.

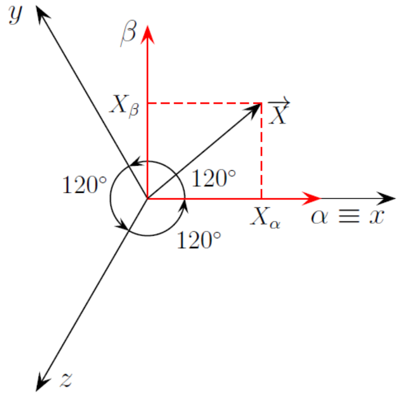

Figure A.1: Clarke transformation.

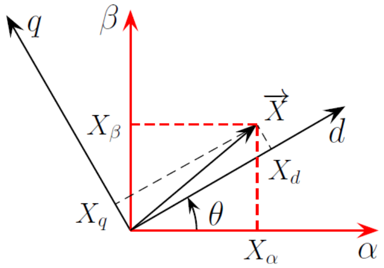

Figure A.2: Park transformation.

This thesis has considered the amplitude invariant transformation (second approach) when required in FOC.

A.2 Park transformation

Finally, the Park transformation converts the $\alpha\beta o$ system into an orthogonal rotating reference frame (dqo), as shown in figure A.2. The Park matrix transformation is defined as:

$$\begin{bmatrix} X_d \\ X_q \\ X_o \end{bmatrix} = \begin{bmatrix} \cos\theta & \sin\theta & 0 \\ -\sin\theta & \cos\theta & 0 \\ 0 & 0 & 1 \end{bmatrix} \begin{bmatrix} X_\alpha \\ X_\beta \\ X_o \end{bmatrix}, \tag{A.2}$$

where θ is the angle of the dqo reference frame with respect to the $\alpha\beta o$ reference frame. The corresponding anti-transformation matrices can be directly derived from (A.1) and (A.2).

Appendix B

Second order SMC parameter tuning

In this appendix, the selection of the parameter c_j and the tuning equations to adjust the ST parameters λ_j and Ω_j are detailed. The approach presented in [150] has been followed for these calculations, although in this thesis the procedure has been particularized for the current control of a non-linear synchronous machine. For simplicity, only the calculations for $v_{d,eq}$ and $v_{d,ST}$ tuning are presented, while the same procedure should be followed to obtain the q-axis parameters. In this sense, introducing (2.38) and (2.36) into (2.32), the following motor dynamic control law is obtained:

$$\frac{ds_{i_d}}{dt} = -\left[\lambda_d |s_{i_d}|^{1/2} sgn(s_{i_d}) + \Omega_d \int sgn(s_{i_d}) dt\right], \tag{B.1}$$

where the time derivative of (B.1) can be expressed as:

$$\frac{d^2 s_{i_d}}{dt} = -\left[\frac{1}{2}\lambda_d |s_{i_d}|^{-1/2} \frac{ds_{i_d}}{dt} + \Omega_d \frac{s_{i_d}}{|s_{i_d}|}\right]. \tag{B.2}$$

Considering that the sliding regime has been reached, $|s_{i_d}| \leq \delta_d$, being δ_d close to zero. Assuming the worst case ($|s_{i_d}| = \delta_d$) and introducing (2.28) and its time first and second derivatives in (B.2), the following expression is obtained:

$$\frac{d^2 e_{i_d}}{dt} + c_d \frac{de_{i_d}}{dt} = -\left[\frac{1}{2}\lambda_d \delta_d^{-1/2} (\frac{de_{i_d}}{dt} + c_d e_{i_d}) + \Omega_d \frac{(e_{i_d} + c_d \int e_{i_d} dt)}{\delta_d}\right], \tag{B.3}$$

and rearranging (B.3), the following differential equation is deduced:

$$\frac{d^2 e_{i_d}}{dt} + a_2 \frac{de_{i_d}}{dt} + a_1 e_{i_d} + a_0 \int e_{i_d} dt = 0. \tag{B.4}$$

Calculating the time derivative of (B.4), the error dynamic expression is obtained as:

$$\frac{d^3 e_{i_d}}{dt} + a_2 \frac{d^2 e_{i_d}}{dt} + a_1 \frac{de_{i_d}}{dt} + a_0 e_{i_d} = 0, \tag{B.5}$$

being

$$a_2 = c_d + \frac{1}{2}\lambda_d \delta_d^{-1/2}, \tag{B.6}$$

$$a_1 = \frac{1}{2}\lambda_d \delta_d^{-1/2} c_d + \frac{\Omega_d}{\delta_d}, \tag{B.7}$$

$$a_0 = \frac{\Omega_d c_d}{\delta_d}. \tag{B.8}$$

Taking into account the third-order general characteristic equation, defined as:

$$(p^2 + 2\xi w_n p + w_n^2)(p + \alpha \xi w_n) = p^3 + b_2 p^2 + b_1 p + b_0 = 0, \tag{B.9}$$

where

$$b_2 = (2 + \alpha)\xi w_n, \tag{B.10}$$

$$b_1 = (1 + 2\alpha\xi^2) w_n^2, \tag{B.11}$$

$$b_0 = \alpha \xi w_n^3, \tag{B.12}$$

being α a constant that must have a high enough value ($\alpha > 10$) in order to make less relevant the third pole of the system. Finally, the term c_d is directly calculated from (B.9), while Ω_d and λ_d are obtained so that $a_0 = b_0$ and $a_2 = b_2$, respectively:

$$c_d^3 + b_2 c_d^2 + b_1 c_d + b_0 = 0, \tag{B.13}$$

$$\Omega_d = \frac{\alpha \xi w_n^3 \delta_d}{c_d}, \tag{B.14}$$

$$\lambda_d = [(2 + \alpha)\xi w_n - c_d] 2\delta^{1/2}. \tag{B.15}$$

Appendix C

Experimental platform for EV propulsion system testing

In this appendix, the experimental platform used to carry out the validation of the proposed control algorithms (figures C.1 and C.2) is described. This platform is constituted by three main elements, i.e., the test bench cabin, the power train and the vehicle emulator (figure C.3), and it also includes devices for control, monitor and data logging purposes.

The test bench cabin includes the 51 kW PM-assisted SynRM machine under test (figure C.2), mechanically coupled to a counter-load machine. The counter-load IM has a maximum speed of 8000 rpm and a maximum power of 157 kW, and is used to emulate the electric vehicle behaviour (figure C.2). The IM is controlled throughout a regenerative 4-quadrant commercial drive, which allows both torque or speed control modes. In order to emulate the vehicle motion, the counter-load machine is controlled in the speed control mode for this particular application. A 1:1.8 ratio gearbox is included between the IM and the PM-assisted SynRM, allowing a maximum speed up to 14400 rpm for the machine under test. Additionally, a programmable DC voltage source of a maximum output power of 280 kW and a maximum output voltage of 500 V is available to emulate the battery pack. A cooling system (LAUDA RP1845) is also installed

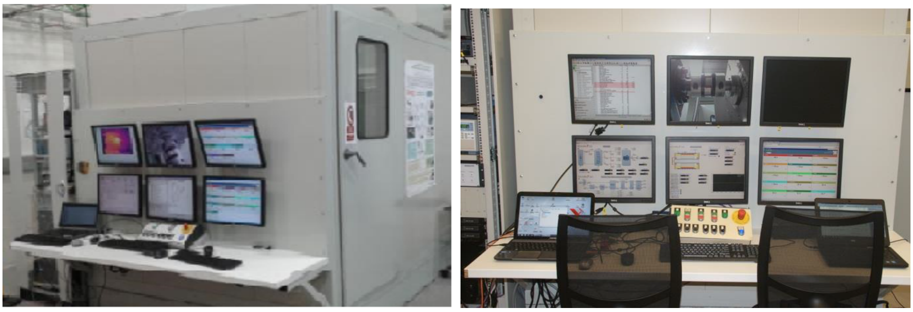

(a) Overview of the test bench.

(b) Devices for control, monitoring and data logging platform.

Figure C.1: Test bench overview, including the monitoring platform.

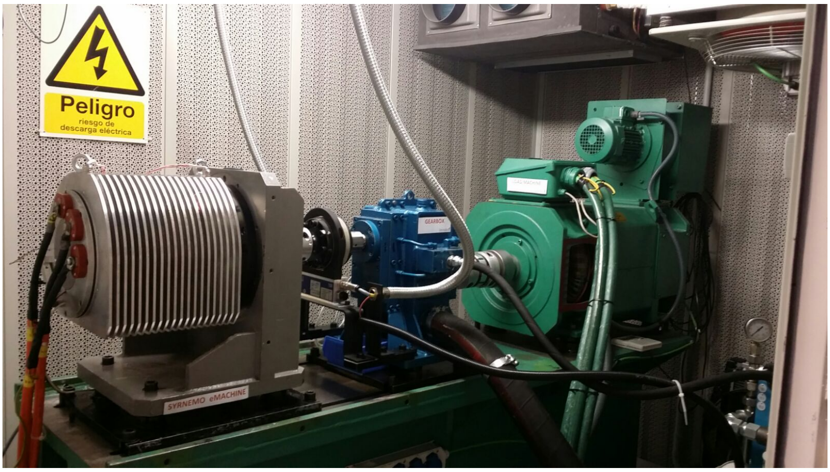

Figure C.2: Tecnalia's automotive test bench cabin overview, including the machine under test (left) and the counter-load machine (right).

in order to cool both the motor and inverter under test[1]. It provides liquid cooling (water/ethilenglycol) with a maximum coolant flow of 25 l/min. Finally,

---

[1] However, in this particular case the motor under test is air cooled; thus, this cooling loop is only required for the counter-load machine cooling.

a climate chamber is also installed to emulate real life operation conditions of the unit under test.

The control algorithms are developed in the Matlab/Simulink environment and implemented in a dSPACE Rapid Control Prototyping (RCP) digital real-time device, including a slot-CPU control board (DS1006) and an AC Motor Control Solutions board. The dSPACE RCP device is connected to an industrial Semikron IGD-1-424-P1N4-DL-FA power inverter, which has a nominal power of 140 kW and a maximum switching frequency of 25 kHz. The dSPACE device and the commercial inverter emulate the control ECU and the power electronics of an automotive eDrive.

Regarding sensors and monitoring, the driveline includes an HBMT40B torque and speed sensor mounted in-line between the load machine and the unit under test. LEM IT 400-S current sensors are also available to measure the DC input current and the three-phase AC output currents. Using the information provided by such sensors, a Yokogawa WT3000 power analyser is used for the evaluation of the drive efficiency and for harmonic waveform analysis.

The test bench includes a software tool to facilitate control, monitoring and data logging. The communication between devices is carried out through Ethernet, CAN and RS232 (figure C.3). The specifically designed software application has been developed under NI LabView and VeriStand. It allows to send commands to each device, calculating, visualizing and storing automatically all the measured variables. Additionally, the application allows to test the performance of the system under a defined driving cycle (customized or standardized). On the other hand, a National Instruments PC based PXI platform (Test bench PXI) is used to interact with the test bench digital devices (figure C.3).

This automotive test bench also allows to carry out Human in the Loop tests (figure C.4). This is achieved using the DYNACAR® product, a complete road vehicle real time model based on LabVIEW. A vehicle can be modelled introducing its design parameters with a dedicated GUI (figures C.4(a) and C.4(b)). This platform considers both longitudinal and lateral dynamics, providing two operation modes: autonomous and manual driving. When selecting the autonomous option, DYNACAR® executes automatic driving cycles, providing the corresponding speed set-point to the load machine and torque set-point to the PM-assisted SynRM machine. When manual driving operation is activated, DYNACAR® makes use of the real steering wheel, pedals (accelerator and brake) and actual torque to reproduce real driving conditions, as shown in figure C.4(c).

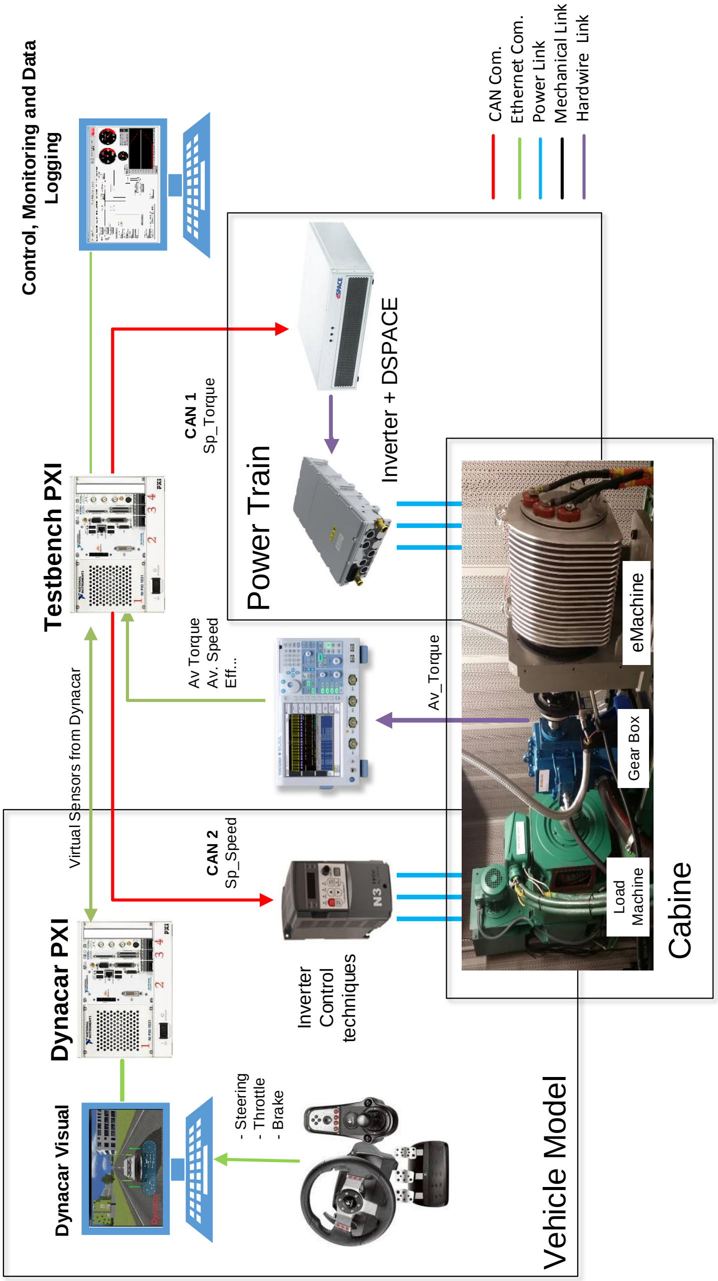

Figure C.3: Test bench communications.

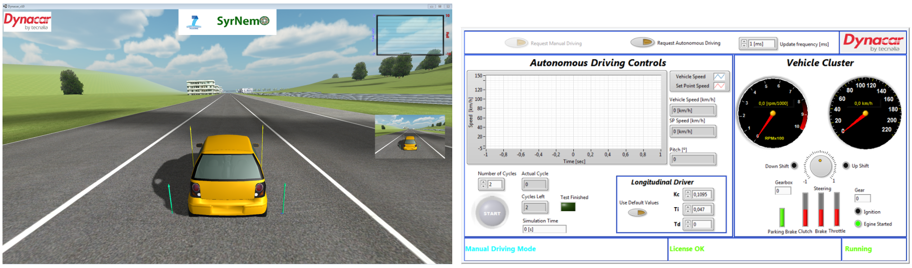

(a) DYNACAR® visual.

(b) DYNACAR® manual/autonomous driving controls.

(c) DYNACAR® vehicle simulator.

Figure C.4: DYNACAR® vehicle model.

Bibliography

[1] International Energy Agency, "Global EV outlook 2016," *Tech report, Clear Energy Ministerial*, 2016.

[2] S. Delprat, T. Guerra, and J. Rimaux, "Optimal control of a parallel powertrain: From global optimization to real time strategy," *in Proc. of the IEEE Vehicular Technology Conference*, 2002.

[3] L. Kumar and S. Jain, "Electric propulsion system for electric vehicular technology: A review," *Renewable and Sustainable Energy Reviews*, vol. 29, pp. 924–940, 2014.

[4] T. Finken, M. Hombitzer, and K. Hameyer, "Study and comparison of several permanent-magnet excited rotor types regarding their applicability in electric vehicles," in *In Proc. of the Emobility - Electrical Power Train Conference*, 2010.

[5] D. Fodorean, L. Idoumghar, M. Brevilliers, P. Minciunescu, and C. Irimia, "Hybrid differential evolution algorithm employed for the optimum design of a high-speed PMSM used for EV propulsion," *IEEE Transactions on Industrial Electronics*, vol. 64, no. 12, pp. 9824–9833, 2017.

[6] A. Bazi, "Electric machines and energy storage technologies in EVs and HEVs for over a century," *in Proc. of the International Electric Machines and Drives Conference*, pp. 212–219, 2013.

[7] J. Alsawalhi and S. Sudhoff, "Design optimization of asymmetric salient permanent magnet synchronous machines," *IEEE Transactions on Energy Conversion*, vol. 31, no. 4, pp. 1315–1324, 2016.

[8] I. Boldea, L. Tutelea, L. Parsa, and D. Dorrell, “Automotive electric propulsion systems with reduced or no permanent magnet: An overview,” *IEEE Transactions on Industrial Electronics*, vol. 61, no. 10, pp. 5696–5711, 2014.

[9] J. Riba, C. López-Torres, L. Romeral, and A. Garcia, “Rare-earth-free propulsion motors for electric vehicles: A technology review,” *Renewable and Sustainable Energy Reviews*, no. 57, pp. 367–379, 2016.

[10] M. Meyer and J. Bocker, “Optimum control for interior permanent magnet synchronous motors (IPMSM) in constant torque and flux weakening range,” in *In Proc. of the Power Electronics and Motion Control Conference (EPE-PEMC)*, 2006, pp. 282–286.

[11] Y. Kim and S. Sul, “Torque control strategy of an IPMSM considering the flux variation of the permanent magnet,” in *Proc. of the Industry Applications Society Conference (IAS)*, 2007.

[12] I. Iwamuro and T. Laska, “IGBT history, state-of-the-art and future prospects,” *IEEE Transactions on Electron Devices*, vol. 64, no. 3, pp. 741–752, 2017.

[13] M. Hofmann, “Evaluation of potentials for infineon SiC-MOSFETs in automotive inverter applications,” *Tech. report, Volkswagen, Fraunhofer IISB*, 2016.

[14] M. Su, C. Chen, S. Sharma, and J. Kikuchi, “Performance and cost considerations for SiC-based HEV traction inverter systems,” *in Proc. of the IEEE Workshop on Wide Bandgap Power Devices and Applications*, 2015.

[15] P. Shamsi, M. McDonough, and B. Fahimi, “Wide-bandgap semiconductor technology - its impact on the electrification of the transportation industry,” *IEEE Electrification Magazine*, vol. 1, no. 2, pp. 59–63, 2013.

[16] P. Rogers, R. Kavasseri, and S. Smith, “An FPGA-based design for joint control and monitoring of permanent magnet synchronous motors,” *in Proc. of the International Conference on ReConFigurable Computing and FPGAs*, 2016.

[17] A. Ruddle, A. Galarza, B. Sedano, I. Unanue, I. Ibarra, and L. Low, “Safety and failure analysis of electrical powertrain for fully electric vehicles and the development of a prognostic health monitoring system,” *in Proc. of the Hybrid and Electric Vehicles Conference*, 2013.

[18] O. Bethoux, E. Laboure, G. Remy, and E. Berthelot, “Real-time optimal control of a 3-phase PMSM in 2-phase degraded mode,” *IEEE Transactions on Vehicular Technology*, vol. 66, no. 3, pp. 2044–2052, 2016.

[19] P. Baraldi, F. Maio, M. Rigamonti, E. Zio, A. Galarza, D. Astigarraga, I. Unanue, I. Ruddle, and S. Rantala, “A procedure for practical prognostics and health monitoring of fully electric vehicles for enhanced safety and reliability,” *in Proc. of the Hybrid and Electric Vehicles Conference (HEVC)*, 2014.

[20] Y. Wang, C. Lee, P. Kuo, and Y. Lin, “Overcurrent protection design, failure mode and effect analysis of an electric vehicle inverter,” *in Proc. of the IEEE International Conference on Industrial Technology*, 2016.

[21] S. Kommuri, S. Lee, and K. Veluvolu, “Robust sensors-fault-tolerance with sliding mode estimation and control for PMSM drives,” *IEEE Transactions on Mechatronics*, DOI: 10.1109/TMECH.2017.2783888, 2017.

[22] E. Dehghan-Azad, S. Gadoue, D. Atkinson, H. Slater, P. Barrass, and F. Blaabjerg, “Sensorless control of IM for limp-home mode EV applications,” *IEEE Transactions on Power Electronics*, vol. 32, no. 9, pp. 7140–7150, 2017.

[23] E. Dehghan-Azad, S. Gadoue, D. Atkinson, H. Slater, P. Barrass, and P. Blaabjerg, “Sensorless control of IM based on stator-voltage MRAS for limp-home EV applications,” *IEEE Transactions on Power Electronics*, vol. 33, no. 3, pp. 1911–1921, 2018.

[24] United States Environmental Protection Agency, “Inventory of U.S. greenhouse gas emissions and sinks: 1990-2015,” *Tech. report, US Government*, 2017.

[25] European Environment Agency, “Greenhouse gas emissions from transport,” *Tech. report*, 2017.

[26] European Commission, “Reducing emissions from transport, a Europe strategy for low-emission mobility,” *Tech. report*, 2014.

[27] ——, “Roadmap to a single Europe transport area - toward a competitive and resource-efficient transport system,” *Tech. report*, 2011.

[28] European Road Transport Research Advisory Council, “The electrification approach to urban mobility and transport,” *Tech. report*, 2009.

[29] A. Zubaryeva and C. Thiel, “Paving the way to electrified road transport,” *Tech. report, European Commission*, 2013.

[30] V. Kaitic, B. Dumnic, Z. Corba, and D. Milicevic, “Electrification of the vehicle propulsion system - an overview,” *Facta universitatis - series: Electronics and Energetics*, vol. 27, no. 2, pp. 299–316, 2014.

[31] A. Emadi, Y. Lee, and K. Rajashekara, “Power electronics and motor drives in electric, hybrid electric, and plug-in hybrid electric vehicles,” *IEEE Transactions on Industrial Electronics*, vol. 55, no. 6, pp. 2237–2245, 2008.

[32] C. Shen, P. Shan, and T. Gao, “A comprehensive overview of hybrid electric vehicles,” *Energy Conversion and Management*, vol. 52, no. 2, pp. 1305–1313, 2011.

[33] Infineon, “Hybrid electric and electric cars - electromobility drive by semiconductor innovations,” *Tech. report, Infineon*, 2017.

[34] M. Ehsani, Y. Gao, and A. Emadi, “Modern electric, hybrid electric, and fuel cell vehicles. Fundamentals, theory and design,” *CRC Press*, 2010.

[35] A. Baltatanu and L. Florea, “Comparison of electric motors used for electric vehicles propulsion,” *in Proc. of the International Conference on Scientific Paper AFASES*, 2013.

[36] C. Chan and K. Chau, *Modern Electric Vehicle Technology.* Oxford Science Publication, 2011.

[37] X. Luo, J. Wang, M. Dooner, and J. Clarken, “Overview of current development in electrical energy storage technologies and the application potential in power system operation,” *Aplied Energy*, vol. 137, pp. 511–536, 2015.

[38] M. Charkhgard and M. Farrokhi, “State-of-charge estimation for lithium-ion batteries using neural networks and EKF,” *IEEE Transaction on Industrial Electronics*, vol. 57, no. 12, pp. 4178–4187, 2010.

[39] D. Haifeng, W. Xuezhe, and S. Zechang, “A new SOH prediction concept for the power lithium-ion battery used on HEVs,” *in Proc. of the Vehicle Power and Propulsion Conference*, 2009.

[40] W. Zhu, Y. Zhu, Z. Davis, and B. Tatarchuk, “Energy efficiency and capacity retention of Ni-MH batteries for storage applications,” *Applied Energy*, vol. 106, pp. 307–313, 2013.

[41] M. Fetcenko, S. Ovshinsky, B. Reichman, K. Young, C. Fierro, and J. Koch, “Recent advances in NiMH battery technology.” *Journal of Power Sources*, vol. 165, pp. 544–551, 2007.

[42] T. Ying, X. Gao, W. Hu, F. Wu, and D. Noreus, “Studies on rechargeable NiMH batteries.” *International Journal of Hydrogen Energy*, vol. 31, pp. 525–530, 2006.

[43] European Commission, “Overview of storage technologies,” *Tech. report*, 2016.

[44] X. Zeng and J. Wang, “A two-level stochastic approach to optimize the energy management strategy for fixed-route hybrid electric vehicles,” *Mechatronics*, vol. 38, pp. 93–102, 2016.

[45] L. Li, B. Yan, J. Song, Y. Zhang, G. Jiang, and L. Li, “Two-step optimal energy management strategy for single-shaft series-parallel powertrain,” *Mechatronics*, vol. 36, pp. 147–158, 2016.

[46] Y. Zhang, L. Chu, Z. Fu, N. Xu, C. Guo, X. Zhang, Z. Chen, and P. Wang, “Optimal energy management strategy for parallel plug-in hybrid electric vehicle based on driving behavior analysis and real time traffic information prediction,” *Mechatronics*, vol. 46, pp. 177–192, 2017.

[47] A. Mayyas, S. Kumar, P. Pisu, J. Rios, and P. Jethani, “Model-based design validation for advanced energy management strategies for electrified hybrid power trains using innovative vehicle hardware in the loop (VHIL) approach,” *Applied Energy*, vol. 204, pp. 287–302, 2017.

[48] C. Yang, S. Du, L. Li, S. You, Y. Yang, and Y. Zhao, “Adaptive real-time optimal energy management strategy based on equivalent factors optimization for plug-in hybrid electric vehicle,” *Applied Energy*, vol. 203, pp. 883–896, 2017.

[49] W. Liu, J. Xu, and J. Tang, “Study on control strategy of urban rail train with on-board regenerative braking energy storage system,” *in Proc. of the Industrial Electronics Society Conference (IECON)*, pp. 3924–3929, 2017.

[50] X. Zhang, D. Gohlich, and J. Li, “Energy-efficient toque allocation design of traction and regenerative braking for distributed drive electric vehicles,” *IEEE Transactions on Vehicular Technology*, DOI: 10.1109/TVT.2017.2731525, 2017.

[51] F. Naseri, E. Farjah, and T. Ghanbari, “An efficient regenerative braking system based on battery/supercapacitor for electric, hybrid, and plug-in hybrid electric vehicles with BLDC motor,” *IEEE Transactions on Vehicular Technology*, vol. 66, no. 5, pp. 3724–3738, 2017.

[52] D. Popa and D. Fodorean, “Design and performances evaluation of a high speed induction motor used for the propulsion of an electric vehicle,” *in Proc. of the International Symposium on Power Electronics, Electric Drives Automation and Motion*, 2014.

[53] T. Finken, M. Felden, and K. Hameyer, “Comparison and design of different electrical machine types regarding their applicability in hybrid electrical vehicles,” *in Proc. of the International Conference on Electrical Machines*, 2008.

[54] H. Zelaya de la Parra, F. Magnussen, and S. Bosga, “Challenges for electric machines and power electronics in automotive applications,” *in Proc. of the International Conference on Mechatronics and Automation (ICMA)*, pp. 784–789, 2009.

[55] W. Cao, B. Mecrow, G. Atkinson, J. Bennett, and D. Atkinson, “Overview of electric motor technologies used for more electric aircraft (MEA),” *IEEE Transactions on Industrial Electronics*, vol. 59, no. 9, pp. 3523–3531, 2012.

[56] J. Urresti, J. Riba, M. Delgado, and L. Romeral, “Detection of demagnetization fault in surface-mounted permanent magnets synchronous motors by means of the zero-sequence voltage component,” *IEEE Transaction on Energy Conversion*, vol. 27, pp. 42–51, 2012.

[57] K. Smith, “Heavy rare earths, permanent magnets and renewable energies: an inminent crisis.” *Energy Policy*, vol. 79, pp. 1–8, 2015.

[58] P. Dent, “High performance magnets materials: risky supply chain,” *Advanced Materials & Processes (AM&P)*, vol. 167, no. 8, pp. 27–30, 2009.

[59] E. Bostanci, M. Moallem, A. Parsapour, and E. Fahimi, “Opportunities and challenges of switched reluctance motor drives for electric propulsion: A comparative study,” *IEEE Transactions on Transportation Electrification*, vol. 3, no. 1, pp. 58–75, 2017.

[60] E. Machacek and N. Fold, “Alternative value chains for rare earths: The anglodeposit developers,” *Resources Policy*, vol. 42, pp. 53–64, 2014.

[61] K. Binnemans, P. Jones, B. Blanpain, T. Gerven, Y. Yang, A. Walton, and M. Buchert, “Recycling of rare earths: A critical review,” *Journal of Cleaner Production*, vol. 51, pp. 1–22, 2013.

[62] T. Graedel, J. Allwood, J. Birat, B. Reck, S. Sibley, G. Sonnemann, M. Buchert, and C. Hagelken, “Recycling rates of metals: A status report, a report of the working group on the global metal flows to the international resource panel,” *Tech. report, United Nations Environment Programme (UNEP)*, 2011.

[63] M. Thompson, E. Chang, A. Foto, J. Citron-Rivera, D. Haddad, R. Waldo, and F. Pinkerton, “Grain-boundary-diffused magnets: The challenges in obtaining reliable and representative BH curves for electromagnetic motor design,” *IEEE Electrification Magazine*, vol. 5, no. 1, pp. 19–27, 2017.

[64] T. Jahns, “Getting rare-earth magnets out of EV traction machines: A review of the many approaches being pursued to minimize or eliminate rare-earth magnets from future EV drivetrains,” *IEEE Electrification Magazine*, vol. 5, no. 1, pp. 6–18, 2017.

[65] W. Zhao, T. Lipo, and B. Kwon, “Comparative study on novel dual stator radial flux and axial flux permanent magnet motors with ferrite magnets for traction application,” *IEEE Transactions on Magnetics*, vol. 50, no. 11, pp. 1–4, 2014.

[66] K. Sone, M. Takemoto, S. Ogasawara, K. Takezaki, and H. Akiyama, “A ferrite PM inwheel motor without rare earth materials for electric city commuters,” *IEEE Transactions on Magnetics*, vol. 48, no. 11, pp. 2961–2964, 2012.

[67] P. Sergeant and A. Van Den Bossche, “Influence of the amount of permanent-magnet material in fractional-slot permanent-magnet synchronous machines,” *IEEE Transactions on Industrial Electronics*, vol. 61, no. 9, pp. 4979–4989, 2014.

[68] T. Kato, N. Limsuwan, C. Yu, K. Akatsu, and R. Lorenz, “Rare earth reduction using a novel variable magnetomagnet force flux-intensified IPM machine,” *IEEE Transactions on Industrial Electronics*, vol. 50, no. 3, pp. 1748–1756, 2014.

[69] S. Chung, J. Kim, Y. Chun, B. Woo, and D. Hong, “Fractional slot concentrated winding PMSM with consequent pole rotor for a low speed direct drive: Reduction of rare-earth permanent magnet,” *IEEE Transactions on Industrial Electronics*, vol. 30, no. 1, pp. 103–109, 2015.

[70] T. Vyncke, R. Boel, and J. Melkebeek, “On extended Kalman filters with augmented state vectors for the stator flux estimation in SPMSMs,” in *Proc. of the Applied Power Electronics Conference*, 2010, pp. 1711–1718.

[71] P. Vas, “Sensorless vector and direct torque control,” *Oxford Science Publications*, 1998.

[72] M. Rahman and P. Zhou, “Analysis of brushless permanent magnet synchronous motors,” *IEEE Transaction on Industrial Electronics*, vol. 43, no. 2, pp. 256–267, 1996.

[73] P. Pillay and R. Krishnan, “Application characteristics of permanent magnet synchronous and brushless DC motors for servo drives,” *IEEE Transactions on Industry Applications*, vol. 27, no. 5, pp. 986–996, 1991.

[74] E. Montalvo-Ortiz, S. Foster, J. Cintron-Rivera, and E. Strangas, “Comparison between a spoke-type PMSM and a PMASynRM using ferrite magnets,” *in Proc. of the IEEE International Electric Machines and Drives*, pp. 1080–1087, 2013.

[75] Y. Jeong, K. Kim, Y. Kim, B. Park, and S. Jung, “Design characteristics of PMa SynRM and performance comparison with IPMSM based on numerical analysis,” *in Proc. of the International Conference on Electric machines*, pp. 164–170, 2012.

[76] X. Liu, H. Chen, and A. Belahcen, “Research on the performance and parameters of interior PMSM used for electric vehicles,” *IEEE Transactions on Industrial Electronics*, vol. 63, no. 6, pp. 3533–3545, 2016.

[77] B. Asaei and B. Rahrovi, “Minimum-copper-loss control over full speed range of an IPMSM drive for hybrid electric vehicle application,” in *Proc. of the IEEE Vehicle Power and Propulsion Conference (VPPC)*, 2010.

[78] A. Chiba, M. Takeno, N. Hoshi, M. Takemoto, S. Ogasawara, and M. Rahma, "Consideration of number of series turns in switched-reluctance traction motor competitive to HEV IPMSM," *IEEE Transactions on Industry Applications*, vol. 48, no. 6, pp. 2333–2340, 2012.

[79] M. Seilmeier and B. Piepenbreier, "Initial start-up and magnet polarity estimation method for HF test current injection based sensorless control of PMSM," *in Proc. of the International Power Electronics and Motion Control Conference and Exposition*, pp. 59–64, 2014.

[80] A. Arias, C. Ortega, J. Zaragoza, J. Espina, and J. Pou, "Hybrid sensorless permanent magnet synchronous machine four quadrant drive based on direct matrix converter," in *International Journal of Electrical Power & Energy Systems*, vol. 45, no. 1, 2012, pp. 78–86.

[81] F. Briz, M. Degner, P. Garca, and R. Lorenz, "Comparison of Saliency-Based Sensorless Control Techniques for AC Machines," *IEEE Transactions on Industry Applications*, vol. 40, no. 4, pp. 1107–1115, 2004.

[82] J. McCraw, "Skin deep, review of tesla model S," *Tech. report, Electric Hybrid Vehicle Technology*, pp. 54–57, 2013.

[83] G. Witzenburg, "GM EV1 - the real story part III," *Tech. report, Green Cars News*, 2008.

[84] M. Zeraoulia, M. Benbouzid, and D. Diallo, "Electric motor drive selection issues for HEV propulsion systems: A comparative study," *IEEE Transactions on Vehicular Technology*, vol. 55, no. 6, pp. 1756 – 1764, 2006.

[85] K. Chau and W. Li, "Overview of electric machines for electric and hybrid vehicles," *International Journal of Vehicle Design*, vol. 64, no. 1, pp. 46–71, 2014.

[86] K. Malekian, M. Sharif, and J. Milimonfared, "An optimal current vector control for synchronous reluctance motors incorporating field weakening," *in Proc. of the IEEE International Workshop on Advanced Motion Control*, pp. 393–398, 2008.

[87] C. Chen, T. Liu, and M. Lin, "Position control of a sensorless synchronous reluctance motor," *IEEE Transactions on Industrial Electronics*, vol. 51, no. 1, pp. 15–24, 2004.

[88] P. Guglielmi, M. Pastorelli, G. Pellegrino, and A. Vagati, "Position-sensorless control of permanent-magnet-assisted synchronous reluctance motor," *IEEE Transactions on Industry Applications*, vol. 40, no. 2, pp. 615–622, 2004.

[89] J. Hsu, T. Burress, S. Lee, R. Wiles, C. Coomer, J. McKeever, and D. Adams, "16000-rpm interior permanent magnet reluctance machine with brushless field exitation," *in Proc. of the IEEE IAS Annual Meeting*, 2008.

[90] A. Vagati, B. Boazzo, P. Guglielmi, and G. Pellegrino, "Ferrite assisted synchronous reluctance machines: A general approach," *in Proc. of the International Conference on Electric machines*, pp. 1315–1321, 2012.

[91] S. Ooi, M. Morimoto, M. Sanada, and Y. Inoue, "Performance evaluation of a high power density PMASynRM with ferrite magnets," *IEEE Transactions on Industry Applications*, vol. 49, no. 3, pp. 1308–1315, 2013.

[92] P. Reddy, K. Grace, and A. El-Refaie, "Conceptual design of sleeve rotor synchronous reluctance motor for traction applications," *IET Electric Power Applications*, vol. 10, no. 5, pp. 368–347, 2016.

[93] Y. Wang, D. Ionel, M. Jiang, and S. Stretz, "Establishing the relative merits of synchronous reluctance and PM-assisted technology through systematic design optimization," *IEEE Transactions on Industry Applications*, vol. 52, no. 4, pp. 2971–2978, 2016.

[94] N. Bianchi, S. Bolognani, E. Carraro, M. Castiello, and E. Fornasiero, "Electric vehicle traction based on synchronous reluctance motors," *IEEE Transactions on Industry Applications*, vol. 52, no. 6, pp. 4762–4769, 2016.

[95] N. Bianchi and Z. Mahmoud, "An analytical approach to design the PM in PMAREL motors robust toward the demagnetization," *IEEE Transactions on Energy Conversion*, vol. 31, no. 2, pp. 800–809, 2016.

[96] X. Xue, K. Cheng, and N. Cheung, "Selection of electric motor drives for electric vehicles," *in Proc. of the Australasian Universities Power Engineering Conference*, pp. 1–6, 2008.

[97] S. Kurian and G. K. Nisha, "State of the art of switched reluctance motor for torque ripple minimization," *International Journal of Industrial Electronics and Electrical Engineering*, vol. 2, no. 12, pp. 68–74, 2014.

[98] D. Dorrell, M. Knighta, M. Popescu, L. Evans, and D. Staton, “Comparison of different motor design drives for hybrid electric vehicles,” *in Proc. of the IEEE Energy Conversion Congress and Exposition*, pp. 3352–3359, 2010.

[99] J. Kim, Y. Jeong, Y. Jeon, J. Kang, S. Lee, and J. Park, “Development of a switched reluctance motor-based electric AC compressor drive for HEV/EV applications,” *Journal of Magnetics*, vol. 19, no. 3, pp. 282–290, 2014.

[100] P. Lawrenson, J. Stephenson, P. Blenkinsop, J. Corda, and N. Futon, “Variable-speed switched reluctance motors,” *IEE Proceedings B-Electric Power Applications*, vol. 127, no. 4, pp. 253–265, 1980.

[101] R. Suryadevara and B. Fernandes, “Control techniques for torque ripple minimization in switched reluctance motor: An overview,” *in Proc. on the IEEE International Conference on Industrial and Information Systems (ICIIS)*, pp. 24–29, 2013.

[102] S. Moore, K. Rahman, and M. Ehsani, “Effect on vehicle performance of extending the constant power region of electric drive motors,” *in Proc. of the SAE International Conference*, 1990.

[103] S. Amjad, S. Neelakrishnan, and R. Rudramoorthy, “Review of design considerations and technological challenges for successful development and deployment of plug-in hybrid electric vehicles,” *Renewable and Sustainable Energy Reviews*, vol. 14, pp. 1104–1110, 2010.

[104] A. Anekunu, S. Chowdhury, and S. Chowdhury, “A review of research and development on switched reluctance motor for electric vehicles,” *in Proc. of the Power and Energy Society General Meeting (PES)*, 2013.

[105] A. Labak and N. Kar, “Outer rotor switched reluctance motor design for in-wheel drive of electric bus applications,” *in Proc. of the International Conference on Electrical Machines (ICEM)*, pp. 418–423, 2012.

[106] E. Trancho, E. Ibarra, A. Arias, C. Salazar, I. Lopez, A. Diaz de Guereñu, and A. Peña, “IPMSM torque control strategies based on LUTs and VCT feedback for robust control under machine parameter variations,” in *Proc. of the IEEE Industrial Electronics Society Conferece (IECON)*, 2016.

[107] S. Jung, J. Hong, and K. Nam, "Current minimizing torque control of the IPMSM using Ferrari's method," *IEEE Transactions on Power Electronics*, vol. 28, no. 12, pp. 5603–5617, 2013.

[108] Y. Inoue, S. Morimoto, and M. Sanada, "Control scheme for wide-speed-range operation of synchronous reluctance motor in m-t frame synchronized with stator flux linkage," *IEEE Journal of Industry Applications*, vol. 2, no. 2, pp. 98–105, 2013.

[109] F. Barrero and J. Duran, "Recent advances in the design, modeling, and control of multiphase machines - part I," *IEEE Transactions on Industrial Electronics*, vol. 63, no. 1, pp. 449–458, 2016.

[110] ——, "Recent advances in the design, modeling, and control of multiphase machines - part II," *IEEE Transactions on Industrial Electronics*, vol. 63, no. 1, pp. 459–468, 2016.

[111] T. Lubin, H. Razik, and A. Rezzoug, "Magnetic saturation effects on the control of a synchronous reluctance machine," *Transactions on Energy Conversion*, vol. 17, no. 3, pp. 356–362, 2002.

[112] K. Meessen, P. Thelin, J. Soulard, and E. Lomonova, "Inductance calculations of permanent-magnet synchronous machines including flux change and self- and cross-saturations," *IEEE Transactions on Magnetics*, vol. 44, no. 10, pp. 2324–2331, 2008.

[113] D. Marcetic, R. Varga, and M. Bozic, "IPMSM model including magnetic saturation and cross-coupling," *Electronics*, vol. 16, no. 1, pp. 12–15, 2012.

[114] K. Ahn, A. Bayrak, and P. Papalambros, "Electric vehicle design optimization: Integration of a high-fidelity interior-permanent-magnet motor model," *IEEE Transactions on Vehicular Technology*, vol. 64, no. 9, pp. 3870–3877, 2015.

[115] H. Seol, J. Jeong, J. Lee, and C. Jin, "Current control of WRSM considering magnetic saturation phenomenon," *IEEE Transactions on Magnetics*, vol. 52, no. 7, 2016.

[116] C. Dufour, S. Cense, T. Yamada, R. Imamura, and J. Belanger, "FPGA permanent magnet synchronous motor floating-point models with Variable-DQ and spatial harmonic finite-element analysis solvers," in *Proc. of the International Power Electronics and Motion Control Conference, (EPE-PEMC ECCE Europe)*, 2012.

[117] J. Cintron-Rivera, S. Foster, W. Zanardelli, and E. Strangas, "High performance controllers based on real parameters to account for parameter variations due to iron saturation," in *In Proc. of the NDIA Ground Vehicle Systems Engineering and Technology Symposium*, 2013.

[118] J. Cintron-Rivera, S. Foster, C. Nino-Baron, and S. E., "High performance controllers for interior permanent magnet synchronous machines using look-up tables and curve-fitting methods," in *In Proc. of the IEEE International Electric Machines & Drives Conference (IEMDC)*, 2013, pp. 268–275.

[119] G. Schoonhoven and M. Uddin, "Wide speed range operation of PMSM drives using nonlinear flux control techniques," *in Proc. of the International Conference on Electrical and Computer Engineering*, pp. 603–606, 2014.

[120] L. Samaranayake and S. Longo, "Degradation control for electric vehicle machines using nonlinear model predictive control," *IEEE Transactions on Control Systems Technology*, vol. 26, no. 1, pp. 89–101, 2018.

[121] T. Pajchrowski and K. Zawirski, "Application of fuzzy logic techniques to robust speed control of PMSM," *in Proc. of the Power Electronics and Motion Control Conference*, pp. 1198–1203, 2008.

[122] S. Singh, A. Gautam, J. Dubey, J. Pandey, and R. Payasi, "Performance comparison of PMSM drive using PI and fuzzy logic based controllers," *in Proc. of the International Conference on Electrical, Computer and Electronics Engineering (UPCON)*, 2016.

[123] J. Su and I. H. Rui, "Model predictive control based field-weakening strategy for traction EV used induction motor," *in Proc. of the Energy Conversion Congress and Exposition (ECCE)*, 2016.

[124] A. Abdelsalam, K. Jung, and L. Young, "Model predictive torque control of PMSM for EV drives: A comparative study of finite control set and predictive deadbeat control schemes," *in Proc. of the Power Systems Conference (MEPCON)*, 2016.

[125] A. Ammar, A. Bourek, and A. Benakcha, "Efficiency optimization for sensorless induction motor controlled by MRAS based hybrid FOC-DTC strategy," *in Proc. of the International Conference on Control, Automation and Diagnosis (ICCAD)*, 2017.

[126] F. Korkmaz, I. Topaloglu, M. akir, and R. Grbz, “Comparative performance evaluation of FOC and DTC controlled PMSM drives,” *in Proc. of the International Conference on Power Engineering, Energy and Electrical Drives (POWERENG)*, 2013.

[127] D. Casadei, F. Profumo, G. Serra, and A. Tani, “FOC and DTC: Two viable schemes for induction motors torque control,” *IEEE Transactions on Power Electronics*, vol. 17, no. 5, pp. 779–787, 2002.

[128] X. Garcia, B. Zigmund, A. Terlizzi, T. Pavlanin, and L. Salvatore, “Comparison between FOC and DTC strategies for permanent magnet synchronous motors,” *in Proc. of the Advances in Electrical and Electronic Engineering Conference*, pp. 76–81, 2004.

[129] F. Niu, B. Wang, A. Babel, K. Li, and E. Strangas, “Comparative evaluation of direct torque control strategies for permanent magnet synchronous machines,” *IEEE Transactions on Power Electronics*, vol. 31, no. 2, pp. 1408–1424, 2016.

[130] J. Justo, F. Mwasilu, E. Kim, J. Kim, H. Choi, and J. Jung, “Fuzzy model predictive direct torque control of IPMSMs for electric vehicle applications,” *IEEE Transactions on Mechatronics*, vol. 22, no. 4, pp. 1542–1553, 2017.

[131] T. Geyer, G. Papafotiou, and M. Morari, “Model predictive direct torque control part I, concept, algorithm, and analysis,” *IEEE Transactions on Power Electronics*, vol. 56, no. 6, pp. 1894–1905, 2009.

[132] M. Preindl and S. Bolognani, “Model predictive direct torque control with finite control set for PMSM drive systems, part 2: Field weakening operation,” *IEEE Transactions on Industrial Informatics*, vol. 9, no. 2, pp. 648–657, 2013.

[133] M. Farasat, A. Trzynadlowski, and M. Fadali, “Efficiency improved sensorless control scheme for electric vehicle induction motors,” *IET Electrical Systems in Transportation*, vol. 4, no. 4, pp. 122–131, 2014.

[134] D. Mohan, X. Zhang, and G. Foo, “Generalized DTC strategy for multilevel inverter fed IPMSMs with constant inverter switching frequency and reduced torque ripples,” *IEEE Transactions on Energy Conversion*, vol. 32, no. 3, pp. 1031–1041, 2017.

[135] H. Ismail, A. Jidin, F. Patkar, S. Tarusan, A. Razi, and M. Rahim, "Constant switching frequency torque controller for DTC of induction motor drives with three-level NPC inverter," *in Proc. of the IEEE International Conference on Power and Energy*, 2016.

[136] A. Berzoy, J. Rengifo, and O. Mohammed, "Fuzzy predictive DTC of induction machines with reduced torque ripple and high-performance operation," *IEEE Transactions on Power Electronics*, vol. 33, no. 3, pp. 2580–2587, 2018.

[137] S. Malla, "A review on direct torque control (DTC) of induction motor: With applications of fuzzy," *in Proc. of the International Conference on Electrical, Electronics, and Optimization Techniques (ICEEOT)*, 2016.

[138] I. M. Alsofyani and N. R. Idris, "Lookup-table-based DTC of induction machines with improved flux regulation and extended kalman filter state estimator at low-speed operation," *IEEE Transactions on Industrial Informatics*, vol. 122, no. 4, pp. 1412–1425, 2016.

[139] W. Lin and H. Chiang, "Super-twisting algorithm second-order sliding mode control for a synchronous reluctance motor speed drive," *Hindawi Publishing Corporation Mathematical Problems in Engineering*, 2013.

[140] Texas Instruments, "Field orientated control of 3-phase AC-motors," *Tech. report*, 1998.

[141] S. Capitaneanu, B. Fornel, M. Fadel, and J. Faucher, "Graphical and algebraic synthesis for PWM methods," *EPE Journal*, vol. 11, no. 3, pp. 16–28, 2001.

[142] J. Pou, "Space vector PWM," *Tech. report, Technical university of Catalonia.*

[143] M. Chinchilla, S. Arnaltes, and J. Burgos, "Control of permanent-magnet generators applied to variable-speed wind energy system connected to the grid," *IEEE Transactions on Energy Conversion*, vol. 87, no. 1, pp. 130–135, 2006.

[144] A. Arias, J. Caum, and R. Griño, "Moving towards the maximum speed in stepping motors by means of enlarging the bandwidth of the current controller," *Mechatronics*, vol. 40, pp. 51–62, 2016.

[145] V. Utkin, J. Guldner, and J. Shi, *Sliding Mode Control in ElectroMechanical Systems.* CRC Press, 2009, vol. 39.

[146] A. Pisano, "Second order sliding modes: Theory and applications," Ph.D. dissertation, Dipartimento di Ingegneria Eletrica ed Elettronica, Univerista degli Studi di Cagliari, 2000.

[147] J. Liu, S. Vazquez, L. Wu, A. Marquez, H. Gao, and L. Franquelo, "Extended state observer-based sliding-mode control for three-phase power converters," *IEEE Transactions on Industrial Electronics*, vol. 64, no. 1, pp. 22–31, 2017.

[148] V. Repecho, D. Biel, and A. Arias, "Fixed switching period discrete-time sliding mode current control of a PMSM," *IEEE Transactions on Industrial Electronics*, vol. 65, no. 3, pp. 2039–2048, 2018.

[149] V. Repecho, D. Biel, R. Ramos-Lara, and P. Garcia, "Fixed-switching frequency interleaved sliding mode eight-phase synchronous Buck converter," *IEEE Transactions on Power Electronics*, vol. 33, no. 1, pp. 676–688, 2018.

[150] A. Susperregui, M. Martinez, I. Zubia, and G. Tapia, "Design and tuning of fixed-switching-frequency second-order sliding-mode controller for doubly fed induction generator power control," *IET Electric Power Applications*, vol. 6, pp. 696–706, 2012.

[151] A. Levant, "Sliding order and sliding accuracy in sliding mode control," *International Journal of Control*, vol. 58, no. 6, pp. 1247–1263, 1993.

[152] G. Bartolini, A. Ferrara, A. Levant, and E. Usai, *On second order sliding mode controller, Variable structure systems, sliding mode and nonlinear control.* Springer Lecture Notes, 1999.

[153] A. Damiano, A. Floris, G. Fois, I. Marongiu, M. Porru, and A. Serpi, "Design of a high-speed ferrite-based brushless DC machine for electric vehicles," *IEEE Transactions on Industry Applications*, vol. 53, no. 5, pp. 4279–4287, 2017.

[154] D. Gerada, A. Mecarki, N. Brown, C. Gereda, A. Cavagnino, and A. Boglietti, "High-speed electrical machines: Technologies, trends, and developments," *IEEE Transactions on Industrial Electronics*, vol. 61, no. 6, pp. 2946–2959, 2014.

[155] M. Besbes, H. Chehimi, S. Hadj, and F. Sahli, “Study on the FPGA implementation of high gain observer with sampled measurement for induction machine,” *in Proc. of the International conference on Sciences and Techniques of Automatic control and computer engineering*, 2015.

[156] University of Oslo, “Signal sampling,” *Tech. report*, 2015.

[157] E. Durna, “Effect of sampling frequency and execution time on hysteresis current controlled three-phase three-wire hapf converters,” *in Proc. of the International Symposium on Power Electronics, Electrical Drives, Automation and Motion*, 2016.

[158] J. Millan, P. Godignon, X. Perpina, A. Perez-Tomas, and J. Rebollo, “A survey of wide bandgap power semiconductor devices,” *IEEE Transactions on Power Electronics*, vol. 29, no. 5, pp. 2155–2163, 2014.

[159] J. Millan, “A review of WBG power semiconductor devices,” *in Proc. of the Semiconductor Conference (CAS)*, pp. 57–66, 2012.

[160] A. Stefanskyi, L. Starzak, and A. Napieralski, “Silicon carbide power electronics for electric vehicles,” *in Proc. of the International Conference on Ecological Vehicles and Renewable Energies (EVER)*, pp. 1–9, 2015.

[161] E. Monmasson and M. Cirstea, “Guest editorial special section on industrial control applications of FPGAs,” *IEEE Transactions on Industrial Informatics*, vol. 9, no. 3, pp. 1250–1252, 2013.

[162] A. Darba, F. Belie, P. D’haese, and J. Melkebeek, “Improved dynamic behavior in BLDC drives using model predictive speed and current control,” *IEEE Transactions on Industrial Electronics*, vol. 63, no. 2, pp. 728–740, 2016.

[163] A. Altomare, A. Guagnano, F. Cupertino, and D. Naso, “Discrete time control of high-speed salient machines,” *IEEE Transactions on Industry Applications*, vol. 52, no. 1, pp. 293–301, 2016.

[164] A. Guagnano, F. Rizzello, G. Cupertino, and D. Naso, “Robust control of high-speed synchronous reluctance machines,” *IEEE Transactions on Industry Applications*, vol. 52, no. 5, pp. 3990–4000, 2016.

[165] L. Sepulchre, M. Fadel, and M. David, “Improvement of the digital control of a high speed PMSM for vehicle application,” *in Proc. of the International Conference on Ecological Vehicles and Renewable Energies (EVER)*, 2016.

[166] E. Trancho, E. Ibarra, A. Arias, I. Kortabarria, J. Jurgens, L. Marengo, A. Fricasse, and J. Gragger, "PM-assisted synchronous reluctance machine flux weakening control for EV and HEV applications," *IEEE Transactions on Industrial Electronics*, vol. 65, no. 4, pp. 2986–2995, 2017.

[167] S. Morimoto, Y. Takeda, T. Hirasa, and K. Taniguchi, "Expansion of operating limits for permanent magnet motor by current vector control considering inverter capacity," *IEEE Transactions on Industry Applications*, vol. 26, no. 5, pp. 866–871, 1990.

[168] G. Pellegrino, R. Bojoi, and P. Guglielmi, "Unified direct-flux vector control for AC motor drives," *IEEE Transactions on Industry Applications*, vol. 47, no. 5, pp. 2193–2102, 2011.

[169] K. Chen, Y. Sun, and B. Liu, "Interior permanent magnet synchronous motor linear field-weakening control," *IEEE Transactions on Energy Conversion*, vol. 31, no. 1, pp. 159–164, 2016.

[170] Y. Jeong, S. Sul, S. Schulz, and N. Patel, "Fault detection and fault-tolerant control of interior permanent-magnet motor drive system for electric vehicle," *IEEE Transactions on Industry Applications*, vol. 41, no. 1, pp. 46–51, 2005.

[171] R. Tallam, S. Lee, G. Stone, G. Kliman, J. Yoo, T. Habetler, and R. Harley, "A survey of methods for detection of stator-related faults in induction machines," *IEEE Transactions on Industry Applications*, vol. 43, no. 4, pp. 920–933, 2007.

[172] National Highway Traffic Safety Administration, "Failure modes and effects analysis for hydrogen fuel cell vehicles - subtask 1," *Tech. report, U.S. Department of transportation*, 2009.

[173] V. Ferencey, "Failure modes and effect analysis which is applied to the electric powertrain system of unmanned ground vehicle," *Portl pre odborn publikovanie*, vol. 4, no. 7, pp. 1–9, 2011.

[174] S. Haghbin, "Electrical failure mode and effect analysis of a 3.3kW onboard vehicle battery charger," *in Proc. of the European Conference on Power Electronics and Applications*, 2016.

[175] E. Zio, *An Introduction to the Basics of Reliability and Risk Analysis.* World Scientific, 2007.

[176] J. Hang, S. Ding, J. Zhang, M. Cheng, W. Chen, and Q. Wang, “Detection of interturn short-circuit fault for PMSM with simple fault indicator,” *IEEE Transactions on Energy Conversion*, vol. 31, no. 4, pp. 1697–1699, 2016.

[177] L. Otava, “Implementation of PMSM inter-turn short fault detection using frequency analysis of stator currents,” *IFAC, Elsevier*, vol. 49, no. 25, pp. 86–91, 2016.

[178] M. Fitouri, Y. Bensalem, and M. Abdelkrim, “Modeling and detection of the short-circuit fault in PMSM using finite element analysis,” *IFAC, Elsevier*, vol. 49, no. 12, pp. 1418–1423, 2016.

[179] M. Alavi, D. Wang, and M. Luo, “Short-circuit fault diagnosis for three-phase inverters based on voltage-space patterns,” *IEEE Transactions on Industrial Electronics*, vol. 61, no. 10, pp. 5558–5569, 2014.

[180] M. Zhu, W. Hu, and N. Kar, “Torque ripple based interior permanent magnet synchronous machine rotor demagnetization fault detection and current regulation,” *IEEE Transactions on Industry Applications*, vol. 53, no. 3, pp. 2795–2804, 2016.

[181] G. Pacoli, W. Hribernik, G. Ujvari, and B. Fruth, “Partial discharge diagnosis of generator insulation systems - measurements, simulations and picture recognition,” *in Proc. of the IEEE International Symposium on Diagnostics for Electric Machines, Power Electronics and Drives*, pp. 475–479, 2007.

[182] J. Riba, A. Garcia-Espinoza, L. Romeral, and J. Cusido, “Demagnetization diagnosis in permanent magnet synchronous motors under non-stationary speed conditions,” *Electric Power Systems Research*, vol. 80, pp. 1277–1285, 2010.

[183] J. Urresty, R. Atashkhooei, J. Riba, L. Romeral, and S. Royo, “Shaft trajectory analysis in a partially demagnetized permanent-magnet synchronous motor,” *IEEE Transactions on Industrial Electronics*, vol. 60, no. 8, pp. 3454–3461, 2013.

[184] S. Moosavi, A. Djerdir, Y. Amirat, and D. Khaburi, “Demagnetization fault diagnosis in permanent magnet synchronous motors: A review of the state-of-the-art,” *Journal of Magnetism and Magnetic Materials*, vol. 391, pp. 203–212, 2015.

[185] A. Sharma, L. Golubchik, and R. Govindan, "On the prevalence of sensor faults in real-world deployments," *in. Proc. of the Annual IEEE Communications Society Conference on Sensor, Mesh and Ad Hoc Communications and Networks*, 2007.

[186] M. Benbouzid, D. Diallo, and M. Zeraoulia, "Advanced fault-tolerant control of induction-motor drives for EV/HEV traction applications: From conventional to modern and intelligent control techniques," *IEEE Transactions on Vehicular Technology*, vol. 56, no. 2, pp. 519–528, 2007.

[187] D. Diallo, M. Benbouzid, and A. Makouf, "A fault-tolerant control architecture for induction motor drives in automotive applications," *IEEE Transactions on Vehicular Technology*, vol. 53, no. 6, pp. 1847–1855, 2004.

[188] G. Rang, J. Lim, K. Nam, H. Ihm, and H. Kim, "A MTPA control scheme for an IPM synchronous motor considering magnet flux variation caused by temperature," in *in Proc. of the Applied Power Electronics Conference and Exposition (APEC)*, 2004.

[189] T. Herold, D. Franck, E. Lange, and K. Hameyer, "Extension of a D-Q model of a permanent magnet excited synchronous machine by including saturation, cross-coupling and slotting effects," in *in Proc. of the International Electric Machines and Drives Conference*, 2011.

[190] J. Kim and S. Sul, "Speed control of interior permanent magnet synchronous motor drive for the flux weakening operation," *IEEE Transactions on Industry Applications*, vol. 33, no. 1, pp. 43 – 48, 1997.

[191] S. Shue and C. Pan, "Voltage-constraint-tracking-based field-weakening control of IPM synchronous motor drives," *IEEE Transactions on Industrial Electronics*, vol. 55, no. 1, pp. 340–347, 2008.

[192] J. Lee, C. Won, B. Lee, J. Baek, K. Han, and U. Chung, "IPMSM torque control method considering DC-link voltage variation and friction torque for EV/HEV applications," in *Proc. of the IEEE Vehicle Power and Propulsion Conference*, 2012, pp. 1063–1069.

[193] B. Nguyen, V. Han, and C. Minh, "High performance current control of IPMSM for electric vehicles drives using disturbance observer," in *Proc. of the IEEE Vehicle Power and Propulsion Conference (VPPC)*, 2015.

[194] J. S. Choi, H. H. Choi, and J. W. Jung, "Feedback linearization direct torque control with reduced torque and flux ripples for IPMSM drives," *IEEE Transactions on Power Electronics*, vol. 31, no. 5, pp. 3728–3737, 2015.

[195] S. Huang, Z. Chen, K. Huang, and J. Gao, "Maximum torque per ampere and flux-weakening control for PMSM based on curve fitting," in *Proc. of the IEEE Vehicle Power and Propulsion Conference (VPPC)*, 2010.

[196] M. Hoque, C. Butt, and M. Rahman, "A novel approach for MTPA speed control of IPMSM drive," in *Proc. of the International Conference on Electrical and Computer Engineering (ICECE)*, 2002, pp. 336–339.

[197] Z. Lei, W. Xuhui, Z. Feng, K. Liang, and Z. Baocang, "Deep field-weakening control of PMSM for both motion and generation operation," in *Proc. of the International Conference on Electrical Machines and Systems (ICEMS)*, 2011.

[198] J. Kim and S. Sul, "Speed control of interior permanent magnet synchronous motor drive for the flux weakening operation," *IEEE Transactions on Industry Applications*, vol. 33, no. 1, pp. 43–48, 1997.

[199] P. Lin and Y. Lai, "Novel voltage trajectory control for flux weakening operation of surface mounted PMSM drives," in *Proc. of the IEEE Industry Applications Society Annual Meeting*, 2008.

[200] S. Bolognani, S. Calligaro, and R. Petrella, "Adaptive flux-weakening controller for interior permanent magnet synchronous motor drives," *IEEE Journal of Emerging and Selected Topics in Power Electronics*, vol. 2, no. 2, pp. 236–248, 2014.

[201] H. Eldeeb, C. Hackl, J. Kullick, and L. Horlbeck, "Analytical solutions for the optimal reference currents for MTPC/MTPA, MTPV and MTPF control of anisotropic synchronous machines," *in Proc. of the IEEE International Electric Machines and Drives Conference (IEMDC)*, 2017.

[202] R. Ni, D. Xu, G. Wang, L. Ding, G. Zhang, and L. Qu, "Maximum efficiency per ampere control of permanent-magnet synchronous machines," *IEEE Transactions on Industrial Electronics*, vol. 62, no. 4, pp. 2135–2143, 2015.

[203] J. Ahn, S. Lim, K. Kim, and J. Lee, "Field weakening control of synchronous reluctance motor for electric power steering," *IET Electric Power Applications*, vol. 1, no. 4, pp. 565–570, 2007.

[204] D. Dang, M. Rafaq, H. Choi, and J. Jung, "Online parameter estimation technique for adaptive control applications of interior PM synchronous motor drives," *IEEE Transaction on Industrial Electronics*, vol. 63, no. 3, pp. 1438–1449, 2016.

[205] H. Kim and R. Lorenz, "Improved current regulators for IPM machine drives using on-line parameter estimation," *in Proc. of the IEEE Industry Applications Conference (IAS)*, 2002.

[206] J. Lara, J. Xu, and A. Chandra, "Effects of rotor position error in the performance of Field-Oriented-Controlled PMSM drives for electric vehicle traction applications," *IEEE Transaction on Industrial Electronics*, vol. 63, no. 8, pp. 4738–4751, 2016.

[207] Y. Wang, D. Ionel, V. Rallabandi, M. Jiang, and S. Stretz, "Large-scale optimization of synchronous reluctance machines using CE-FEA and differential evolution," *IEEE Transactions on Industry Applications*, vol. 52, no. 6, pp. 4699–4709, 2016.

[208] K. Rahman and S. Hiti, "Identification of machine parameters of a synchronous motor," *in Proc of the IEEE Industry Aplications (IAS) conference*, 2013.

[209] M. Yilmaz and P. T. Krein, "Capabilities of finite element analysis and magnetic equivalent circuits for electrical machine analysis and design," *in Proc. of the IEEE Power Electronics Specialist Conference (PESC)*, 2008.

[210] M. Ott, A. Gulec, and J. Bocker, "An iterative compensation method for production tolerances in electric drive systems," *in Proc. of the IEEE International Electric Machines and Drives Conference (IEMDC)*, 2017.

[211] J. Li, S. Ekanayake, M. Rahman, R. Dutta, X. Huang, J. Ma, and Y. Fang, "Deep flux weakening control with six-step overmodulation for a segmented interior permanent magnet synchronous motor," *in Proc. of the International Conference on Electrical Machines and Systems (ICEMS)*, 2017.

[212] S. Amornwongpeeti, O. Kiselychnyk, J. Wang, N. Shatti, N. Shah, and M. Soumelidis, “Adaptive torque control of IPMSM motor drives for electric vehicles,” *in Proc. of the IEEE International Symposium on Industrial Electronics (ISIE)*, pp. 226 – 231, 2017.

[213] C. Pan and S. Sue, “A linear maximum torque per ampere control for IPMSM drives over full-speed range,” *IEEE Transactions on Energy Conversion*, vol. 20, no. 2, pp. 359–366, 2005.

[214] I. Boldea and S. Nasar, *Electric Drives.* CRC Press, 1999.

[215] A. Specht and J. Bocker, “Observer for the rotor temperature of IPMSM,” in *Proc. of the International Power Electronics and Motion Control Conference (EPE-PEMC)*, 2010.

[216] M. Ganchev, C. Kral, and T. Wolbank, “Sensorless rotor temperature estimation of permanent magnet synchronous motor under load conditions,” in *Proc. of the IEEE Industrial Electronics Conference (IECON)*, 2012, pp. 1989–1994.

[217] Dorf and Bishop, *Modern Control Systems.* Pearson/Prentice-Hall, 2005.

[218] J. L. Lin, “A new approach of dead-time compensation for PWM voltage inverters,” *IEEE Transactions on Circuits and Systems - I: Fundamental Theory and Applications*, vol. 49, no. 4, 2002.

[219] U. Tietge, N. Zacharof, P. Mock, V. Franco, J. German, A. Bandivadekar, N. Ligterink, and U. Lambrecht, “A 2015 update of official and real-world fuel consumption and CO_2 values for passenger cars in Europe,” *The International Council of Clear Transportation*, 2015.

[220] E. Bagalini, J. Sini, M. Sonza, and M. Violante, “An automatic approach to perform the verification of hardware designs according to the ISO26262 functional safety standard,” *In Proc. of the 18th IEEE Latin American Test Symposium (LATS)*, 2017.

[221] P. Carvalho, “Mapping the Software Errors and Effects Analysis to ISO26262 requirements for software architecture analysis,” *In Proc. of the IEEE International Symposium on Software Reliability Engineering Workshops*, 2014.

[222] V. Bonfiglio, L. Meontecchi, I. Irrera, F. Rossi, P. Lollini, and A. Bondavalli, “Software Faults Emulation at Model-Level: Towards Automated Software FMEA,” *In Proc. of the IEEE International Conference on Dependable Systems and Networks Workshops*, 2015.

[223] S. Bolognani, L. Tubiana, and M. Zigliotto, “Extended Kalman Filter tuning in sensorless PMSM drives,” *IEEE Transactions on Industry Applications*, vol. 39, no. 6, pp. 1741–1747, 2003.

[224] D. Janiszewski, *Extended Kalman Filter Based Speed Sensorless PMSM Control with Load Reconstruction.* INTECH, 2010.

[225] V. Bindu, A. Unnikrishnan, and R. Gopikakumari, “Sensorless vector control of PMSM using a blind system identification approach based on extended kalman filter algorithm,” in *Proc. of the IEEE International Conference on Computational Intelligence and Computing Research*, 2010.

[226] T. Senjyu, K. Kinjo, N. Urasaki, and K. Uezato, “Sensorless control of synchronous reluctance motors considering the stator iron loss with Extended Kalman Filter,” in *Proc. of the Power Electronics Specialist Conference (PESC)*, 2003, pp. 403–408.

[227] M. Huang, A. Moses, and F. Anayi, “The comparison of sensorless estimation techniques for PMSM between Extended Kalman Filter and flux-linkage observer,” in *Proc. of the Applied Power Electronics Conference and Exposition (APEC)*, 2006, pp. 654–659.

[228] S. Bolognani, A. Faggion, E. Fornasiero, and L. Sgarbossa, “Full speed range sensorless IPM motor drives,” *in Proc. of the International Conference on Electrical Machines (ICEM)*, 2012.

[229] L. Idkhajine, E. Monmasson, and A. Maalouf, “Extended Kalman filter for AC drive sensorless speed controller - FPGA-based solution or DSP-based solution,” *in Proc. of the IEEE International Symposium on Industrial Electronics (ISIE)*, 2010.

[230] N. Henwood, J. Malaize, and L. Plary, “A robust nonlinear luenberger observer for the sensorless control of SM-PMSM: Rotor position and magnets flux estimation,” *in Proc. of the IEEE Industrial Electronics Society (IECON)*, pp. 1625–1630, 2012.

[231] M. Jouili, K. Jarray, Y. Koubaa, and M. Boussak, “A Luenberger state observer for simultaneous estimation of speed and rotor resistance in sensorless indirect stator flux orientation control of induction motor drive,” *in Proc. of the International Conference on Sciences and Techniques of Automatic Control and Computer Engineering (STA)*, 2015.

[232] S. Chen, Y. Luo, and Y. Pi, “PMSM sensorless control with separate control strategies and smooth switch from low speed to high speed,” *ISA Transactions*, vol. 58, pp. 650–658, 2015.

[233] S. Chi and L. Xu, “Position sensorless control of PMSM based on a novel sliding mode observer over wide speed range,” in *Proc. of the Power Electronics and Motion Control Conference*, 2006.

[234] Z. Qiao, T. Shi, Y. Wang, Y. Yan, C. Xia, and H. X., “New sliding-mode observer for position sensorless control of permanent-magnet synchronous motor,” *IEEE Transactions on Industrial Electronics*, vol. 60, no. 2, pp. 710–719, 2013.

[235] R. Li and G. Zhao, “Position sensorless control for PMSM using sliding mode observer and phase-locked loop,” in *Proc. of the Power Electronics and Motion Control Conference*, 2009.

[236] S. Maiti, V. Verma, C. Chakraborty, and Y. Hori, “An adaptive speed sensorless induction motor drive with artificial neural network for stability enhancement,” *IEEE Transactions on Industrial Informatics*, vol. 8, no. 4, pp. 757–766, 2012.

[237] S. Hussain and M. Bazaz, “Sensorless control of PMSM drive using neural network observer,” *In Proc. of the IEEE International Conference on Power Electronics, Intelligent Control and Energy Systems (ICPEICES)*, 2016.

[238] Y. Yang, “A Neural Network Model Reference Adaptive System for Speed Estimation of Sensorless Induction Motor,” *In Proc. of the 29th Chinese Control and Decision Conference*, 2017.

[239] G. El-Murr, D. Giaouris, and J. Finch, “Universal PLL strategy for sensorless speed and position estimation of PMSM,” in *Proc. of the IEEE Industrial and Information Systems Conference*, 2008.

[240] C. Olivieri and M. Tursini, “A novel PLL scheme for a sensorless PMSM drive overcoming common speed reversal problems,” in *Proc. of the International Symposium on Power Electronics, Electrical Drives, Automation and Motion*, 2012.

[241] A. Piipo, M. Hinkkanen, and J. Luomi, “Sensorless control of PMSM drives using a combination of voltage model and HF signal injection,” in *Proc. of the IEEE Industry Applications Conference*, 2004.

[242] J. Jang, S. Sul, J. Ha, and K. Ide, “Sensorless drive of surface-mounted permanent-magnet motor by high-frequency signal injection based on magnetic saliency,” *IEEE Transactions on Industry Applications*, vol. 39, no. 4, pp. 1031–1039, 2003.

[243] S. Zaim, B. Nahid-Mobarakeh, and F. Meibody-Tabar, “Robust position sensorless control of nonsalient pmsm at standstill and low speeds,” *IEEE Journal of Emerging and Selected Topics in Power Electronics*, vol. 2, no. 3, pp. 640–650, 2014.

[244] N. Chen, Z. Wang, S. Yu, W. Gui, and Y. Guo, “A new starting method of sensorless PMSM motors based on TMS 32F103B,” *in Proc. of the Control Conference*, 2010.

[245] F. Parasiliti, R. Petrella, and M. Tursini, “Sensorless speed control of a PM synchronous motor based on sliding mode observer and extended Kalman filter,” *in Proc. of the IEEE Industry Applications Conference*, 2001.

[246] A. Arias, G. Asher, M. Sumner, P. Wheeler, L. Empringham, and C. Silva, “High frequency voltage injection for the sensorless control of permanent magnet synchronous motors using matrix converters,” in *Proc. of the IEEE Industrial Electronics Conference (IECON)*, 2004, pp. 969–974.

[247] I. Omrane, W. Dib, E. Etien, and O. Bachelier, “Sensorless control of PMSM based on a nonlinear observer and a high-frequency signal inj ection for automotive applications,” *in Proc. of the IEEE Industrial Electronics Society Conference (IECON)*, pp. 3130–3135, 2013.

[248] R. Leidhold, “Position sensorless control of PM synchronous motors based on zero-sequence carrier injection,” *IEEE Transactions on Industrial Electronics*, vol. 58, no. 12, pp. 5371–5379, 2011.

[249] J. Holtz and J. Juliet, “Sensorless acquisition of the rotor position angle of induction motors with arbitrary stator windings,” *IEEE Transactions on Industry Applications*, vol. 41, pp. 1675–1682, 2005.

[250] X. Wu, H. Wang, S. Huang, K. Huang, and L. Wang, “Sensorless speed control with initial position estimation for surface mounted synchronous motor drive in electric vehicles,” *Energies*, vol. 8, no. 10, pp. 11 030–11 046, 2015.

[251] Y. Yan, J. Zhu, and Y. Guo, “Initial rotor position estimation and sensorless direct torque control of surface mounted permanent magnet synchronous motors considering saturation saliency,” *IET Electric Power Applications*, vol. 2, no. 1, pp. 42–48, 2008.

[252] K. Tanaka, T. Yuzawa, R. Morimyama, and I. Miki, “Initial rotor position estimation for surface permanent magnet synchronous motor,” *in Proc. of the International Conference on Electrical Machines and System (ICEMS)*, pp. 2592–2597, 2001.

[253] J. Holtz, “Initial rotor polarity detection and sensorless control of PM synchronous machines,” *in Proc. of the IEEE Industry Applications Conference*, 2006.

[254] H. Kim, K. Huh, and R. Lorenz, “A novel method for initial rotor position estimation for IPM synchronous machine drives,” *IEEE Transactions in Industrial Electronics*, vol. 40, no. 5, pp. 1369–1378, 2004.

[255] J. Ha, K. Ide, T. Sawa, and S. Sul, “Sensorless position control and initial position estimation of an interior permanent magnet motor,” *in Proc. of the IEEE Industry Applications Conference*, pp. 761–767, 2001.

[256] A. Arias, C. Silva, G. Asher, J. Clare, and P. Wheeler, “Use of a matrix converter to enhance the sensorless control of a surface-mount permanent-magnet AC motor at zero and low frequency,” *IEEE Transaction on Industrial Electronics*, vol. 53, pp. 440–449, 2006.

[257] Y. Inoue, S. Morimoto, and M. Sanada, “A novel control scheme for maximum power operation of synchronous reluctance motors including maximum torque per flux control,” *IEEE Transactions on Industry Applications*, vol. 47, no. 1, pp. 115–121, 2011.

[258] M. Corley and D. Lorenz, “Rotor position and velocity estimation for a salient-pole permanent magnet synchronous machine at standstill and high speeds,” *IEEE Transactions on Industry Applications*, vol. 34, no. 4, pp. 784–789, 1998.

[259] C. Silva, G. Asher, and M. Summer, “Hybrid rotor position observer for wide speed-range sensorless PM motor drives including zero speed,” *IEEE Transactions on Industrial Electronics*, vol. 53, no. 2, pp. 373–378, 2006.

[260] S. Sayeef, G. Foo, and M. Rahman, “Rotor position and speed estimation of a variable structure direct-torque-controlled IPM synchronous motor drive at very low speeds including standstill,” *IEEE Transactions on Industrial Electronics*, vol. 57, no. 11, pp. 3715–3723, 2010.

[261] Y. Risfendra, Kung and H. L.C., “Design and Digital Hardware Implementation of a Sensorless Controller for PMSM Drives using LF Signal Injection and EKF,” *In Proc. of the International conference on Applied System Innovation (ICASI)*, 2017.

[262] D. Paulus, P. Landsmann, and R. Kennel, “Saliency based sensorless field-oriented control for permanent magnet synchronous machines in the whole speed range,” *in Proc. of the IEEE Symposium on Sensorless Control for Electrical Drives (SLED)*, 2012.

[263] V. Kaura and V. Blasko, “Operation of a phase locked loop system under distorted utility conditions,” *IEEE Transactions on Industry Applications*, vol. 33, no. 1, pp. 58 – 63, 1997.

[264] M. Karimi-Ghartemani and M. Iravani, “A method for synchronization of power electronic converters in polluted and variable-frequency environments,” *IEEE Transactions on Power Systems*, vol. 19, no. 3, pp. 1263–1270, 2004.

[265] S. Chung, “A phase tracking system for three phase utility interface inverters,” *IEEE Transactions on Power Systems*, vol. 15, no. 3, pp. 431–438, 2000.

[266] L. Medjmadj, D. Diallo, M. Mostefai, C. Delpha, and A. Arias, “PMSM drive position estimation: Contribution to the high-frequency injection voltage selection issue,” *IEEE Transactions on Energy Conversion*, vol. 30, no. 1, pp. 349–358, 2015.